

DISSERTATION

MECHANISMS OF OBSERVED SEA SURFACE TEMPERATURE VARIABILITY  
IN THE EXTRATROPICAL SOUTHERN HEMISPHERE

Submitted by

Laura M. Ciasto

Department of Atmospheric Science

In partial fulfillment of the requirements

For the Degree of Doctor of Philosophy

Colorado State University

Fort Collins, Colorado

Summer 2008

UMI Number: 3332708

## INFORMATION TO USERS

The quality of this reproduction is dependent upon the quality of the copy submitted. Broken or indistinct print, colored or poor quality illustrations and photographs, print bleed-through, substandard margins, and improper alignment can adversely affect reproduction.

In the unlikely event that the author did not send a complete manuscript and there are missing pages, these will be noted. Also, if unauthorized copyright material had to be removed, a note will indicate the deletion.

**UMI**<sup>®</sup>

---

UMI Microform 3332708

Copyright 2008 by ProQuest LLC.

All rights reserved. This microform edition is protected against unauthorized copying under Title 17, United States Code.

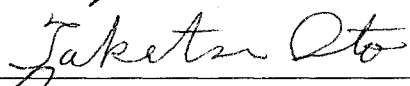
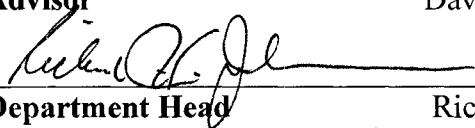
ProQuest LLC  
789 E. Eisenhower Parkway  
PO Box 1346  
Ann Arbor, MI 48106-1346

COLORADO STATE UNIVERSITY

June 16, 2008

WE HEREBY RECOMMEND THAT THE DISSERTATION PREPARED UNDER OUR SUPERVISION BY LAURA M. CIASTO ENTITLED MECHANISMS OF OBSERVED SEA SURFACE TEMPERATURE VARIABILITY IN THE EXTRATROPICAL SOUTHERN HEMISPHERE BE ACCEPTED AS FULFILLING IN PART REQUIREMENTS FOR THE DEGREE OF DOCTOR OF PHILOSOPHY.

Committee on Graduate Work

	_____	Scott Denning
	_____	Clara Deser
	_____	Geof Givens
	_____	Takamitsu Ito
	_____	David Thompson
<b>Advisor</b>		
	_____	Richard Johnson
<b>Department Head</b>		

## ABSTRACT OF DISSERTATION

### MECHANISMS OF OBSERVED SEA SURFACE TEMPERATURE VARIABILITY IN THE EXTRATROPICAL SOUTHERN HEMISPHERE

The physical mechanisms that drive sea surface temperature (SST) variability in the extratropical Southern Hemisphere (SH) are examined using multiple ocean temperature datasets. The first part of the study provides a detailed analysis of the relationships between variability in SH SST anomalies, the Southern Annular Mode (SAM) and the El-Niño/Southern Oscillation (ENSO) during the warm (November-April) and cold (May-October) seasons. It is shown that the signatures of the SAM and ENSO in the SST field vary as a function of season, both in terms of their amplitudes and structures. SAM-related SST anomalies are primarily driven by surface turbulent heat fluxes with a smaller contribution from heat advection by Ekman currents. The role of turbulent heat fluxes in generating ENSO-related SST anomalies is less clear.

Analyses of the temporal evolution of the relationships between the SAM and the SST field demonstrate that SST anomalies are largest when SSTs lag by  $\sim 1$  week and persist for up to 8 weeks. In the absence of ENSO, cold season SAM-related SST anomalies persist longer than their warm season counterparts, consistent with seasonal variations in the depth of the mixed layer.

The second part of the study uses observations of subsurface temperatures to examine the winter-to-winter “reemergence” of SST anomalies in the extratropical South

Pacific. Reemergence is the mechanism whereby SST anomalies formed in the late winter are sequestered beneath the shallow summer mixed layer and then re-entrained into the deepening mixed layer during the following fall/winter. The results exhibit a pronounced reemergence signal in which surface temperature anomalies during the late winter season are strongly correlated with surface temperature anomalies during the subsequent early winter months, but are only significantly correlated with temperature anomalies beneath the mixed layer during the intervening summer months. The results are robust to small changes in the period of analysis and are qualitatively similar to existing evidence of reemergence in the Northern Hemisphere. The signal of reemergence evident in the subsurface data is readily apparent in SST data in the western South Pacific. Reemergence is less evident in SST data in the eastern South Pacific.

Laura M. Ciasto  
Department of Atmospheric Science  
Colorado State University  
Fort Collins, CO 80523  
Summer 2008

## ACKNOWLEDGMENTS

Deepest thanks goes to my advisor Dr. David W. J. Thompson, whose guidance has been invaluable. I would also like to thank committee members, Dr. Clara Deser, Senior Scientist in the Climate and Global Dynamics Division at the National Center for Atmospheric Research (NCAR), Boulder Colorado; Dr. Scott Denning, Professor of Atmospheric Science at Colorado State University (CSU); Dr. Taka Ito, Professor of Atmospheric Science (CSU); Dr. Geof Givens, Professor of Statistics (CSU). Drs. Mike Alexander, James Hurrell, Stephen Rintoul, Carolina Vera, and Mike Wallace provided valuable comments on the research presented in this dissertation. Further thanks goes to my research group, including Kevin Grise, Amy Butler, and Jillian L'Ecuyer as well as my friends and family for their support. This research was supported by the National Science Foundation (NSF) under ATM-0613082 and ATM-0132190.

## TABLE OF CONTENTS

<b>1. INTRODUCTION</b> .....	<b>1</b>
1.1. Heat Budget of the Ocean Mixed Layer .....	2
1.1.1. Radiative heat fluxes .....	4
1.1.2. Surface turbulent heat fluxes .....	5
1.1.3. Horizontal transport of heat .....	6
1.1.4. Vertical transport of heat .....	10
1.1.5. The null hypothesis of extratropical SST variability .....	12
1.2. Observations of Large-Scale Extratropical SST Variability in the Southern Hemisphere .....	13
1.2.1. Leading modes of Southern Hemisphere atmospheric variability and associated patterns of SST anomalies .....	15
1.2.2. Reemergence of wintertime SST anomalies .....	18
1.2.3. The Antarctic Circumpolar Current .....	19
1.3. Objectives .....	21
<b>2. DATA AND METHODOLOGY</b> .....	<b>23</b>
2.1. Data .....	23
2.1.1. Sea surface temperature data .....	23
2.1.2. Subsurface temperature data .....	28
2.1.3. Mixed layer depth data .....	31
2.1.4. Sea surface height data .....	32
2.1.5. Atmospheric data .....	32
2.2. Methodology .....	34
2.2.1. Regression and correlation analyses .....	35
2.2.2. Empirical Orthogonal Function (EOF) analysis .....	36
<b>3. RELATIONSHIPS BETWEEN PATTERNS OF LARGE-SCALE ATMOSPHERIC VARIABILITY AND EXTRATROPICAL SOUTHERN HEMISPHERE SEA SURFACE TEMPERATURE ANOMALIES</b> .....	<b>42</b>
3.1. Overview .....	42
3.2. Relevant Aspects of the Climatology .....	42
3.3. Patterns of SH SST Anomalies Associated with the SAM and ENSO .....	44
3.4. Physical Processes That Drive SH SST Variability on Monthly Timescales ..	49
3.5. Concluding Remarks .....	55

<b>4. TEMPORAL EVOLUTION AND PERISTENCE OF SOUTHERN HEMISPHERE SEA SURFACE TEMPERATURE ANOMALIES ASSOCIATED WITH THE SOUTHERN ANNULAR MODE</b> .....	<b>74</b>
4.1. Overview .....	74
4.2. Relationships between the SAM and SH SST Anomalies on Weekly Timescales .....	74
4.3. Persistence of the SAM-SST Relationship .....	76
4.4. Concluding Remarks .....	80
<b>5. OBSERVATIONAL EVIDENCE OF REEMERGENCE IN THE EXTRATROPICAL SOUTHERN HEMISPHERE</b> .....	<b>91</b>
5.1. Overview .....	91
5.2. Methodology .....	91
5.3. The Reemergence Signal in Extratropical South Pacific Subsurface Temperature Observations .....	93
5.4. The Surface Signature of Reemergence across the Extratropical South Pacific .....	98
5.5. Concluding Remarks .....	100
<b>6. CONCLUSIONS</b> .....	<b>111</b>
6.1. Summary and Discussion .....	111
6.2. Future Research .....	116
6.2.1. Persistence of extratropical SST anomalies as a function of hemisphere .....	116
6.2.2. Atmospheric response to persistent SH SST anomalies .....	117
<b>REFERENCES</b> .....	<b>121</b>

## **CHAPTER ONE**

### **INTRODUCTION**

The Southern Hemisphere (SH) ocean basins, including the South Atlantic, South Pacific, Indian and Southern Oceans, account for ~60% of the total area of the world ocean. However, the SH oceans are also some of the most poorly sampled regions of the globe, particularly poleward of 30°S. The lack of in situ data has limited the exploration of variability in the SH oceans until recently when observations from programs such as the World Ocean Circulation Experiment (WOCE), ARGO and satellite-derived sea surface temperatures (SSTs) have become available.

Analyses of the available observations suggest that variability in the SH oceans may significantly impact the global climate system. For example, the lack of physical barriers in the Southern Ocean allows water to flow via the Antarctic Circumpolar Current (ACC) along all longitudes uninterrupted by land, thus linking all major ocean basins in the SH. This communication between basins is crucial for the transport of heat and other properties around the globe. For instance, the meridional overturning circulation in the Southern Ocean and the ACC is responsible for redistributing deep-water formed in the North Atlantic to other basins such as the Indian and Pacific Oceans (Rintoul et al. 2001). Hence, fluctuations in the rate of the meridional overturning circulation in the Southern Ocean could, in turn, influence the global thermohaline circulation.

The SH oceans are also a key component of the global carbon cycle, sequestering ~60% of the total anthropogenic carbon dioxide (CO<sub>2</sub>) taken up by the oceans (Sabine et al. 2004). The fluxes of CO<sub>2</sub> between the Southern Ocean and atmosphere are directly influenced by surface winds and therefore fluctuations in the atmospheric circulation may also drive fluctuations in the rate of CO<sub>2</sub> uptake. Recent trends in the SH atmospheric circulation may have driven a weakening of the Southern Ocean CO<sub>2</sub> sink (Lovenduski et al. 2006), and this weakening may have had a significant impact on the global climate system.

While recent studies have provided considerable insight into the role of the SH oceans in the global climate system, there are still many aspects of SH ocean-atmosphere interaction that are relatively unexplored. The main goal of this dissertation is to comprehensively examine the mechanisms that generate variability in the extratropical SH SST field. In this chapter, I will first discuss the physical processes that regulate the heat budget of the ocean mixed layer and then provide a review of observed SST variability in the extratropical SH oceans.

### **1.1 Heat Budget of the Ocean Mixed Layer**

Before discussing the mechanisms that drive the observed SST variability in the SH oceans, it is worth first reviewing the components of the heat budget of the ocean mixed layer shown in Figure 1.1. The heat budget of the ocean mixed layer can also be expressed mathematically as:

$$\rho c_p H \frac{dSST}{dt} = SW_a - SW_o + LW_a - LW_s - F_{hf} + F_h - F_v \quad (1.1)$$

where  $c_p$  and  $\rho$  are the heat capacity and density of sea water, respectively;  $H$  is the depth of the mixed layer;  $SW_a$  is the incoming short-wave (solar) radiation;  $SW_o$  corresponds to the short-wave radiation that passes through the mixed layer;  $LW_a$  and  $LW_s$  correspond to long-wave radiation emitted from the atmosphere and surface, respectively;  $F_{hf}$  is the net surface turbulent heat flux (the sum of the sensible and latent heat fluxes); and  $F_v$  and  $F_h$  correspond to heat fluxed by vertical and horizontal transport, respectively.

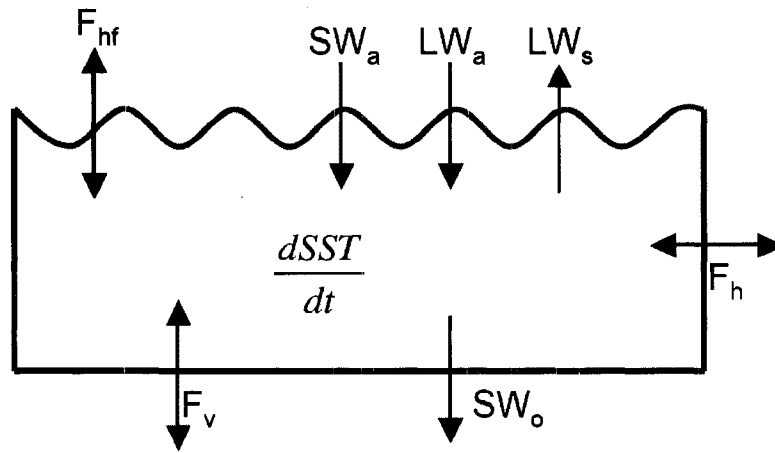


Figure 1.1. Heat budget of the ocean mixed layer.

Equation (1.1) states that the tendency in the temperature of the ocean mixed layer ( $dSST/dt$ ) is driven by the net exchange of heat with both the atmosphere and the surrounding ocean regions. The ocean mixed layer receives radiant energy in the form of short-wave (solar) radiation and long-wave radiation from the atmosphere, and it loses energy through long-wave radiation emitted by the surface. Energy is further exchanged through fluxes of latent and sensible heat at the air-sea interface and through lateral and vertical heat transport within the mixed layer. In the sections below, I will describe the contribution of each term in Eq. (1.1) to the total heat budget of the ocean mixed layer as

well as the relative contribution of each term to the generation of extratropical SST variability.

### *1.1.1 Radiative Heat Fluxes*

The radiative fluxes in Eq. (1.1) consist of the following terms: the net convergence of solar radiation in the mixed layer ( $SW_a - SW_o$ ), long-wave radiation emitted from the atmosphere  $LW_a$ , and long-wave radiation emitted from the surface,  $LW_s$ . These terms are described below.

The amount of solar radiation absorbed by the mixed layer is determined by the following two factors: 1) The amount of incoming short-wave radiation received at the surface, which depends on the net solar flux at the surface as well as the surface albedo. The albedo of the ocean is ~5% but varies as a function of wind speed, cloudiness, solar zenith angle, and the presence of sea-ice (Hartmann 1994); and 2) The amount of solar radiation that passes through the mixed layer, which is dependent on the optical depth of the mixed layer. As more dust, debris and biological life appear in the mixed layer, less radiation is able to pass through to deeper levels of the ocean, and hence more incident solar radiation is absorbed in the mixed layer.

Changes in the heat budget of the ocean mixed layer are also influenced by long-wave radiation emitted by both the atmosphere and the surface of the ocean. Long-wave radiation is strongly dependent on temperature ( $\propto T^4$ ). Thus, anomalously warm air temperatures will give rise to increased atmosphere-to-ocean long-wave fluxes at the surface of the mixed layer and anomalously warm ocean temperatures in the mixed layer will lead to increased ocean-to-atmosphere long-wave fluxes.

### 1.1.2 Surface turbulent heat fluxes

The net surface turbulent heat fluxes  $F_{hf}$  in Fig. 1.1 and Eq. (1.1) represent the transfer of sensible and latent heat across the air-sea interface and are described in further detail below.

A net sensible heat flux occurs in the presence of a vertical temperature gradient between the ocean mixed layer and the air directly above it. Heat is transferred across the air-sea boundary through the following two processes: conduction of heat from warmer to cooler regions via molecular activity and convection of heat by fluid motion. Within the first few millimeters above and below the air-sea interface, the flux of sensible heat occurs via conduction. However, because the atmosphere is a poor conductor of heat, beyond the thin layer of air above the interface, heat is dispersed throughout the boundary layer via mechanical turbulence and convection.

The most commonly used method to estimate the net sensible heat flux is the bulk aerodynamic formula (Hartmann 1994):

$$SH = c_p \rho C_{DH} U_r (T_s - T_a) \quad (1.2)$$

where  $c_p$  is the specific heat of air,  $\rho$  is the density of air,  $C_{DH}$  is the aerodynamic transfer coefficient for heat ( $\sim 10^{-3}$ ),  $U_r$  is the climatological wind speed and  $(T_s - T_a)$  is the temperature difference between the air at 10 m (denoted by subscript  $a$ ) and the surface of the ocean (denoted by subscript  $s$ ). Eq. (1.2) reveals that anomalously warm SSTs or cool surface air temperatures are associated with a net flux of sensible heat from the ocean to the atmosphere.

Fluxes of latent heat (e.g., evaporative cooling) arise from the energy needed to transform water from one state to another. For example, when water evaporates, energy is

extracted from the surface to convert the molecules from their liquid to gaseous state. The energy required to evaporate water is held latent (i.e., hidden) and later released when the reverse process occurs (e.g., condensation of water vapor into liquid cloud or fog droplets). The evaporation of water makes energy available to the atmosphere that would have otherwise gone into warming the surface.

The bulk aerodynamic form of the net latent heat flux is expressed as (Hartmann 1994):

$$LH = L_v \rho C_{DL} U_r (q_s - q_a) \quad (1.3)$$

$L_v$  corresponds to the latent heat of evaporation ( $2.5 \times 10^6$  J/kg).  $C_{DL}$  is the aerodynamic coefficient for water vapor ( $\sim 10^{-3}$ ). The last terms,  $q_s$ ,  $q_a$ , are the specific humidity at the surface and at 10 m, respectively.

Of all the components of the heat budget of the ocean mixed layer, the surface turbulent (sensible + latent) heat fluxes have the largest impact on extratropical SST variability on interannual and shorter time scales (e.g., Frankignoul and Reynolds 1983; Frankignoul 1985). Numerous observational studies have demonstrated that the dominant structures of extratropical SST variability in the NH are predominantly generated by the surface turbulent heat fluxes associated with the leading patterns of atmospheric variability (Bjerknes 1964; Cayan 1992a, b; Battisti et al. 1995; Visbeck et al. 2003) but as we will discuss in Section 1.2, the role of surface turbulent heat fluxes in driving the large-scale patterns of SST variability in the extratropical SH has not been extensively examined.

### 1.1.3 Horizontal transport of heat

The horizontal transport of heat  $F_h$  in Eq. (1.1) is primarily generated by the wind-driven circulation of the ocean. The steady-state, linearized equations of motion in the ocean can be written as (Pond and Pickard 1983):

$$\begin{aligned} -f(v_g + v_E) &= -\frac{1}{\rho} \frac{\partial p}{\partial x} + \frac{1}{\rho} \frac{\partial \tau^x}{\partial z} \\ f(u_g + u_E) &= -\frac{1}{\rho} \frac{\partial p}{\partial y} + \frac{1}{\rho} \frac{\partial \tau^y}{\partial z} \end{aligned} \quad (1.4)$$

where  $u$  and  $v$  are the zonal and meridional velocities, respectively; the subscripts  $g$  and  $E$  refer to the geostrophic and Ekman components of the flow, respectively;  $f$  corresponds to the Coriolis parameter,  $\rho$  is the density of sea water,  $p$  is the pressure and  $\tau$  is the surface wind stress. In the sections below, we describe the mechanisms through which the surface wind-stress and pressure gradient forces drive localized Ekman currents and large-scale geostrophic currents, which, in turn, drive fluctuations in the extratropical SST field.

#### 1) Transport of heat by Ekman currents

Ekman currents are the component of the wind-driven circulation balanced by the frictional surface wind-stress (i.e., the Coriolis torque acting on Ekman currents is balanced by the second term on the right-hand-side of Eq. 1.4). Assume that the ocean comprises of an infinite number of discrete layers: the wind stress acting upon the top layer of the ocean deflects the surface current  $45^\circ$  to the left of the wind direction in the SH. The next layer down does not “feel” the wind, but rather the layer above and below it, and is deflected slightly more to the left. The result is that, with increasing depth, the

flow not only gets weaker but is also directed increasingly to the left of the surface wind. Near the bottom of the Ekman layer, the current is oriented in the opposite direction of the surface wind.

The total transport within the Ekman layer is found by vertically integrating Eq. (1.4) over the depth of the wind-driven layer:

$$\begin{aligned} U_E &= \frac{\tau^y}{\rho f} \\ V_E &= -\frac{\tau^x}{\rho f} \end{aligned} \quad (1.5)$$

where  $U_E$  and  $V_E$  represent the transport of water in the wind-driven layer of the upper ocean via Ekman currents. Eq. (1.5) shows that the total Ekman transport is directed  $90^\circ$  to the left of surface wind stress in the SH and vice versa in the NH. Thus, equatorward Ekman heat transport is observed in the presence of westerlies and poleward Ekman heat transport is observed in the presence of easterlies.

The heat advection by the Ekman currents  $F_{Hek}$  can be written as (Marshall et al. 2001; Visbeck et al. 2003):

$$F_{Hek} = c_p \vec{M}_{ek} \cdot \nabla SST \quad (1.6)$$

where  $M_{ek}$  is the total Ekman transport in the zonal and meridional directions from Eq. (1.5). Eq. (1.6) states that heat advection by Ekman currents is dependent on the strength of the Ekman transport, which is a function of wind stress, as well as the gradients in the SST field. As a result, heat advection by Ekman currents strongly impacts variability in the SST field in the extratropics where strong surface winds and large SST gradients are observed. Ekman currents respond almost instantaneously to surface wind stress and therefore impact SST anomalies on relatively short time scales (i.e., less than a month).

Heat advection by Ekman currents (hereafter referred to as Ekman heat fluxes) generally plays a smaller role in generating large-scale extratropical SST patterns than surface turbulent heat fluxes on interannual time scales (Frankignoul and Reynolds 1983; Haney 1985; Frankignoul 1985; Luksch and von Storch 1992; Sterl and Hazeleger 2003). However, the Ekman heat fluxes are nevertheless crucial for obtaining the detailed structure and correct magnitude of the patterns of midlatitude SST variability (Seager et al. 2000; Haarsma et al. 2005; Alexander and Scott 2008). As is the case with the surface turbulent heat fluxes, the role of Ekman heat fluxes in driving the large-scale SST variability in the extratropical SH has not been extensively examined.

*2) Comments on the transport of heat by geostrophic currents and the thermohaline circulation*

Geostrophic currents are the component of the wind-driven circulation driven by pressure gradient forces (i.e., the Coriolis torque acting on the geostrophic currents is balanced by the first term on the right hand side of Eq. 1.4). Unlike Ekman currents, geostrophic currents do not respond instantaneously to fluctuations in the surface wind stress field. Consequently, the role of temperature advection by geostrophic currents in generating SST variability will dominate decadal time scales but will be less important than surface turbulent and Ekman heat fluxes on interannual and shorter time scales (Frankignoul and Reynolds 1983; Saravanan and McWilliams 1998). More details on the geostrophic flow in the Southern Ocean and, in particular the Antarctic Circumpolar Current, are provided in Section 1.2.3.

In addition to the wind-driven circulation, the ocean also transports heat horizontally via the thermohaline circulation. For example, the poleward heat transport within the Gulf Stream is driven partly by the wind-driven gyre circulation and partly by the circulation required to compensate for deep-water formation in the high latitudes of the North Atlantic. Variations in the rate of deep-water formation will give rise to variations in the horizontal heat transport. However, like the geostrophic currents, the impact of the thermohaline circulation on horizontal heat transport in the ocean mixed layer is more likely to affect SST anomalies on interdecadal rather than monthly time scales.

#### *1.1.4 Vertical transport of heat*

The effect of vertical heat transport  $F_v$  on the heat budget of the ocean mixed layer (Eq. 1.1) occurs primarily through two mechanisms: 1) variations in the depth of the mixed layer and 2) vertical motion driven by the horizontal convergence and divergence of surface Ekman currents.

##### *1) Variations in the depth of the mixed layer*

Variations in the depth of the mixed layer are predominantly associated with convection (i.e., surface cooling deepens the mixed layer through buoyancy effects) and mechanical mixing (i.e., strong surface winds will induce more vertical mixing than weak winds). As a result, a shoaling of the mixed layer will detrain anomalous SSTs and a deepening of the mixed layer will entrain anomalous temperatures from below. Note that the depth of the mixed layer, which corresponds to vertical extent of mixing in the upper

ocean, is not necessarily equal to the depth of the Ekman layer, which corresponds to the vertical extent of influence by surface wind stress.

Variations in the mixed layer depth also affect the persistence of SST anomalies. The subduction and re-entrainment of SST anomalies associated with the seasonal cycle of the depth of the mixed layer gives rise to the winter-to-winter persistence of extratropical SST anomalies, a process termed “reemergence” by Alexander and Deser (1995). Reemergence was first noted by Namias and Born (1970, 1974), who found that extratropical SST anomalies tend to persist from one winter to the next but not through the intervening summer. They hypothesized that SST anomalies extending deep into the mixed layer are sequestered beneath the shoaling mixed layer during the spring and thus are insulated from the surface and atmospheric variability. When the mixed layer deepens in the subsequent fall, the sequestered thermal anomalies are re-entrained back into the mixed layer. Consequently, reemergence does not directly generate extratropical SST anomalies but accounts for their year-to-year persistence (Deser et al. 2003).

Evidence of reemergence has been widely documented across the North Atlantic (Alexander and Deser 1995; Watanabe and Kimoto 2000; Coetlogon and Frankignoul 2003; Timlin et al. 2002) and North Pacific (Alexander and Deser 1995; Alexander et al. 1999) basins. However, there is only sparse observational evidence of reemergence in the SH ocean basins, which will be discussed in more detail in Section 1.2.

## *2) Convergence and divergence of Ekman currents*

The vertical transport of heat into the mixed layer is also driven by the convergence and divergence of the horizontal surface Ekman currents. Combining the

horizontal derivative of Eq. (1.5) with the continuity relationship reveals that the vertical velocity at the base of the Ekman (i.e., wind-driven) layer is directly proportional to the curl of the wind stress (Hartmann 1994):

$$w_E = \hat{k} \cdot \nabla \times \left( \frac{\vec{\tau}}{\rho f} \right) \quad (1.7)$$

Consequently, regions of cyclonic wind stress in the SH will drive convergence of the horizontal Ekman currents, which, in turn, generates sinking motion at the base of the ocean mixed layer. The opposite is true in regions of anti-cyclonic wind stress. Vertical heat transport by Ekman pumping/sinking primarily generates SST anomalies on relatively small spatial scales and has less influence on large-scale patterns of SST variability (Frankignoul 1985). Note that the horizontal divergence/convergence of Ekman currents is responsible for the pressure gradient forces that give rise to geostrophic currents.

### *1.1.5 The null hypothesis of extratropical SST variability*

Of all the mechanisms given in Eq. (1.1), and described above, the surface turbulent heat fluxes and, to a lesser extent, Ekman heat fluxes generally have the largest impact on large-scale extratropical SST variability on month-to-month timescales (e.g. Frankignoul and Reynolds 1983; Frankignoul 1985). The response of the ocean mixed layer to changes in the surface turbulent and Ekman heat fluxes associated with random atmospheric forcing is frequently used as a benchmark for assessing the importance of other physical processes in the ocean and is thus often considered a “null hypothesis” for extratropical SST variability.

The response of the ocean mixed layer to surface turbulent heat fluxes was first extensively examined in a simple stochastic climate model by Frankignoul and Hasselman (1977; hereafter FH77). By excluding the radiative and transport terms in Eq. (1.1) and assuming a mixed layer of fixed depth  $H$ , the model developed in FH77 explicitly examined the SST response to stochastic atmospheric forcing characterized by surface heat fluxes. The FH77 model is given as:

$$\rho c_p H \frac{dT'}{dt} = F' - \lambda T' \quad (1.8)$$

where  $\rho$  is the density of seawater,  $c_p$  is the heat capacity of the ocean, and the last term on the right hand side denotes the damping of the SST anomalies via a constant feedback factor  $\lambda$  (e.g., Newtonian cooling). The damping  $\lambda T'$  corresponds to a highly idealized representation of the ocean-to-atmosphere sensible and latent fluxes associated with  $T'$  (Frankignoul and Hasselman 1977; Barsugli and Battisti 1998; Deser et al. 2003). The feedback factor  $\lambda$  is estimated from bulk aerodynamic formula (e.g., Eqs. 1.2 and 1.3) and is dependent on the surface winds, surface temperature, and relative humidity.

The model developed in Frankignoul and Hasselman (1977) reveals that the large thermal inertia of the mixed layer of the ocean renders it sensitive to only the low-frequency part of the atmospheric forcing. Hence, the SST field has a spectrum consistent with red-noise and an  $e$ -folding time scale as large as  $\sim 3$ -5 months, despite the fact the atmospheric forcing may have a decorrelation timescale of only a few days.

The FH77 model is often viewed as a null hypothesis for understanding extratropical SST variability. However, the model in Eq. (1.8) is a simplification of extratropical ocean-atmosphere interaction and cannot account for other characteristics of

the SST field such as mixed layer processes, ocean-atmosphere coupling, or the effects of the thermohaline circulation. By extending the FH77 model to include the effects of the seasonal cycle of the mixed layer depth, Deser et al. (2003) showed that white noise atmospheric forcing can give rise to wintertime SST anomalies with an *e*-folding timescale of up to ~two years.

## **1.2 Observations of Large-Scale Extratropical SST Variability in the Southern Hemisphere**

In the previous sections, we reviewed the heat budget of the ocean mixed layer and the relative importance of different physical factors for fluctuations in extratropical SST field. The primary mechanisms that drive SST anomalies are surface turbulent heat fluxes and, to a lesser extent, heat advection by Ekman currents. Variations in the depth of the mixed layer are inversely proportional to the tendency in SSTs, thus impacting the amplitude and persistence of SST anomalies generated by the heat fluxes.

A large fraction of the observational studies that have examined the relative contributions of different mechanisms to extratropical SST variability have focused on the North Atlantic and North Pacific oceans. This is primarily because of the high quality and quantity of ocean observations in the extratropical Northern Hemisphere (NH) relative to the SH. For example, until the late 1970s/early 1980s, most sea surface temperature observations were measured in situ onboard ships crossing between major population centers in North America, Europe and Asia. Relative to the NH, the number of ships crossing the SH ocean basins is small, and thus there are fewer in situ SST observations available in the Southern Ocean (e.g., Reynolds and Smith 1994).

The lack of in situ temperature observations in the SH has prevented extensive analysis of large-scale variability in the Southern Ocean until global satellite-derived SST data became available starting in the late 1970s/ early 1980s. Thus, there are now several decades of satellite-derived SST observations available for the SH oceans, a period long enough to warrant detailed explorations of variability in the extratropical SH SST field.

Figure 1.2 shows a schematic of the heat budget of the ocean mixed layer with the contributions of different SH climate phenomena highlighted on the figure. In this section, we will discuss the role of all of these phenomena in driving variability in the SH SST field.

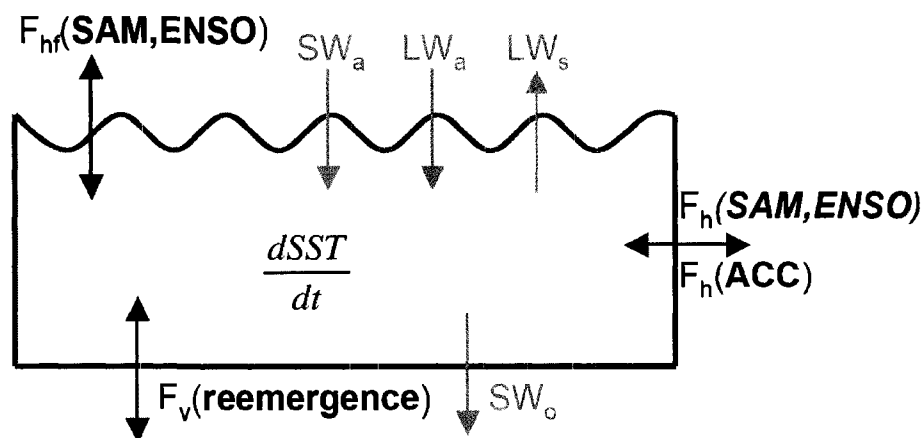


**Figure 1.2. Heat budget of SH ocean mixed layer. The mechanisms in bold-face are discussed in Section 1.2.**

### *1.2.1 Leading modes of Southern Hemisphere atmospheric variability and associated patterns of SST anomalies*

As discussed in Section 1.1, changes in the surface turbulent heat fluxes associated with large-scale variability in the atmospheric circulation play a key role in

generating large-scale SST anomalies on interannual timescales. Here, we review large-scale structures of extratropical SH atmospheric variability and their associated patterns of SST anomalies.

Large-scale atmospheric variability in the SH is dominated by two patterns of climate variability: the Southern Annular Mode (SAM) and the remote SH response to the El-Niño Southern Oscillation phenomenon (ENSO). The SAM is characterized by nearly zonally symmetric north-south vacillations in the latitude of the midlatitude atmospheric westerly jet (Kidson 1988; Karoly 1990; Thompson and Wallace 2000). The high index polarity of the SAM is defined as periods when the midlatitude jet is contracted poleward, and thus when the flow poleward of 50°S is anomalously westerly and pressures over the SH polar region are anomalously low. The low index polarity of the SAM is defined by anomalies in the opposite sense. The SAM has a timescale of ~10 days (Lorenz and Hartmann 2001), is believed to reflect a positive feedback between the zonal flow and transient eddies in the SH storm track (Lorenz and Hartmann 2001), and explains ~25% of the month-to-month variability in the SH geopotential height field (Kidson 1988; Karoly 1990; Thompson and Wallace 2000).

In contrast to the zonally symmetric structure of the SAM, the SH atmospheric response to ENSO is predominantly wave-like (e.g., Karoly 1989; Kiladis and Mo 1998; Kidson and Renwick 2002). During the warm phase of the ENSO cycle (i.e., El Niño conditions), increased convection in the central tropical Pacific creates anomalous upper level vorticity, which is advected poleward in the upper tropical troposphere by the mean meridional circulation (Sardesmukh and Hoskins 1988). From the subtropics, the anomalous vorticity excites a pattern of standing Rossby waves extending from the

subtropics towards North America in the NH and the Southern Ocean in the SH (Hoskins and Karoly 1981). In the SH, the wave train associated with the warm phase of ENSO is characterized by cyclonic anomalies to the west of New Zealand, anti-cyclonic anomalies to the west of the Antarctic Peninsula and cyclonic anomalies off the east coast of southern South America (Karoly 1989).

A complicating factor in interpreting large-scale SH atmospheric variability is that during austral summer, the remote response to ENSO includes not only the wave-like response noted above, but also a component that projects onto the SAM (L'Heureux and Thompson 2006). Thus the impacts of the SAM and ENSO on high latitude SH climate bear strong resemblance to each other during the SH summer season.

The impact of the SAM on variability in the extratropical SH SST field has been examined in only a handful of observational and modeling studies (e.g., Watterson 2000; Hall and Visbeck 2002; Holland et al. 2005; Lovenduski and Gruber 2005; Verdy et al. 2006; Sen Gupta and England 2006). Observations reveal the pattern of SST anomalies associated with the high index polarity of the SAM is marked by predominantly warm SST anomalies along 30°-40°S, cold SST anomalies along 50°-60°S, and a broad region of enhanced cold SST anomalies in the Southern Ocean centered near 50°S, 130°W (Lovenduski and Gruber 2005; Sen Gupta and England 2006). Numerical results reveal a qualitatively similar impact of the SAM on the SST field (e.g., Hall and Visbeck 2002; Holland et al 2005; Sen Gupta and England 2006), though in general the climate model ocean response to the SAM is more zonally symmetric than the observations (e.g., Hall and Visbeck 2002). Verdy et al. (2006) note a large fraction of SST variability in the vicinity of the ACC is consistent with surface turbulent and Ekman heat fluxes associated

with variability in the SAM as well as ENSO. Meredith et al. (2004) argue the SAM impacts ocean transport through the Drake Passage and Meredith and Hogg (2006) reveal the SAM drives anomalies in kinetic energy in the Antarctic Circumpolar Current (ACC). LeFebvre et al. (2004) demonstrate that the SAM influences the distribution of sea-ice around Antarctica.

The pattern of SST anomalies associated with the extratropical SH response to ENSO has also been described in a select number of observational and modeling studies (e.g., Li 2000; Renwick 2002; Kidson and Renwick 2002; Holland et al 2005; Verdy et al. 2006). The SH SST response to ENSO is primarily associated with a dipole in SST anomalies between the region to the north of New Zealand and near the region centered near 50°S, 140°W. The pattern of SST anomalies associated with ENSO is similar to the leading Empirical Orthogonal Function (EOF) of extratropical SH SST anomalies (Kidson and Renwick 2002).

While the relationships between extratropical SH SST anomalies and large-scale patterns of atmospheric variability have been documented in several studies, the physical processes that drive these relationships have not been comprehensively analyzed. Thus, one goal of this study is to examine the role of surface turbulent heat fluxes and heat advection by Ekman currents in generating SST anomalies associated with the SAM and the remote SH response to ENSO.

### *1.2.2 Reemergence of wintertime SST anomalies*

The reemergence of wintertime SST anomalies has been extensively documented in the extratropical NH ocean basins, but has received only cursory attention in the

extratropical SH, presumably because of the lack of Southern Ocean subsurface ocean temperature observations. Hadfield (2000) noted that SST anomalies in the southeast Tasman Sea recur from early spring to the following fall/winter. Hanawa and Sugimoto (2004) noted in several datasets that SST anomalies also exhibit winter-to-winter persistence in the central South Atlantic, the western Indian, and the western South Pacific Oceans.

The studies mentioned above relied primarily on satellite-derived SSTs, and to our knowledge no study has confirmed the existence of reemergence in the SH using subsurface temperature observations. Thus, another goal of this study is to examine the reemergence of wintertime SST anomalies in the extratropical SH ocean using subsurface temperature observations.

### *1.2.3 The Antarctic Circumpolar Current*

As discussed in Section 1.1.3, the contribution of horizontal heat transport by large-scale currents to month-to-month variability in the SST field is generally weak compared to, say, surface turbulent heat fluxes over much of the extratropical oceans. Obvious exceptions are regions of strong western boundary currents such as the Kuroshio and Gulf Stream. The transport of heat by ocean currents in the SH ocean basins is further unique in that the basins are connected by the Antarctic Circumpolar Current (ACC), which is responsible for zonal transport of heat around the SH ocean basins. Several studies suggest the SAM may impact the Southern Ocean current systems including the ACC. In this section, we review the physical mechanisms that drive the ACC including its relationship with variability in the SAM.

The lack of physical barriers in the SH around  $\sim 60^\circ\text{S}$  allows the ACC to encircle the globe uninterrupted by land. The eastward flow of the ACC is driven by the overlying surface westerlies. In the SH, the net Ekman transport in the wind-driven layer is directed  $90^\circ$  to the left of the surface winds, and hence the Ekman transport creates a gradient in sea surface heights from middle latitudes towards the Antarctic continent. The resulting pressure gradient force is balanced by the Coriolis force acting on the eastward flow.

The ACC is characterized by a series of circumpolar temperature fronts including the Polar Front and the Sub-Antarctic Front. The Sub-Antarctic front also marks the equatorward boundary of the ACC. The poleward boundary of the ACC is defined as the poleward edge of the Upper Circumpolar Deep Water (Orsi et al. 1995). The boundaries of the ACC can also be defined as the northernmost and southernmost lines of constant sea surface height that encircle the globe uninterrupted by land (Karsten and Marshall 2002).

Compared to other major currents, such as the Gulf Stream and Kuroshio, the ACC is relatively slow. The overall speed is  $\sim 0.15\text{-}0.2$  m/s but localized speeds can reach 1m/s (the Gulf Stream exhibits average speeds of 1-2 m/s). However, the ACC extends 2-4 km deep and 2000 km wide, and thus, on average, it transports  $\sim 130$  Sv with a maximum transport of 150 Sv along the Drake Passage (Whitworth 1983; Whitworth and Peterson 1985; Peterson 1988). The Gulf Stream transports  $\sim 80$  Sv near Cape Hatteras and  $\sim 150$  Sv near  $65^\circ\text{W}$  (Hogg 1992; Johns 1995; Hogg and Johns 1995).

Because the ACC is primarily driven by surface winds, variations in the intensity of the current are linked to variations in the atmospheric circulation. For example, in the positive phase of the SAM, the region of largest westerly surface wind stress shifts

poleward, which might give rise to a poleward intensification of the ACC, which in turn should give rise to enhanced equatorward Ekman transport across the ACC (Hall and Visbeck 2002). Hence, the shift towards the positive phase of the SAM over the past 30 years may have important implications for heat transport within the ACC (Meredith et al. 2004; Fyfe and Saenko 2006). The ACC is also thought to exhibit low-frequency intrinsic variability arising from a positive feedback between mesoscale eddies generated by baroclinic instability and the mean circulation (Hogg and Blundell 2006).

The strong eddy activity observed in association with the strong temperature fronts of the ACC is responsible for the poleward flux of heat that balances the equatorward flux of heat by Ekman currents (de Szoeke and Levine 1981). A recent study by Meredith et al. (2006) has demonstrated that enhanced eddy activity along the ACC is preceded by increases in surface wind stress associated with the positive phase of the SAM. It was further suggested by Meredith et al. (2006) that the recent trends in the SAM could lead to a positive trend in poleward heat fluxes across the ACC which, in turn, could potentially lead to the observed warming of the SH circumpolar ocean as noted by Gille (2002).

### **1.3 Objectives**

The goal of this research is to provide the first comprehensive investigation of the physical processes that drive fluctuations in the extratropical SH SST field. In particular, we will evaluate the role of the surface turbulent and Ekman heat fluxes in generating large-scale patterns of SST variability in the SH; we will assess the impact of variations in the mixed layer depth on the persistence of large-scale patterns of SST anomalies; and

we will examine the winter-to-winter reemergence of SST anomalies in the extratropical SH.

The rest of the dissertation is organized as follows. Chapter 2 describes the data, methodology and statistical analysis used in the present research. Chapter 3 provides a comprehensive summary of the observed relationships between large-scale SH patterns of atmospheric variability and the extratropical SST field. It also examines the role of surface turbulent and Ekman heat fluxes in driving the observed SST patterns. Chapter 4 analyzes weekly SST data to evaluate the temporal evolution of the relationships between the SAM and the extratropical SH SST field, and it examines in detail the impact of variations in mixed layer depth on the persistence of the SAM-related SST anomalies. Chapter 5 uses subsurface and surface temperature observations to evaluate the reemergence of winter SST anomalies in the extratropical South Pacific Ocean. Chapter 6 offers a summary and discussion of the major findings of the study and proposes possible future research.

## CHAPTER TWO DATA AND METHODOLOGY

### 2.1 Data

The poor sampling of the Southern Hemisphere (SH) ocean basins limits the amount of data available to extensively analyze the extratropical sea surface temperature (SST) field. The majority of the SH ocean temperature data are restricted in terms of spatial/temporal resolution and measurement capabilities, and hence one goal of the present study is to examine the ocean temperature field in as many independent datasets as possible. In this section, we describe the data sets used in this study and discuss their relative advantages and limitations. The ocean temperature datasets are also summarized in Figure 2.1.

#### *2.1.1 Sea surface temperature data*

The most comprehensive collection of global in situ SST observations is the International Comprehensive Ocean-Atmosphere Data Set (ICOADS) provided by the National Oceanographic and Atmospheric Administration (NOAA)/ Earth System Research Lab (ERSL) Physical Sciences Division (PSD), Boulder CO, USA from their website at <http://www.cdc.noaa.gov/>. ICOADS was developed in the early 1980s by the Earth Research Laboratory (ERL), the Cooperative Institute for Research in Environmental Sciences (CIRES) and the National Climatic Data Center (NCDC) with the goal of creating a historical ocean climate record extending back to the mid-1850s,

when uniform records of in situ measurements began. A large fraction of the observations in ICOADS are measured onboard ships from insulated buckets, hull contact sensors and engine intakes (Woodruff et al. 1987). Beginning in the 1970s, these observations were supplemented with data from drifting and moored buoys in regions of sparse ship-based measurements. The SST data from the buoys are measured using thermistors and hull contact sensors and then relayed in real-time by satellites.

The ICOADS are available in monthly-mean format on both  $1^{\circ} \times 1^{\circ}$  latitude/longitude and  $2^{\circ} \times 2^{\circ}$  latitude/longitude grids for the periods 1960-present and 1800-present, respectively. In addition to SSTs, ICOADS also archives measurements of air temperature, scalar winds, vector winds in the zonal and meridional directions, sea level pressure, total cloudiness and specific humidity.

The primary advantage of ICOADS is the period of record, which is long enough to examine variability in the ocean on interannual to interdecadal time scales. However, the spatial sampling of the data is generally sparse because, as mentioned in Chapter 1, the majority of the SST observations were measured onboard ships crossing between major population centers, which are concentrated in the Northern Hemisphere (NH). As shown in Figure 2.2, “snapshots” of the SH SST field demonstrate that data coverage equatorward of  $30^{\circ}\text{S}$  has improved over the past several decades, but observations poleward of  $30^{\circ}\text{S}$  remain sparse.

Beginning in the late 1970s, observations of SSTs derived from satellite retrievals from the Advanced Very High Resolution Radiometer (AVHRR) became available. The AVHRR is a broadband, 4- or 5-channel scanning radiometer, sensing in the visible, near infrared, and thermal infrared portions of the electromagnetic spectrum (Kidwell et al.

1991, 1995). It has been operational since 1979 onboard the NOAA -7, -9, -11, -14, -16 and -17 polar orbiting satellites. The AVHRR has a true resolution of 1.1 km at nadir and makes measurements twice daily.

The AVHRR-derived SST data are available in weekly and 5-day averages (i.e., pentads) on 9 km and 18 km global latitude/longitude grids. Consequently, the spatial coverage of satellite-derived SST observations is a vast improvement from in situ SST observations, which are especially lacking in the SH. The primary disadvantage of the AVHRR retrievals is the inability of the infrared satellite to “see” through the clouds to the surface. As a result, the AVHRR-derived SSTs cannot be measured in 100% cloud-covered regions. Measurements made in partially cloud-covered regions create a negative bias in SSTs since cloud top temperatures are colder than SSTs. Increased aerosol concentration (e.g. from volcanic eruptions) can also induce a negative bias in the satellite retrievals.

The NOAA Optimum Interpolation (OI) SST analysis is a blended product, combining both in situ and AVHRR satellite-derived observations of SSTs (Reynolds and Smith 1994; Reynolds et al. 2002). In situ data are not only critical for satellite calibration and validation but are also used to correct the satellite biases mentioned above (Reynolds 1988; Reynolds and Marsico 1993).

Once the satellite biases have been removed, the in situ and satellite-derived observations are blended in the NOAA OI SST data by using the optimum interpolation technique outlined in Gandin (1963). In this case, OI SST values for all weeks are calculated at each  $1^{\circ} \times 1^{\circ}$  grid point as the sum of the SST value from the previous week and an analysis increment that is determined from the observations (both satellite and in

situ) for the current week. The analysis increments and final SST values are determined at every  $1^{\circ}\times 1^{\circ}$  grid point as follows:

1. The so-called "data increments" are calculated as the differences between the gridded  $1^{\circ}\times 1^{\circ}$  SST value from the previous week and the values at all available observations within a  $4^{\circ}\times 4^{\circ}$  box centered on the gridded SST value. The number of observations available for the current week determines the number of data increments used in the calculations. For example, if there are 10 observations within the  $4^{\circ}\times 4^{\circ}$  grid box, then 10 data increments are calculated.
2. Weights for the data increments are calculated on the basis of the following: 1) the distance between the center of the grid box and the observation (i.e., observations further away from the grid box center will be weighted less than observations nearby) and 2) the covariance and variance errors of the previous week's SST value and the data increments (i.e., larger errors will be weighted less).
3. The data increments are multiplied by their respective weights and then summed to produce the so-called analysis increment for the  $1^{\circ}\times 1^{\circ}$  grid box in question.
4. The gridded  $1^{\circ}\times 1^{\circ}$  SST value for the current week is calculated by adding the resulting analysis increment to the SST value for the previous week.

Steps 1-4 are repeated for each week for the period 1981-present. The OI SST analyses are available in weekly and monthly-mean formats on a  $1^{\circ}\times 1^{\circ}$  latitude/longitude grid for the period November 1981-present.

The quality of the OI SST analyses is impacted by several factors. Sampling variability may arise in regions of dense cloud cover and sparse in situ measurements because the AVHRR cannot penetrate the clouds to measure temperatures at the ocean

surface. This is particularly true in the extratropical South Pacific where there are few ship observations and the percentage of annual mean cloud coverage exceeds 75% (O'Neill et al. 2003).

Another complicating factor is the noise induced by the bias correction to the satellite data. In most cases, the satellite bias persists from one week to the next but the quantity of available in situ data used to correct the bias varies on a weekly basis. Consequently, the bias correction varies slightly due to weekly changes in the sparse in situ data even though the bias itself remains the same (Reynolds 1988; Reynolds and Marsico 1993). The resulting lack of continuity in the bias correction from one week to the next introduces a small amount of noise into the data. To reduce the noise, a 3-point binomial filter is typically applied to the SST field in space and time (O'Neill et al. 2003; Reynolds et al. 2002).

A more recent satellite-derived SST product is obtained from the Advanced Microwave Scanning Radiometer for the Earth Observing System (AMSR-E), a multi-channel passive microwave radiometer. The data are provided by the Remote Sensing Systems website ([www.ssmi.com](http://www.ssmi.com)). The AMSR-E was launched onboard the National Aeronautics and Space Administration (NASA) Aqua satellite in May of 2002. The Aqua satellite is a sun-synchronous polar orbit (i.e., observations are measured for a given geographical location at the same time every day) and retrieves data for both ascending (local daytime) and descending (local nighttime) portions of the orbit. The data are available in daily, weekly and monthly format on a global  $0.25^{\circ} \times 0.25^{\circ}$  latitude/longitude grid. The radiometer also measures wind speed, atmospheric water vapor, cloud water and rain rate.

The primary advantage of the AMSR-E SST data over the OI SST data is that the microwave radiometer can penetrate through thick cloud layers to measure temperatures at the surface. Therefore, the AMSR-E data provide higher quality measurements of SSTs than the AVHRR-based OI SST data in regions of persistent cloudiness and sparse in situ measurements such as the South Pacific. Unfortunately, the AMSR-E instrument has only been collecting data since June 2002, which is not long enough to perform extensive statistical analysis of variability in the SST field.

### *2.1.2 Subsurface temperature data*

The most extensive collection of historical ocean profile data is the World Ocean Database (WOD) archived by the NOAA National Oceanographic Data Center (NODC). The primary goal of the WOD is to provide a comprehensive set of ocean data that can be used to study the temporal and spatial variability of the physical, biological and chemical parameters in the ocean. The database consists of in situ measurements of 28 variables including temperature, salinity, pressure, nutrients and several tracers from 11 different datasets. Temperature, the primary variable used in this study, is obtained primarily from the following four sources:

1. Ocean Station Data (OSD). The OSD comprise the most comprehensive set of discrete ocean measurements extending back to 1772. Observations are recorded at depths in excess of 1000 m from stationary research ships using manual reversing thermometers. A large fraction of the observations are taken from bottles and buckets, and therefore the data set is also collectively referred to as “bottle data”.

2. High-resolution Conductivity-Temperature-Depth (CTD) data. CTD data extend back to the early 1960s. Conductivity measurements are recorded from the instrument along with pressure and temperature and then values of salinity are derived. Measurements can be made as deep as 10 km but are usually sampled to shallower depths.
3. Mechanical bathythermograph (MBT) profiles. The MBT data were initially developed in the late 1930s. The MBT contains a temperature sensor and a pressure-sensitive Bourdon tube. As the instrument is dropped through the water, the temperature and pressure are recorded at depths up to ~300 m.
4. Expendable Bathythermograph (XBT) probes. By the mid-1960s, MBTs were replaced by XBT probes, which are dropped beneath research vessels, submarines, and aircraft. Temperatures are measured to depths greater than 1000-m using a thermistor located within an expendable probe.

The first World Ocean Database (WOD) was created in 1998 with over 5 million profiles of ocean data from around the world extending back before 1800. The most recent version of WOD was released in 2005 and contains approximately 8 million profiles, including data from more than 164,000 cruises made by 93 countries (Boyer et al. 2006). Data have also been collected from 150 ships, drifting and moored buoys and profiling floats.

The primary limitation of the WOD is the sparse and uneven spatial and temporal coverage of the data. However, the subsurface data coverage has improved dramatically in the past decade with the development of the ARGO network, an array of 3000

profiling floats used to systematically measure temperature and salinity down to 2000 m every 10 days. Measurements are obtained as follows: first water is pumped into an external bladder attached to the float which then rises to the surface over a period of approximately 6 hours. During ascent, the float records temperature and salinity at various depths. At the surface, the measurements as well as the position of the float are transmitted to a satellite. The float then submerges again (as the bladder deflates) and the cycle repeats.

Deployment of the ARGO profiling floats began in 2000 and the array was completed in November 2007. The final array of 3000 floats will ideally provide 100,000 profiles of temperature, salinity and velocity measurements every year, distributed across the world ocean at an approximately  $3^{\circ} \times 3^{\circ}$  spacing. Data are only collected in ice-free zones and therefore measurements are sparse poleward of  $60^{\circ}\text{S}$ .

ARGO is the first data set to provide a systematic measurement of the physical state of the upper ocean, but the temporal record is short, particularly in the SH ocean basins. Deployments began in 2000 but the majority of the profiles were placed in the NH basins. It was not until 2004-2005 that a substantial number of ARGO profiles were deployed in the SH. Hence, the temperature profiles from the WOD extend over several decades but have poor spatial resolution, whereas the ARGO data have dense spatial resolution but a very short temporal record.

Recently, the UK Met Office Hadley Centre has created a more comprehensive data set combining upper ocean temperature profiles from both the WOD and ARGO called the ENSEMBLES (EN3; Ingleby and Huddleston 2007). The WOD and ARGO measurements are supplemented in the EN3 data by temperature profiles from the Global

Temperature Salinity Profile Program (GTSP). An automated quality control system is applied to the temperature profiles from the three sources and duplicate profiles are discarded.

In the ENSEMBLES data, which extend back to 1950, all individual months contain profiles of temperature for a given location (latitude/longitude) and depth (in meters). The number and locations of the profiles varies from month-to-month, but each profile contains temperature measurements at a maximum of 150 depths. Neither the locations of the profiles nor the depths at which temperatures are measured are regularly spaced. For example, January 1990 contains 9646 profiles of temperatures. During January 1990, the profile at, for example, 30°N, 22°W contains 141 temperature values at irregularly spaced depths from 0-2000 m whereas the profile at, for example, 61°S, 57°W, contains 79 temperature values at irregularly spaced depths from 0-300 m. A more detailed discussion of the methodology used to convert these profiles into time series of temperature at standard depths will be provided in Chapter 5 when the subsurface data are analyzed.

### *2.1.3 Mixed layer depth data*

The mixed layer depth data were obtained from the Ocean Mixed Layer Depth Climatology dataset ([www.lodyc.jussieu.fr/~cdblod/mld.html](http://www.lodyc.jussieu.fr/~cdblod/mld.html)), as described in de Boyer Montégut et al. (2004). The data are derived from over four million vertical temperature profiles of the upper ocean from both the WOD and the World Ocean Circulation Experiment (WOCE) between 1941 and 2002. The depth of the mixed layer is defined as the shallowest depth at which the temperature differs from the temperature at 10 m by

0.2°C. The data are available in monthly-mean format on a 2°x2° latitude/longitude mesh.

#### *2.1.4 Sea surface height data*

The sea surface height (SSH) observations were obtained from the University of Texas at Austin Center for Space Research (UT/CSR) dynamic ocean topography database (<ftp.csr.utexas.edu>), which contains gridded sea surface heights derived from TOPEX/POSEIDON altimeter measurements. All the sea surface heights are referenced to the geoid computed from the Joint Gravity Model (JGM-3). The data are available in monthly-mean format on a 1°x1° latitude/longitude grid from October 1992 to February 1995.

#### *2.1.5 Atmospheric data*

The atmospheric variables used throughout the study are geopotential height, surface winds, and surface turbulent heat fluxes produced by the National Centers for Environmental Prediction-National Center for Atmospheric Research (NCEP-NCAR) reanalysis project provided by the NOAA/OAR/ERSL/PSD (Kalnay et al. 1996; Kistler et al. 2001). The reanalysis data consist of measurements from land surface, ships, rawinsonde, aircraft, and satellite data, all of which are quality controlled using a data assimilation system that is frozen over the period 1957-1995 to prevent climatic jumps from changes in the model. As part of the assimilation system, the NCEP operational model dynamically interpolates the data using 6-hour forecasts.

The NCEP reanalysis data are available at 6-hour intervals on global  $2.5^{\circ} \times 2.5^{\circ}$  latitude/longitude grids for 17 vertical levels from 1948 to present. The geopotential height and surface wind fields are mostly obtained from observations. The surface turbulent heat fluxes (latent+sensible) are derived from bulk flux algorithms similar to those described in Eqs. (1.2) and (1.3). The flux data are derived solely from NCEP model-forced fields with no direct influence from observed variables. Positive values denote fluxes of heat into the ocean, and vice versa.

The reanalysis is also used to calculate the heat advection by Ekman currents (hereafter referred to as Ekman heat flux). The Ekman heat fluxes are derived using surface winds and the climatological mean SST field and are calculated as follows: First, the zonal and meridional surface wind stress is calculated from the surface wind field. Second, the surface wind stress fields are divided by the density of seawater ( $\rho=10^3$  kg/m<sup>3</sup>) and the Coriolis parameter ( $f=10^{-4}$ s<sup>-1</sup>) to obtain the Ekman heat transport (Eq. 1.5). Lastly, the Ekman heat flux is evaluated by taking the dot product of the Ekman heat transport and the gradient of the climatological mean SST field (Eq. 1.6). Positive (negative) values of Ekman heat flux denote anomalous convergence (divergence) of heat.

The Southern Annular Mode (SAM) and El Niño Southern Oscillation (ENSO) indices used in the study were obtained from the NOAA Climate Prediction Center (CPC). Daily (monthly) mean values of the SAM index are found by projecting the daily (monthly) 700 mb height anomalies poleward of 20°S onto the leading empirical orthogonal function of monthly-mean 700 mb heights, calculated for the period 1979-2000. As described in Chapter 1, the high index polarity of the SAM is characterized by

negative height anomalies over the pole surrounded by positive height anomalies between 40°-50°S. Monthly-mean variability in ENSO is defined on the basis of SST anomalies averaged over the region 5°S-5°N, 170°-120°W. In all analyses, the resulting cold-tongue index (CTI) is inverted such that positive values of the index correspond to the cold phase of the ENSO cycle, and vice versa. Before all analyses, the SAM and ENSO indices were standardized by subtracting the long-term means and dividing by the long-term standard deviations of the respective analysis periods.

## **2.2 Methodology**

In Chapters 3 and 4, the primary dataset used to analyze variability in the SH SST field (20°-80°S, 0°-360°E) is the OI SST analysis (1981-2007) described in Section 2.1. The ICOADS and AMSR-E SST data are used to supplement the results of the OI SST data. SST values below the threshold value of -1.8°C, the freezing point of seawater, were considered unphysical and were omitted from the analysis. Both weekly and monthly-mean SST values are used. For the NCEP analysis and SAM index, which are only available in monthly and daily format, weekly-means of daily values are calculated. Anomalies are defined as data in which the seasonal cycle has been removed from weekly (monthly) data by subtracting the long-term weekly (monthly) mean from each week (month) at each grid point.

The analyses in Chapter 5 are based primarily on the EN3 subsurface temperature data but are supplemented with surface temperature observations from the OI SST

dataset. A more detailed discussion of the methodology used to format the subsurface data will be provided in Chapter 5.

Variability in the extratropical SH SST field is analyzed primarily using statistical tools such as regression/correlation analyses and Empirical Orthogonal Function (EOF) analysis. The remainder of this section describes these techniques in greater detail.

### *2.2.1 Regression and correlation analyses*

Univariate linear regression analysis is used to describe the linear relationship between two variables using the following equation:

$$\hat{y}(t) = a_0 + a_1 x(t) \quad (2.1)$$

where  $x(t)$  is an independent variable and  $\hat{y}(t)$  is the estimate of the observed  $y(t)$ . Linear regression determines the slope of the line that minimizes the error between the estimate  $\hat{y}(t)$  and the observed data  $y(t)$ . The most common method of determining the error is the “least squares” method, which minimizes the sum of the squared error ( $\hat{y} - y$ ) at each time step. Using the least squares method, the regression coefficient  $a_1$  (i.e., the slope) is found as the covariance between  $x$  and  $y$  divided by the variance in  $x$ :

$$a_1 = \frac{\overline{x'y'}}{\overline{x'^2}} \quad (2.2)$$

where the prime denotes the deviation from the mean and the overbar represents the long-term mean. If the independent variable  $x(t)$  is standardized then the regression coefficient will have units of change in  $y(t)$  per one standard deviation change in  $x(t)$ .

The strength of the relationship given by the least-squares regression is quantified by the correlation coefficient and is determined by comparing the variances of the estimated  $\hat{y}(t)$  and the observed  $y(t)$ . In the linear case described above, the correlation coefficient  $r$  can be calculated:

$$r = \frac{\overline{x'y'}}{\sqrt{\overline{x'^2} \overline{y'^2}}} \quad (2.3)$$

The square of  $r$  corresponds to the fraction of the variance explained by the least-squares fit between two variables.

The statistical significance of the correlation coefficients (and associated regression coefficients) calculated in this study are assessed using the  $t$ -statistic, which is defined in this case as:

$$t = \frac{r\sqrt{N_{eff} - 2}}{\sqrt{1 - r^2}} \quad (2.4)$$

where  $r$  is the correlation coefficient and  $N_{eff}$  is the effective sample size that accounts for the persistence in the data. Assuming the data follow a first order auto-regressive process, Bretherton et al. (2001) outlined a method for determining the effective sample size  $N_{eff}$  as:

$$N_{eff} = N \left[ \frac{1 - r_1 r_2}{1 + r_1 r_2} \right] \quad (2.5)$$

where  $N$  is the sample size, and  $r_1$  and  $r_2$  are the lag-one autocorrelations of the time series being correlated. The effective sample size is inversely proportional to the product of the lag-one autocorrelation of the two time series being correlated. If the data exhibit

substantial persistence, then each sample may not be independent from the previous sample and thus the number of independent samples will be smaller than  $N$ .

### 2.2.2 Empirical Orthogonal Function (EOF) analysis

Empirical Orthogonal Function (EOF) analysis is used to isolate the dominant patterns of variability in the extratropical SH SST field. EOF analysis decomposes any data matrix,  $A_{M \times N}$ , into a series of orthogonal spatial patterns and time series such that the variance in the new phase space is organized entirely along the diagonal of the dispersion matrix. The EOFs are calculated by solving the following eigenvalue problem:

$$C_{N \times N} E_{N \times N} = E_{N \times N} L_{N \times N} \quad (2.6)$$

where  $C$  is the covariance matrix corresponding to  $1/M * A^T A$ ,  $E$  is the matrix of eigenvectors  $e_i$  of length  $N$ , and  $L$  is a diagonal  $N \times N$  matrix containing the eigenvalues  $\lambda_i$ . If  $M$  corresponds to the number of time steps and  $N$  corresponds to the number of grid points then  $C$  represents the spatial covariance matrix. In this case, the eigenvector of  $C$  with the largest eigenvalue  $\lambda_i$ , corresponds to the spatial pattern in  $A$  that explains more variance than any other spatial pattern.

The fraction of the total variance explained by each eigenvector is expressed as:

$$fraction\ of\ variance\ explained = \frac{\lambda_i}{\sum_{i=1}^N \lambda_i} \quad (2.7)$$

By definition, the leading eigenvector of  $C$  (often called the leading EOF of  $A$ ) is the eigenvector associated with the largest eigenvalue in  $L$ ; the second EOF is the eigenvector

associated with the second largest eigenvalue in  $L$  (and explains the second largest fraction of variability in  $A$ ); etc. Because the eigenvectors are linearly independent of each other, each EOF is orthogonal to all preceding (and subsequent) EOFs. As a result of this orthogonality constraint, higher order EOFs are increasingly affected by the mathematical constraints of the analysis and are less effective at capturing physical signals in the data.

Projecting the original data matrix  $A$  onto the eigenvectors at all time steps produces the corresponding Principal Component (PC) time series, which describes the temporal evolution of the EOFs. The PC time series can also be found by solving Eq. (2.6), but for the case where  $C$  is the covariance matrix corresponding to  $1/N * AA^T$ . In this case,  $e_i$  represents the  $i^{\text{th}}$  PC time series, etc.

The statistical significance of EOF/PC pairs is assessed by evaluating the robustness (i.e., reproducibility) of each pair. A common method estimates the robustness of EOF/PC pairs by calculating the degree of separation between eigenvalues (North et al. 1982). The 95% confidence error bars  $\Delta\lambda$  for each eigenvalue  $\lambda$  is expressed as:

$$\Delta\lambda = \lambda \sqrt{\frac{2}{N}} \quad (2.8)$$

where  $N$  is the number of independent samples. An EOF is considered to be distinct and statistically significant if the error bars with preceding and subsequent EOFs do not overlap. The robustness of EOF/PC pairs can also be assessed by performing EOF analysis on subsets of the data (e.g., the first and second halves of the record). An

EOF/PC pair that is reproducible (i.e., qualitatively similar) in both subsets of the data as well as the full record can be considered robust.

Several steps were taken before calculating the EOFs in this study. First, the data were arranged in anomaly form so that the first EOF is not dominated by the seasonal cycle. Second, the grid boxes were weighted by the square root of the cosine of the latitude to account for the unequal areas of the grid boxes (i.e., the area of the grid boxes becomes smaller towards the pole). The data are weighted by the square root of the cosine (rather than the cosine) of the latitude because EOF analysis eigenanalyzes the covariance matrix  $A^T A$ . In all cases, the EOFs are shown as regressions onto standardized values of the associated PC time series. The resulting regression maps are very similar but not identical to the EOFs, since the latter lie in cosine weighted space.

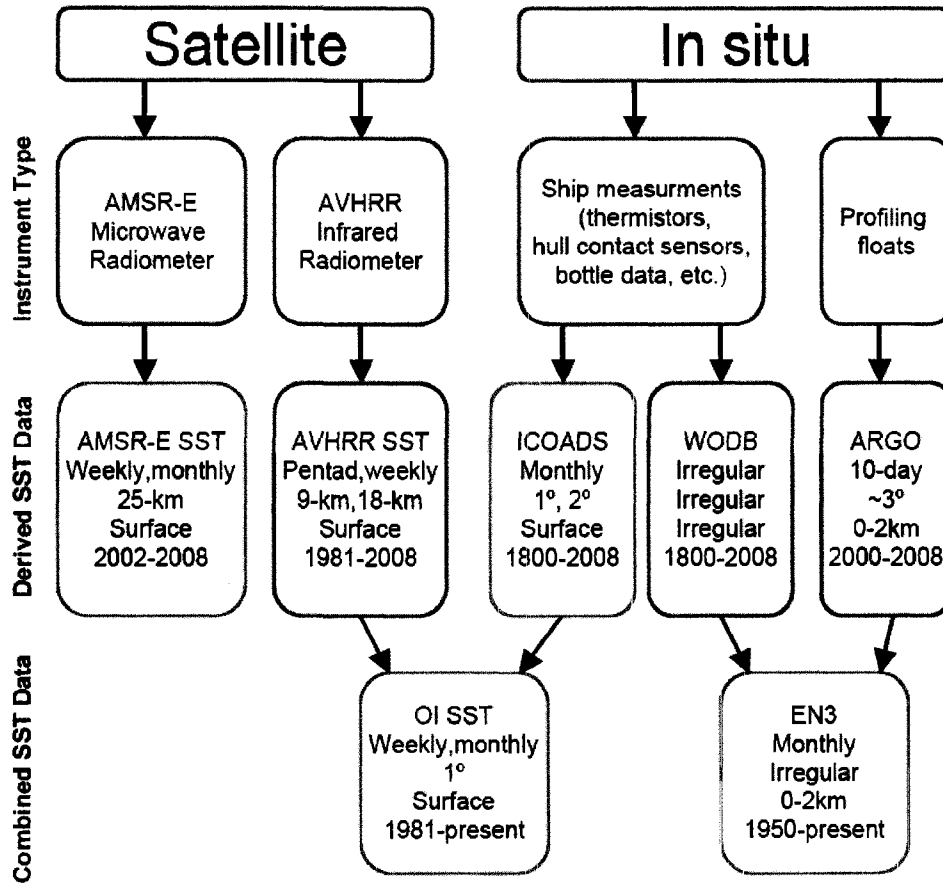


Figure 2.1. Summary of the sea surface and subsurface temperature data described in Chapter 2. For the derived and combined data boxes, the top line corresponds to the dataset name, the second line is the temporal resolution, the third line is the horizontal spatial resolution, the fourth line is the vertical resolution and the bottom line is the period of record. Red boxes denote temperature data specifically analyzed in Chapters 3-5.

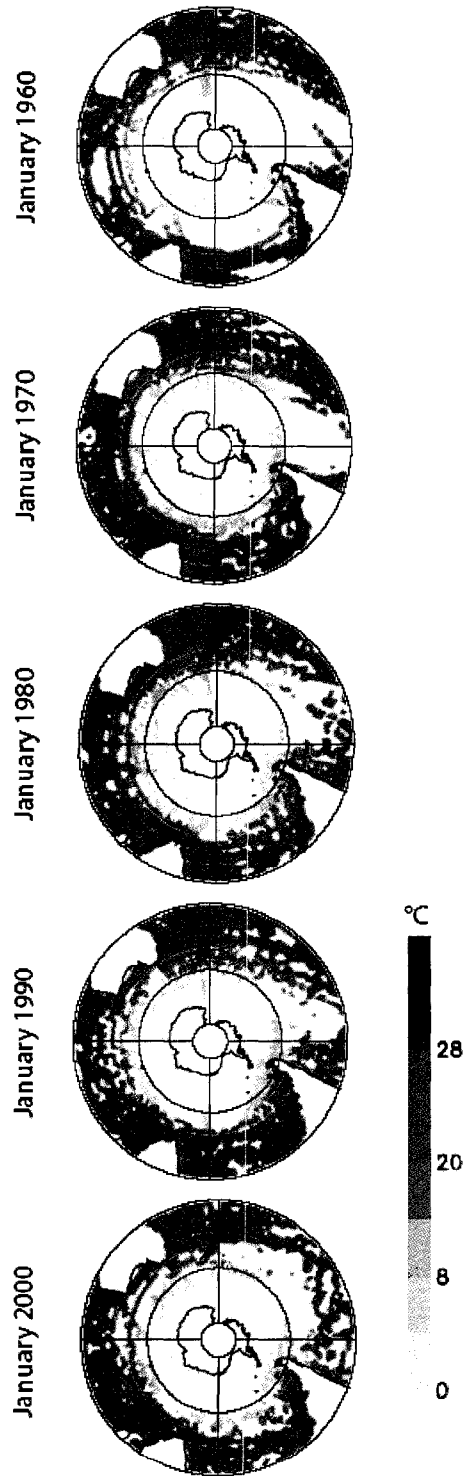


Figure 2.2. Monthly-mean 2° ICOADS SSTs for January of (top) 1960, (second from top) 1970, (middle) 1980, (second from bottom) 1990, and (bottom) 2000.

## **CHAPTER THREE**

### **RELATIONSHIPS BETWEEN PATTERNS OF LARGE-SCALE ATMOSPHERIC VARIABILITY AND EXTRATROPICAL SOUTHERN HEMISPHERE SEA SURFACE TEMPERATURE ANOMALIES**

#### **3.1 Overview**

In this chapter, we examine the relationships between large-scale patterns of atmospheric variability such as the Southern Annular Mode (SAM) and the El Niño Southern Oscillation (ENSO) and extratropical Southern Hemisphere (SH) sea surface temperature (SST) anomalies. Explicitly we will 1) explore seasonal variations in the patterns of SSTs associated with the SAM and ENSO; 2) explicitly compare and contrast the SST patterns associated with the SAM and ENSO; and 3) provide a detailed analysis of the physical processes (i.e., the surface turbulent heat fluxes and heat advection by Ekman currents) that drive observed SST anomalies throughout the SH middle and high latitudes.

#### **3.2 Relevant Aspects of the Climatology**

Before investigating the relationships between large-scale patterns of SH climate variability and the extratropical SST field, it is worth reviewing key climatological features of the SH ocean basins. The contours in the left and right panels of Figure 3.1 show climatological seasonal mean SSTs for the austral warm (November-April) and cold (May-October) seasons, respectively. During both times of year, the isotherms are nearly zonally symmetric, with SSTs decreasing monotonically towards the south pole.

Over most of the SH, the meridional gradients in SSTs are on the order of 4-5 K per  $10^\circ$  of latitude and exhibit a weak seasonal cycle. The meridional gradients in SST are enhanced in the region of the Agulhas Current, where they are as large as 8-10K per  $10^\circ$  of latitude.

The shading in Fig. 3.1 shows the standard deviation of monthly-mean SST anomalies. The two most obvious features in the rms variance field are: 1) the  $\sim 0.5$  K increase in rms variance throughout most of the SH oceans during the warm season; and 2) the region of enhanced variance off the tip of South Africa in the vicinity of the Agulhas current. This region of increased variance associated with the Agulhas Current is analogous to regions of increased variance found in the vicinity of the Gulf Stream and Kuroshio currents in the Northern Hemisphere (NH).

Figure 3.2 shows the climatological mean depth of the mixed layer for the warm and cold seasons (shading) superposed on the mean bounds of the location of the Antarctic Circumpolar Current (ACC; contours). The mean bounds of the position of the ACC are derived from Karsten and Marshall (2002), and correspond to the northernmost and southernmost lines of constant sea surface height (SSH) that encircle the globe uninterrupted by land (the SSH data are derived from TOPEX/Poseidon altimetry data described in Chapter 2).

During the warm season, the mixed layer is on average less than 50 m deep equatorward of  $45^\circ\text{S}$  and between 50 and 100 m deep poleward of  $45^\circ\text{S}$ . The relatively shallow mixed layer depths during the summer are consistent with weaker convective and mechanical mixing during that season. For the most part, the mixed layer is considerably deeper during the cold season as vertical mixing in the upper layers of the ocean is

enhanced. The increase in mixed layer depths during the cold season is most pronounced poleward of 45°S with the most extensive increases in mixed layer depths found just equatorward of the ACC where Subantarctic Mode Waters and Antarctic Intermediate Waters are formed. The mixed layer also deepens substantially during winter in the Weddell Sea, consistent with enhanced deep-water formation in that region. Note that for the most part, the winter season is associated with deeper mixed layers (Fig. 3.2), but lower standard deviations in the SST field (Fig. 3.1).

### **3.3 Patterns of SH SST Anomalies Associated with the SAM and ENSO**

In this section, we investigate the structures of SST variability associated with the two most important patterns of SH climate variability: the SAM and the remote SH response to ENSO.

Maps formed by regressing monthly-mean SST and 500 hPa height ( $Z_{500}$ ) anomalies onto standardized values of the SAM and ENSO indices are shown in the top and middle rows of Figure 3.3, respectively. Contours (shading) correspond to  $Z_{500}$  (SST) anomalies. The left (right) panel corresponds to the warm (cold) season. Recall from Chapter 2 that positive values of the ENSO index denote cold conditions in the eastern tropical Pacific, and vice versa. Thus, the anomalies in the regression maps correspond to the high index polarity of the SAM and the cold phase of the ENSO cycle.

As reviewed in Chapter 1, the high index polarity of the SAM is characterized by lower-than-normal heights over the polar regions and higher-than-normal heights ~40°S (contours, top panels). The structure of the SAM in  $Z_{500}$  is nearly identical throughout the year, but has a more pronounced trough to the west of the Antarctic Peninsula during the

cold season. As also reviewed in Chapter 1, the structure of ENSO in  $Z_{500}$  has a stronger wave-like component than the SAM (contours, middle panels): during austral winter, the cold phase of the ENSO cycle is associated with positive height anomalies to the east of New Zealand, negative height anomalies to the west of the Antarctic Peninsula, and positive height anomalies in the Atlantic sector of the Southern Ocean. As noted in L'Heureux and Thompson (2006), during austral summer the SH response to ENSO also exhibits negative geopotential height anomalies that extend across the pole, positive anomalies that extend from the South Atlantic to the Indian Ocean, and thus the signature of ENSO in  $Z_{500}$  field bears resemblance to the nearly zonally symmetric structure of the SAM (i.e., compare the contours in the top left and middle left panels). The correlation between monthly-mean indices of the SAM and ENSO is  $r \sim 0.5$  during the months November-April (L'Heureux and Thompson 2006).

During the SH warm season, the similarities between the structure of the SAM and ENSO in the SH geopotential height field extend to the sea surface temperature field (top and middle left panels of Fig. 3.3). For example, both the SAM and ENSO are associated with a broad region of negative SST anomalies in the South Pacific sector around  $90^{\circ}$ - $150^{\circ}$ W,  $40^{\circ}$ - $60^{\circ}$ S, positive SST anomalies centered around New Zealand and stretching from Australia to South America along  $30^{\circ}$ - $40^{\circ}$ S, positive SST anomalies along  $45^{\circ}$ S in the southern Atlantic Ocean, and negative SST anomalies along  $20^{\circ}$ - $30^{\circ}$ S in the eastern Pacific, Atlantic and Indian ocean basins. The spatial correlation between the SST regressions maps in the top left and middle left panels is  $\sim 0.75$ .

The most notable differences between the warm season ENSO and SAM SST regression maps lie in their amplitudes: the SAM-related SST anomalies are about half

the amplitude of the ENSO-related SST anomalies (note the color scales for the ENSO and SAM regression maps are different). The differences in amplitudes between the ENSO and SAM SST regression maps are consistent with the relative time scales of SH SSTs and the SAM and ENSO indices used in the regressions, i.e., most of the variance in the SAM index is found on month-to-month timescales, whereas much of the variance in both the ENSO index and Southern Ocean SSTs is found on interannual timescales. The amplitudes of the SAM and ENSO warm season regression maps are very similar when the SAM regression map is based on standardized seasonal-mean values of the SAM index (not shown).

During the SH cold season, fluctuations in ENSO are not significantly correlated with temporal variability in the SAM (L'Heureux and Thompson 2006). Thus the cold season SST regression maps (top and middle right panels of Fig. 3.3) may be viewed as more distinct expressions of the SAM and ENSO in the SH SST field. The cold season SAM regression map (top right) is similar to its warm season counterpart (top left) at middle and high latitudes but does not exhibit pronounced anomalies extending into the subtropical sector of the South Pacific. The cold season ENSO regression map (middle right) resembles its warm season counterpart (middle left) but does not exhibit substantial anomalies in the southern Atlantic and Indian Oceans. For the most part, SST anomalies associated with both the SAM and ENSO exhibit weaker amplitudes during the cold season than during the warm season. The cold season SAM regression map in the top right panel is nearly identical to the pattern of SSTs associated with the SAM found for year-round data, as presented in Lovenduski and Gruber (2005) and Sen Gupta and England (2006).

How do the patterns of SST anomalies associated with the SAM and ENSO relate to the dominant structures of hemispheric scale SH SST variability? The bottom panels in Fig. 3.3 show the regressions of monthly-mean SST (shading) and  $Z_{500}$  (contours) anomalies onto the standardized leading principal component (PC) time series of the SST field calculated for the domain  $20^{\circ}$ - $80^{\circ}$ S. The patterns of SST variability associated with leading PC time series of the cold (right panel) and warm (left panel) seasons account for 15% and 13% of the total variance, respectively. The patterns of SST anomalies associated with the second PC (not shown) explain approximately 8% of the total variance in each season, and the leading EOF/PCs are well separated according to the criteria outlined in North et al. (1982).

As evidenced in Fig. 3.3 and quantified in Table 3.1, during both seasons, the leading patterns of SH SST variability project most strongly onto the pattern of SST anomalies associated with ENSO. Similarly, the patterns of  $Z_{500}$  anomalies associated with the leading PCs of SH SST variability (contours, bottom panels) bear strong resemblance to the structure of ENSO in the SH geopotential height field (contours, middle panels). The expansion coefficient time series of the ENSO-related SST regression maps in the middle panels are correlated with the leading PC time series of the SH SST field at a level of  $r=0.93$  during the cold season and  $r=0.99$  during the warm season (Table 3.1). Note that during the warm season, the pattern of SST anomalies associated with the leading PC time series of SH SST anomalies also resembles the pattern of SST anomalies associated with the SAM by virtue of the correlation between the SAM and ENSO.

The patterns of SST anomalies associated with the SAM and ENSO in Fig. 3.3 are based on SST anomalies obtained from the OI SST data, a blended analysis of AVHRR satellite and in situ observations (Reynolds et al. 2002). In Figures 3.4-3.7 we examine the same results using the raw in-situ data from ICOADS and microwave measurements from the AMSR-E SST data. Note the ICOADS data are used in the OI scheme, and that the AMSR-E data are only available 2002-2008 but are not impacted by regions of cloudiness and have denser spatial coverage (Chapter 2).

Figure 3.4 shows the regressions of monthly-mean SST anomalies onto the SAM for data derived from OI SST (top panels; a reproduction of the SST anomalies from the top row of Fig. 3.3) and from the ICOADS SST data (bottom row). Figure 3.5 is created in a similar fashion but the regressions are based on the inverted ENSO index. The results derived from the ICOADS data are noisy compared to those derived from the OI SST data due to the sparse nature of in situ data over the Southern Ocean (see Figure 2.2). The principle features evident in the OI SST patterns are also observed over regions where in situ data are available. The results demonstrate that the SST anomalies associated with the SAM and ENSO in Fig. 3.3 are reproducible in raw in situ data that are not impacted by clouds and satellite biases. Overall, the amplitudes of the regression maps are similar in both the OI SST and ICOADS data, but there are several highly-localized areas in which the amplitudes are slightly stronger in the ICOADS data.

Figures 3.6 and 3.7 are similar to Figs. 3.4 and 3.5 but the bottom panels now correspond to regressions based on AMSR-E SST data, which are completely independent from the OI SST data. All regression maps in Figs. 3.6 and 3.7 are based only on data from 2002-present, the full AMSR-E record. The structure of the regression

maps derived from OI SST data are remarkably similar to the regression maps derived from AMSR-E SST data with two noticeable differences: 1) the ASMR-E regressions exhibit fine-scale noisy features in the Agulhas Return Current east of Africa and the Brazil Current east of South America that the relatively coarse OI SST data cannot capture; and 2) For the most part, the amplitudes of the regression maps tend to be slightly stronger ( $0.05^{\circ}$ - $0.1^{\circ}\text{C}$ ) in the AMSR-E SST data.

### **3.4 Physical Processes That Drive SH SST Variability on Monthly Timescales**

Below we examine the physical processes through which the SAM and ENSO give rise to the patterns of extratropical SH SST anomalies revealed in the previous section.

On the basis of previous research discussed in Chapter 1, we expect that the SAM and ENSO will impact extratropical SSTs predominantly through changes in surface turbulent fluxes of latent and sensible heat as well as heat advection from Ekman currents (e.g., Frankignoul and Hasselman 1977; Frankignoul 1985; Verdy et al. 2006; Sen Gupta and England 2006). Here we analyze the seasonally varying relationships between the SAM and ENSO and the surface turbulent and Ekman heat fluxes, and compare the results with the patterns of SST anomalies shown in the previous section (3.3). The results are consistent with observational findings reported in Verdy et al. (2006), but the present study more explicitly compares the flux estimates with the pattern of SST anomalies associated with the SAM and ENSO, focuses on regions outside the ACC, and highlights seasonally varying aspects of the relationships.

The top panels in Figure 3.8 are a reproduction of the SST and  $Z_{500}$  anomalies from the top panels in Fig. 3.3. The middle and bottom two panels in Fig. 3.8 show the monthly-mean total surface turbulent heat fluxes (defined as the sum of the latent and sensible heat fluxes) and heat advection by the anomalous Ekman currents (hereafter referred to as the Ekman heat fluxes) regressed onto standardized values of the SAM index, respectively, for the SH warm (left) and cold (right) seasons. The contours in the middle and bottom panels are a reproduction of the  $Z_{500}$  height anomalies from the top panels. Positive values denote fluxes of heat into the ocean, and vice versa. A more detailed description of the surface turbulent and Ekman heat fluxes is provided in Chapter 2.

During both the warm and cold seasons, the high index polarity of the SAM is associated with positive surface turbulent heat fluxes (from the atmosphere to the ocean) throughout much of the zonal ring spanning  $40^{\circ}$ - $50^{\circ}$ S, with maximum positive flux anomalies centered around New Zealand and across a broad region extending eastward from the southern tip of South America to the Indian Ocean. The largest negative anomalies in the turbulent fluxes of heat (i.e., fluxes from the ocean to the atmosphere) are found during the cold season along  $60^{\circ}$ S, with substantial negative anomalies evident in the Pacific sector of the Southern Ocean between  $100^{\circ}$ - $140^{\circ}$ W and  $40^{\circ}$ - $60^{\circ}$ S.

The patterns of turbulent heat flux anomalies associated with the SAM index are consistent with the associated changes in the overlying flow. Bearing in mind that the large-scale atmospheric flow in the SH is close to geostrophic balance and thus that the overlying  $Z_{500}$  anomalies approximate the direction of the anomalous atmospheric winds, the regions of negative air-to-sea fluxes off the coast of east Antarctica and to the east of

the Antarctic Peninsula are consistent with enhanced surface wind speeds in the latitude band  $\sim 50^{\circ}$ - $60^{\circ}$ S; the widespread positive air-to-sea fluxes of heat in SH middle latitudes are consistent with decreased surface wind speeds between  $30^{\circ}$ - $40^{\circ}$ S; the band of locally enhanced negative air-to-sea fluxes centered near  $120^{\circ}$ W in the Southern Ocean are coincident with anomalous southerly advection there; and the enhanced positive fluxes in the vicinity of the Drake Passage are consistent with anomalous northerly advection there.

The shading in the bottom panels of Fig. 3.8 shows the corresponding regressions for heat advection due to the anomalous Ekman currents. Consistent with findings reported by Verdy et al. (2006) for year-round data, negative Ekman heat flux anomalies are observed in much of the circumpolar region around  $50^{\circ}$ - $60^{\circ}$ S, but positive Ekman heat flux anomalies are also evident further north around  $30^{\circ}$ - $40^{\circ}$ S. The Ekman heat flux patterns are consistent with the anomalous Ekman currents inferred from the pattern of wind anomalies associated with the SAM, i.e., the anomalous wind stress on the surface layers of the ocean drives anomalous northward Ekman transport along  $\sim 60^{\circ}$ S but anomalous southward Ekman transport at  $40^{\circ}$ S.

The patterns of turbulent and Ekman heat flux anomalies associated with the SAM are similar in both SH cold and warm seasons but for one notable difference: the amplitude of the turbulent heat flux anomalies (middle panels) are uniformly stronger during the SH cold season than they are during the warm season, whereas the amplitude of the Ekman heat fluxes (bottom panels) are comparable during both seasons. The weaker seasonal cycle in the Ekman heat fluxes is consistent with the weak seasonal cycles in the amplitude of the SAM and the meridional gradients in SSTs.

Comparing the flux regressions from the lower four panels in Fig. 3.8 with the top panels, it is evident that both the anomalous turbulent and Ekman heat fluxes play a substantial role in generating the extratropical SST anomalies associated with the SAM. Both the turbulent heat flux and SST maps exhibit positive anomalies at  $40^{\circ}$ - $50^{\circ}$ S throughout the south Atlantic, Indian, and western Pacific oceans and negative anomalies in the central Pacific around  $40^{\circ}$ - $60^{\circ}$ S,  $90^{\circ}$ - $140^{\circ}$ W. The Ekman heat flux anomalies contribute most to the observed SST anomalies in the high latitude Southern Ocean, as emphasized in Verdy et al. (2006), but also reinforce the positive turbulent heat flux anomalies along  $40^{\circ}$ S.

It is interesting that the amplitudes of the SST anomalies associated with the SAM are weakest during the cold season (top panels), but that the amplitudes of the attendant turbulent heat flux anomalies are largest during the cold season (middle panels). At first, these results seem counter-intuitive since the SST anomalies associated with the SAM are presumably driven by, and hence are proportional to, the amplitude of the sensible and latent heat fluxes. However, as reviewed in Frankignoul (1985), the thermal inertia of the mixed layer is directly proportional to its depth, and thus the response of the SST field to anomalous turbulent heat fluxes is directly proportional to the amplitude of the fluxes but inversely proportional to the depth of the mixed layer. Hence, the presence of weaker SST anomalies during the cold season despite a  $\sim 50\%$  increase in the heat fluxes is consistent with the roughly four fold increases in SH wintertime mixed layer depths, as shown in Fig. 3.2.

Figure 3.9 is analogous to Fig. 3.8, but shows regressions based on the inverted ENSO index (note that the color scales have changed from Fig. 3.8). The main features in

the Ekman heat flux regressions (bottom panels) are evident in the SST anomalies (top panels), e.g., the negative Ekman heat flux anomalies in the Pacific sector of the SH are consistent with the negative SST anomalies in that region; and the positive Ekman heat flux anomalies during the warm season south of Australia (40°S, 120°-180°E) and South Africa (40°S, 15°W-45°E) are also mirrored in the SST field. However, the resemblance between the ENSO turbulent heat flux and SST regression maps is less clear. During the cold season, the main features in the turbulent flux regression map are mirrored in the SST regression map, particularly over the Pacific sector of the hemisphere. But during the warm season, the turbulent heat flux regression map exhibits features that are not evident in the SST field. In general, the similarities between the patterns of surface turbulent heat flux and SST anomalies are weaker for ENSO than they are for the SAM.

It is not clear why the patterns of anomalous surface turbulent heat and Ekman fluxes associated with ENSO do not project strongly onto the patterns of ENSO-related SST anomalies. We repeated the analyses in Fig. 3.9 for seasonal mean data to minimize the impact on the regressions of intraseasonal variability not related to ENSO (Figure 3.10; top panel), for seasonal mean data lagged by up to three months to account for the fact that the atmospheric response to ENSO may lag tropical SST anomalies by several months (Figure 3.10), and for turbulent flux data from three different though not entirely independent flux data sources (Figure 3.11): the NCEP-Reanalysis 2 data, which is an updated version of the NCEP reanalysis data used here; the Woods Hole Oceanographic Institute Objectively Analyzed Air-Sea Flux Data (OAFflux); and the European Centre for Medium-Range Weather Forecast Reanalysis-40 (ERA-40) flux data. In all cases, the resulting flux regressions are qualitatively similar to the results in Fig.3.9, which suggests

the discrepancies between the middle and top panels of Fig. 3.9 transcend the specifics of the analysis procedure.

It is possible that, unlike SAM-related SST anomalies, ENSO-related SST anomalies are not primarily driven by surface turbulent heat fluxes. A comparison of the surface turbulent and Ekman heat fluxes associated with SAM (i.e., compare the middle and bottom panels with the top panel of Fig. 3.8) demonstrates that surface turbulent heat fluxes project most strongly onto the SAM-SST pattern and are reinforced by Ekman heat fluxes of the same sign. However, a comparison of the surface turbulent and Ekman heat fluxes associated with ENSO (i.e., compare the middle and bottom panels with the top panel of Fig. 3.9) demonstrates the Ekman heat fluxes partially balance the surface turbulent heat fluxes in several regions. The negative turbulent heat fluxes observed south of Africa are offset by the positive Ekman heat fluxes in the region, thus creating a small net flux into the ocean (Fig. 3.12). The negative Ekman heat fluxes observed east of New Zealand along 20°-30°S slightly balance the positive turbulent heat fluxes, thus reducing the net flux into the ocean. Consequently, the pattern of ENSO-related SST anomalies (Fig. 3.9 top panel) is more consistent with the combined pattern of surface turbulent and Ekman heat flux anomalies (Fig. 3.12) than the pattern of surface turbulent heat flux anomalies alone (Fig. 3.9 middle panel).

Another process that may influence subtropical SSTs is variability in shortwave radiation associated with ENSO. Changes in tropical convection/cloud cover will induce changes in the fraction of shortwave radiation that is absorbed at the surface (Klein et al. 1999; Lau and Nath 2001; Park et al. 2005). Fig. 3.13 shows the anomalous shortwave radiation associated with ENSO. During warm season, La Niña conditions are

characterized by anomalous convection in the western Pacific sector. The resulting increase in cloud cover decreases the shortwave radiation absorbed at the surface and anomalous cooling is observed in the western tropical/subtropical South Pacific Ocean. In the central/eastern part of the basin, the reduced convection gives rise to decreased cloud cover, which in turn, gives rise to increased shortwave radiation and positive SST anomalies in the region.

Figure 3.14 shows the combined radiative, surface turbulent and Ekman heat fluxes associated with ENSO. The structure of ENSO-related SST anomalies exhibits slightly more agreement with the structure of heat flux anomalies when shortwave radiation is taken into consideration (i.e., compare the top panel of Fig. 3.9 with Fig. 3.12 and Fig. 3.14). However, there are still discrepancies between the pattern of SSTs and combined heat flux anomalies, particularly in the Indian and Atlantic Oceans. In the warm season, the SST regression map exhibits features south of Africa that are not evident in the heat flux field. In the cold season, turbulent heat flux regression map exhibits features across the Indian and Atlantic Oceans that are not evident in the SST field.

### **3.5 Concluding Remarks**

The analyses presented in this chapter support the studies reviewed in Chapter 1, but also extend those studies by: 1) documenting and interpreting seasonal variations in the impact of the SAM and ENSO on the SH extratropical sea surface temperature field and 2) examining the mechanisms through which ENSO and the SAM drive SST variability not only in the vicinity of the ACC but throughout the SH.

The key results of this chapter are the following:

*1) The patterns of SST anomalies associated with the SAM and ENSO vary as a function of season in terms of both their structures and their amplitudes.*

During the cold season, the high index polarity of the SAM is associated with predominantly negative SST anomalies poleward of 50°S and positive SST anomalies equatorward of 50°S, except for a large region of cold anomalies that extends from the west of the Antarctic Peninsula to middle latitudes. The cold phase of the ENSO cycle shares with the SAM the large band of negative SST anomalies to the west of the Antarctic Peninsula, but also exhibits pronounced positive SST anomalies across the southern Pacific Ocean along ~30°S.

During the warm season, the expressions of ENSO and the SAM in the SH SST field bear strong resemblance to each other, consistent with the linear relationship between the SAM and ENSO at that time. Thus, the warm season SAM pattern in SSTs is similar to its cold season counterpart, but includes SST anomalies that extend equatorward toward the tropical Pacific Ocean, and the warm season ENSO pattern in SSTs resembles its cold season counterpart, but includes SST anomalies that extend into the Atlantic and Indian Ocean sectors.

The amplitudes of the impacts of the SAM and ENSO on the SH SST field are largest during the warm season, consistent with the relatively shallow mixed layer at this time.

*2) The leading EOF of monthly-mean SST anomalies projects strongly onto the pattern of SST anomalies associated with the remote SH response to ENSO in both the warm and cold seasons.*

During the warm season, the pattern of SST anomalies associated with the leading PC time series of SH SST anomalies also projects onto the pattern of SST anomalies associated with the SAM by virtue of the correlation between the SAM and ENSO. The warm season EOF in the bottom left panel is nearly identical to the EOFs found for year-round data, as presented in Kidson and Renwick (2002).

*3) The anomalous turbulent heat fluxes associated with the SAM play a key role in generating the observed SST anomalies throughout the SH, while the associated anomalous Ekman heat fluxes are important primarily over high latitudes.*

A comparison of the structures of the SST, surface turbulent and Ekman heat flux anomalies associated with the SAM suggests the turbulent fluxes play an important role in driving the SAM-related SST anomalies throughout much of the SH. The results also suggest that anomalous heat advection by Ekman currents plays a key role in the vicinity of the Antarctic Circumpolar Current (ACC), consistent with Verdy et al. (2006), but are of secondary importance elsewhere (e.g., compare Fig. 3.8, middle and bottom panels). The turbulent heat fluxes exhibit largest amplitude during the cold season, while the Ekman heat fluxes exhibit comparable amplitude year-round.

The ENSO-related SH SST anomalies project strongly onto the ENSO-related Ekman heat flux anomalies. However, the relationships between the ENSO-related SST and turbulent heat flux anomalies over the SH are less clear, particularly during the warm season. Shortwave radiation associated with ENSO appears to be associated with SST variability primarily in the subtropical Pacific sector.

### Climatological Mean and Standard Deviation of Monthly SSTs

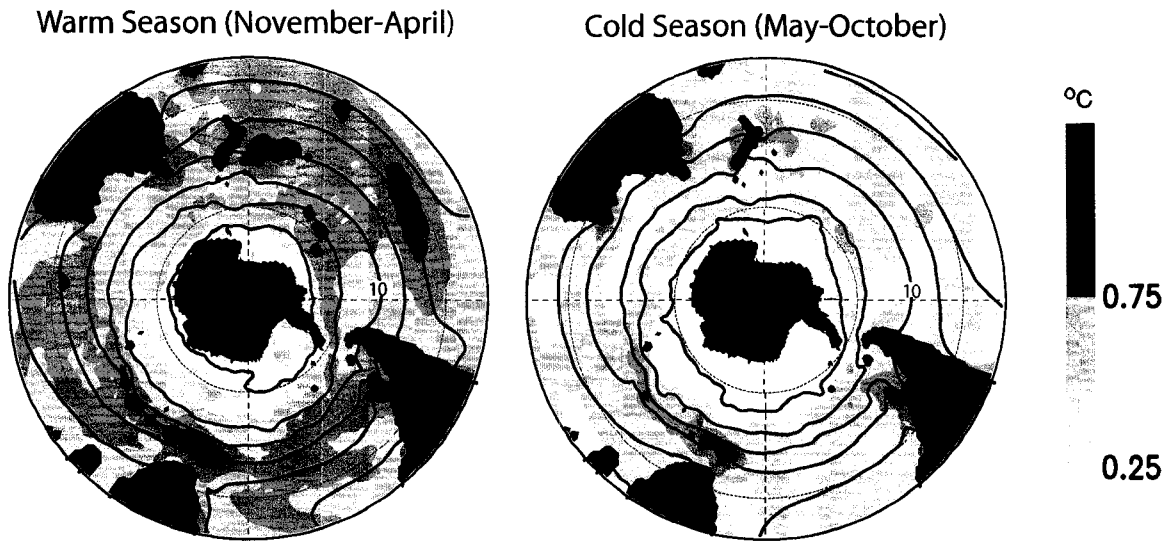


Figure 3.1. Climatological mean sea surface temperatures (SSTs; contours) and standard deviation of SST anomalies (shading) for the (left) warm and (right) cold seasons. Contour intervals are drawn at (0°C, 5°C, 10°C...). The 10°C contour is labeled.

## Climatological Mean Mixed Layer Depths

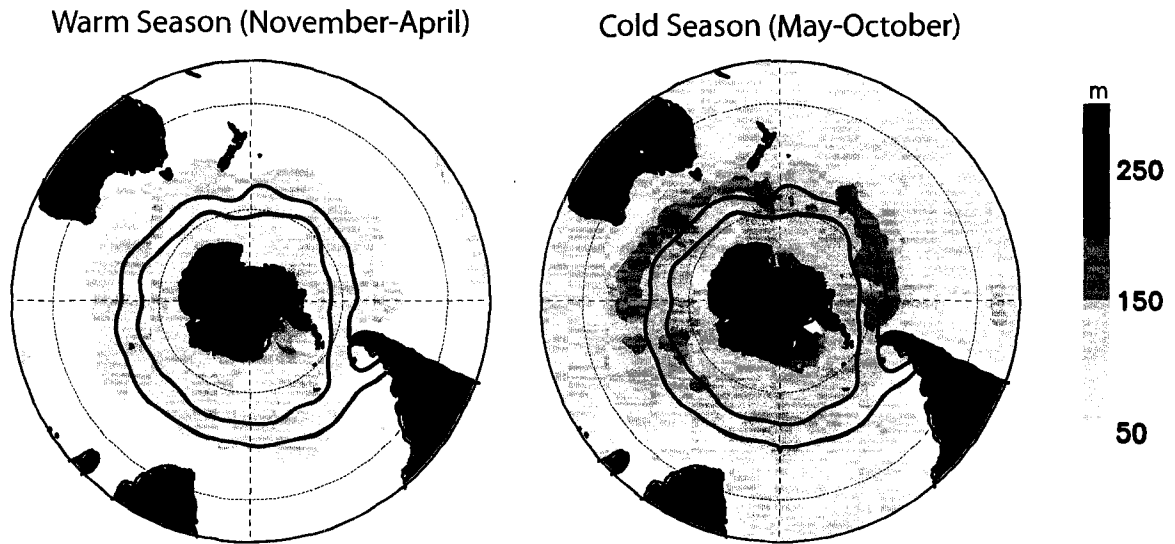


Figure 3.2. Climatological mean mixed layer depths (shading) for the (left) warm and (right) cold seasons. Contours represent the mean path of Antarctic Circumpolar Current (ACC; see text for details of ACC).

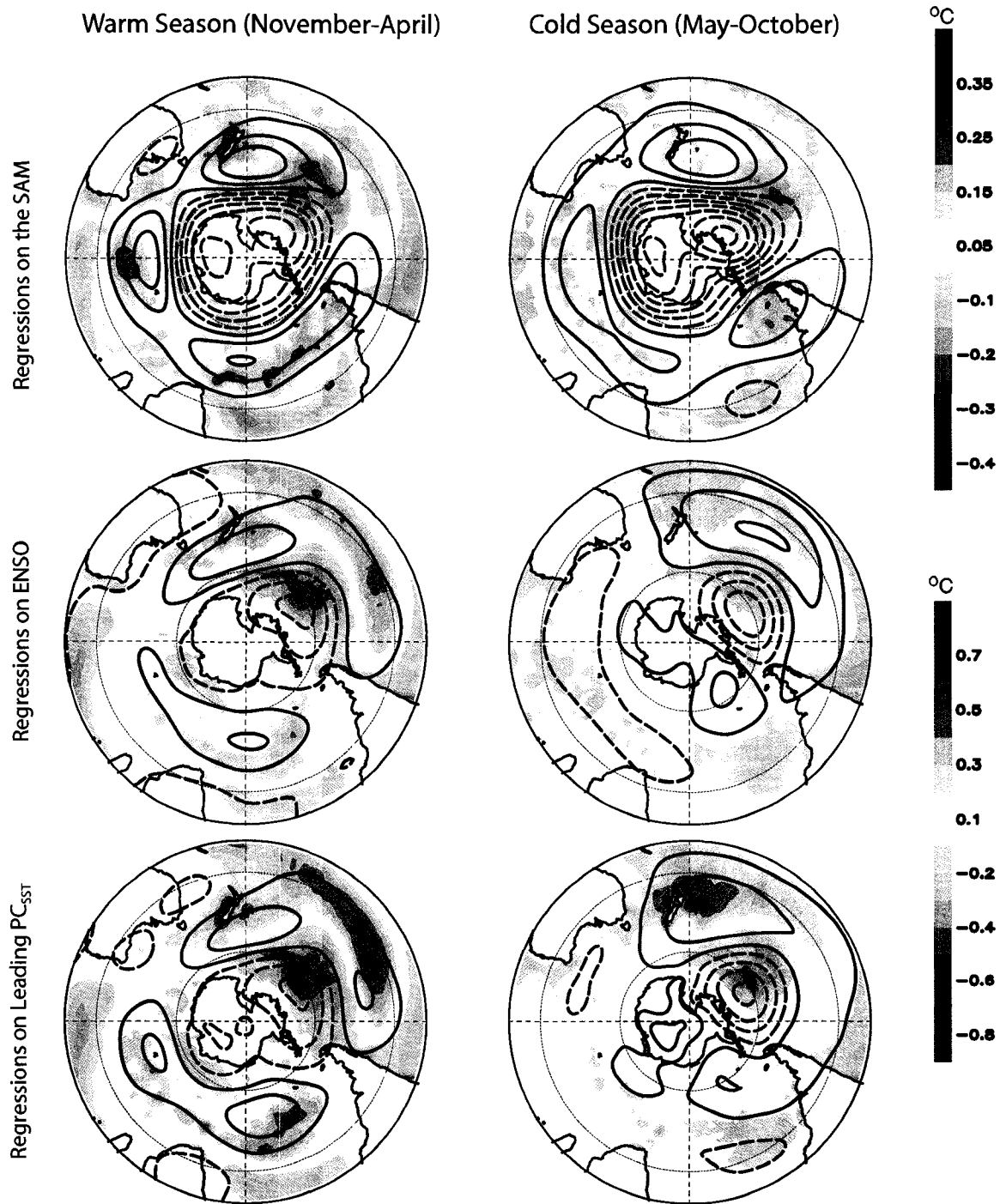


Figure 3.3. Monthly-mean SST (shaded) and  $Z_{500}$  (contours) anomalies regressed onto the (top row) SAM index, (middle row) ENSO index and (bottom row) leading principal component time series of monthly-mean SST anomalies. Positive (negative) contours are denoted by solid (dashed) lines and are drawn at (-5m, 5m, 15m...). The left column denotes warm season (November-April) results and the right column denotes cold season (May-October) results. Note that the sign of the results corresponds to the high index polarity of the SAM and the cold phase of the ENSO cycle.

### Regressions of SST Anomalies on SAM

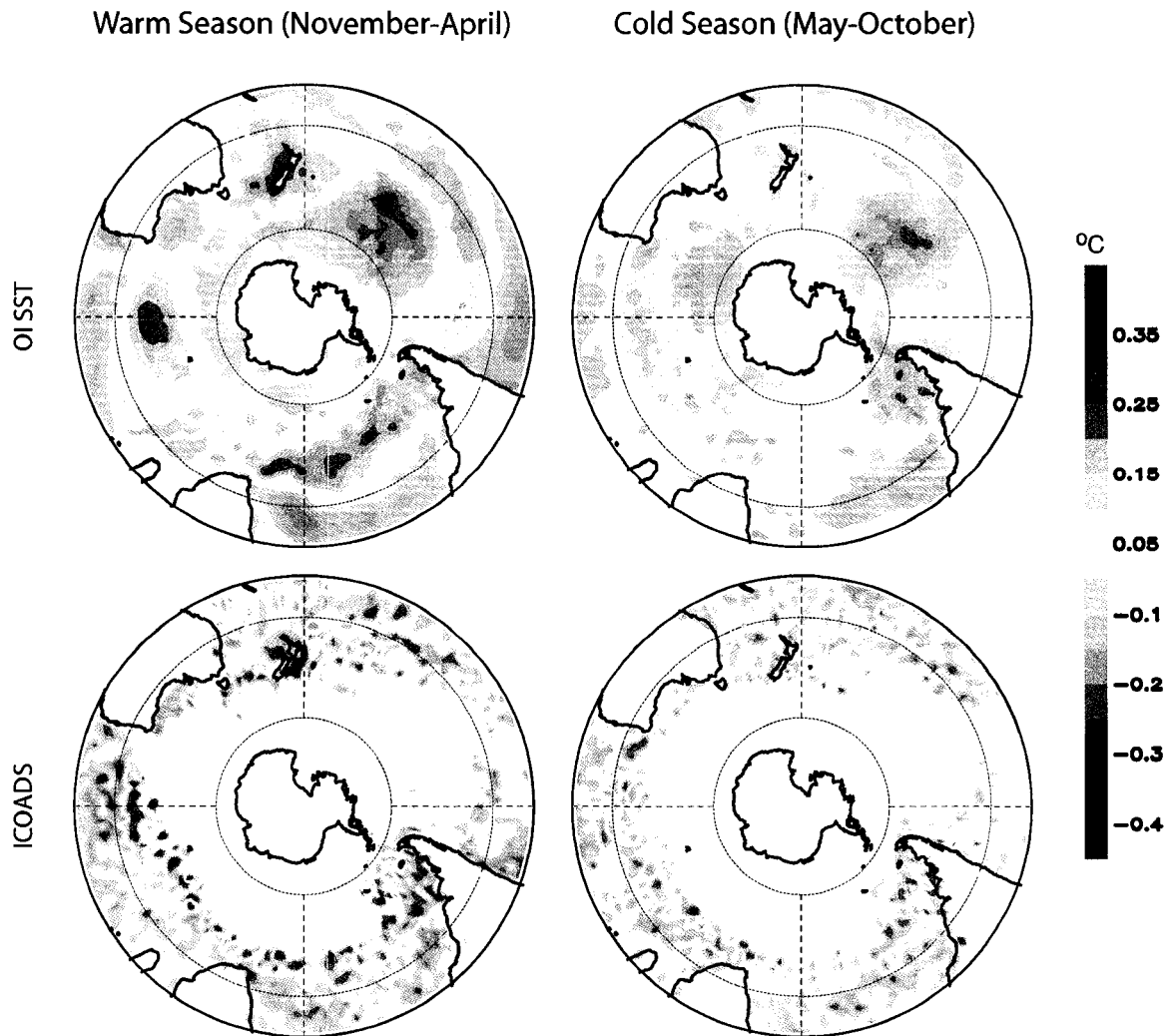


Figure 3.4. Monthly-mean SST anomalies regressed onto the standardized SAM index for (top row) OI SST data and (bottom row) ICOADS SST data. The left column denotes warm season (November-April) results and the right column denotes cold season (May-October) results.

## Regressions of SST Anomalies onto ENSO

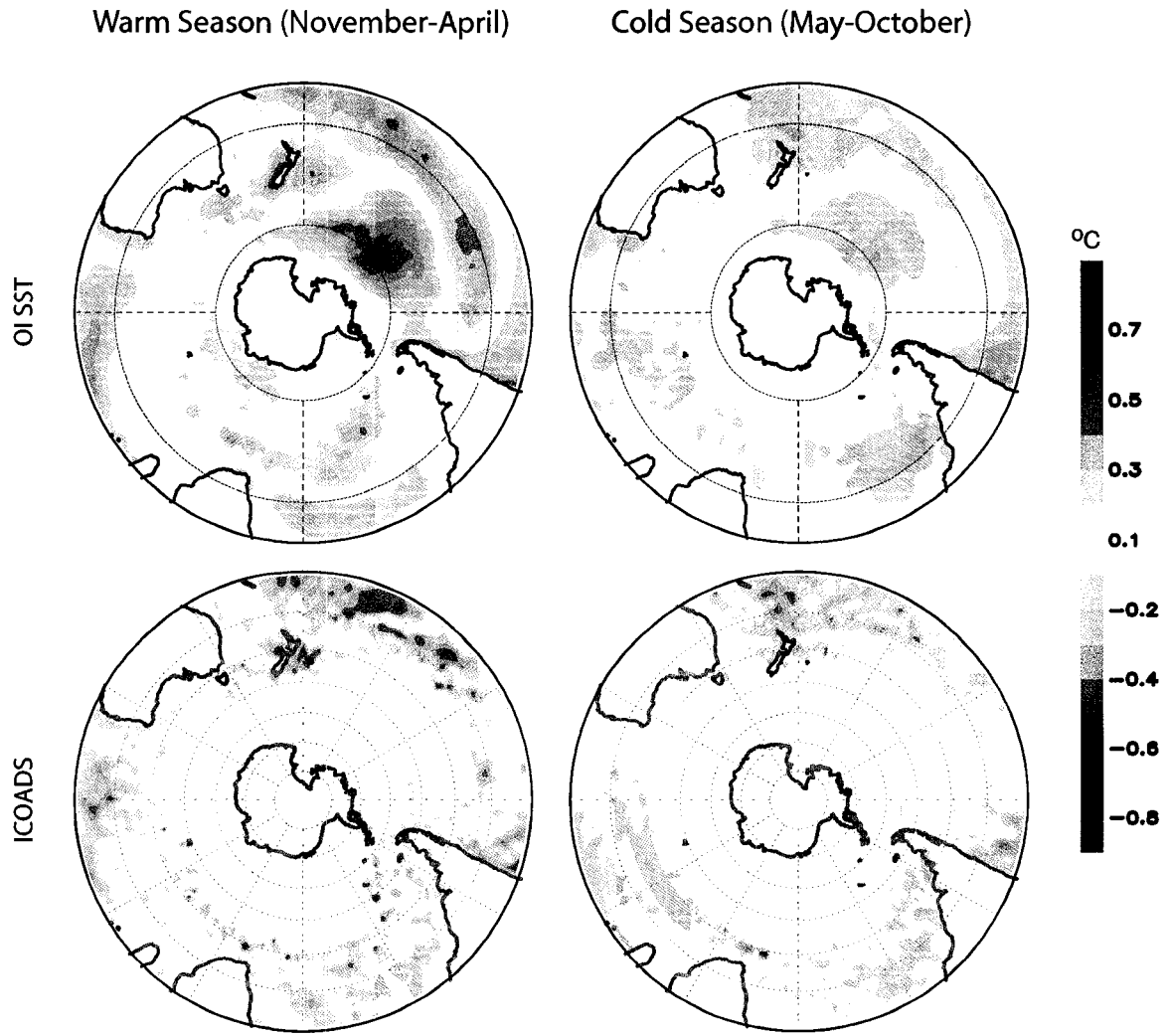


Figure 3.5. As in Figure 3.4 but regressions are based on the standardized ENSO index. Positive values of the ENSO index denote cold conditions in the eastern tropical Pacific.

### Regressions of SST Anomalies on SAM

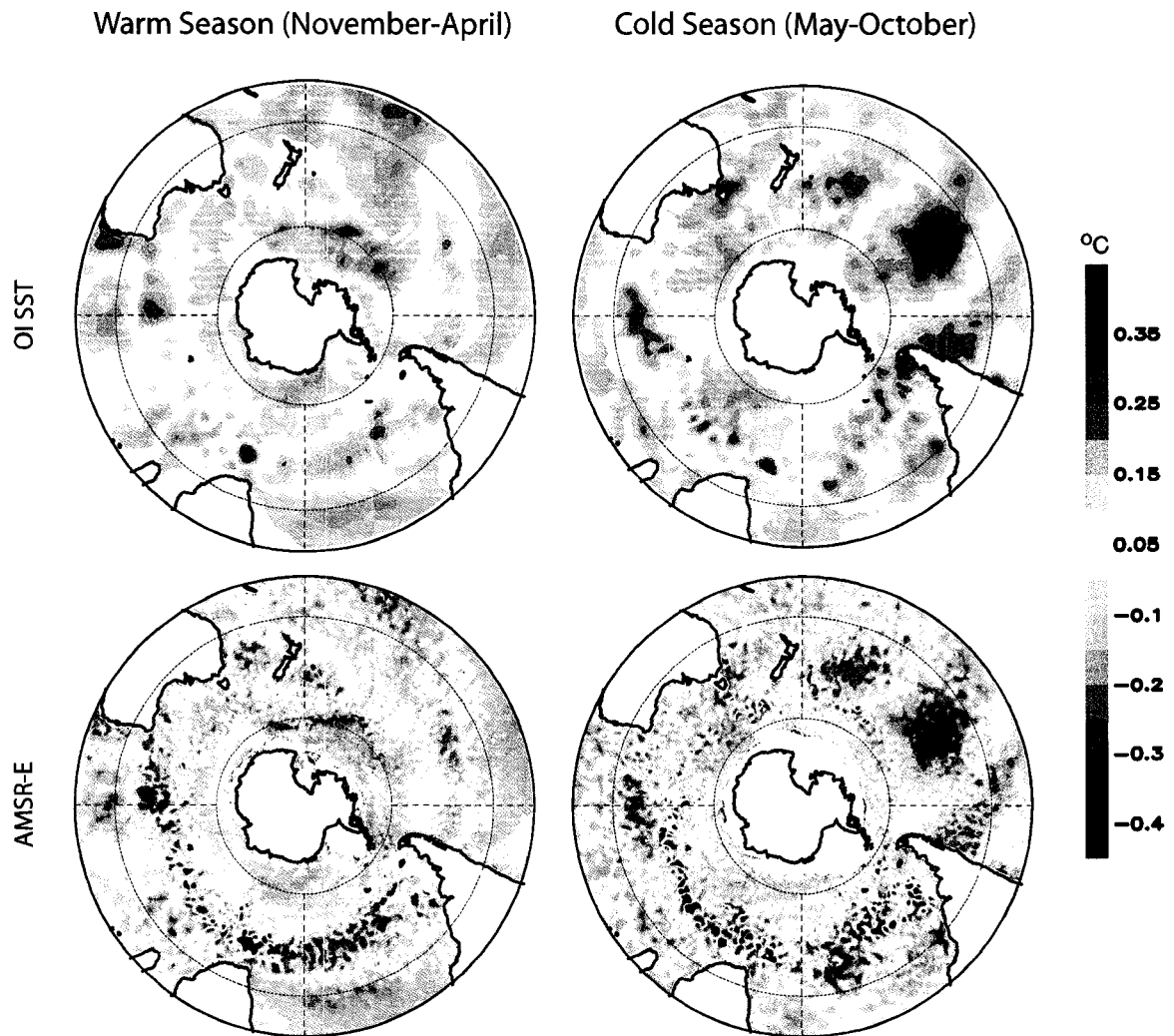


Figure 3.6. Monthly-mean SST anomalies regressed onto the standardized SAM index for (top row) OI SST data and (bottom row) AMSR-E SST data for the period 2002-present. The left column denotes warm season (November-April) results and the right column denotes cold season (May-October) results.

### Regressions of SST Anomalies onto ENSO

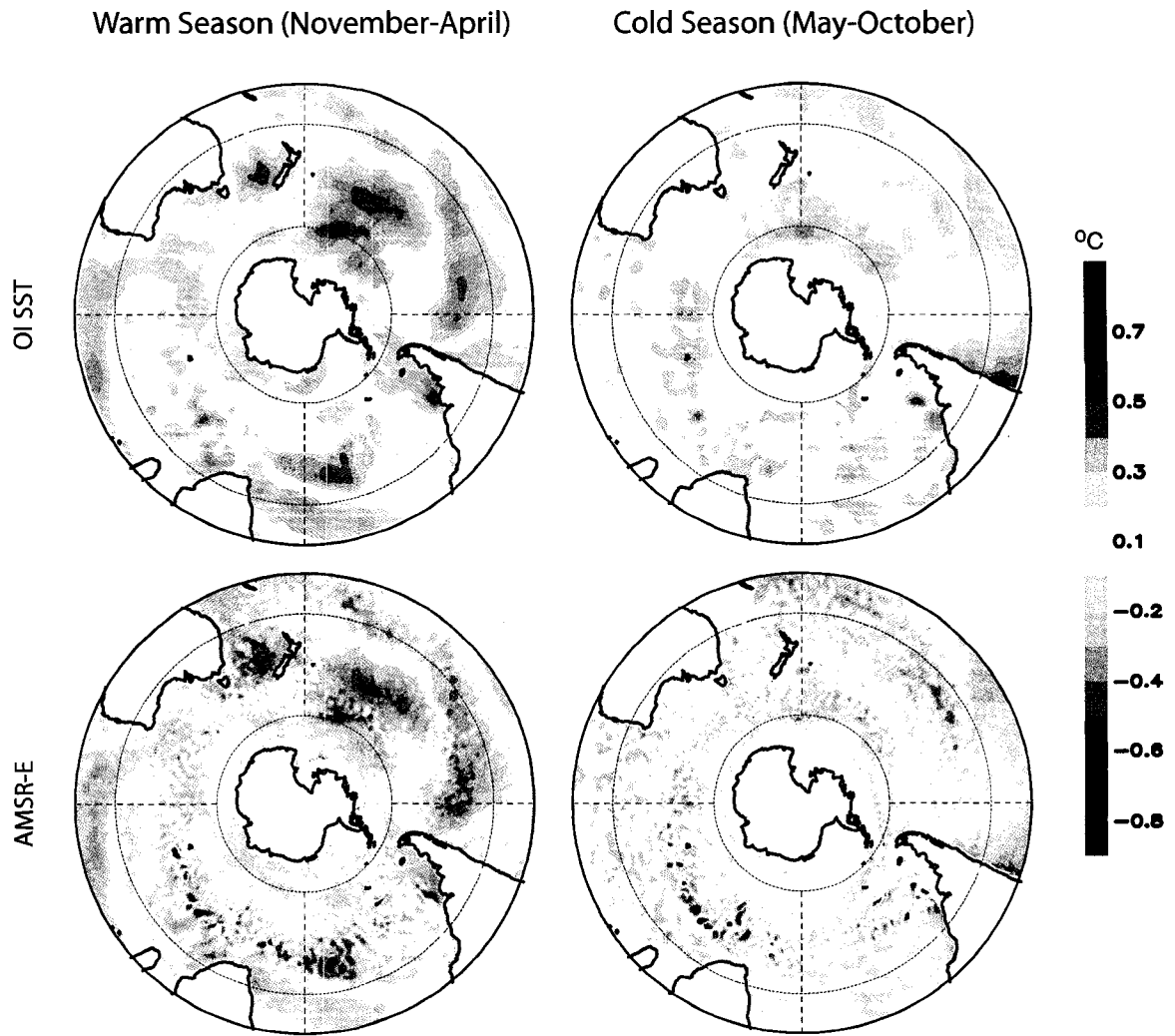


Figure 3.7. As in Figure 3.6 but regressions are based on the standardized ENSO index. Positive values of the ENSO index denote cold conditions in the eastern tropical Pacific.

## Regressions on the SAM

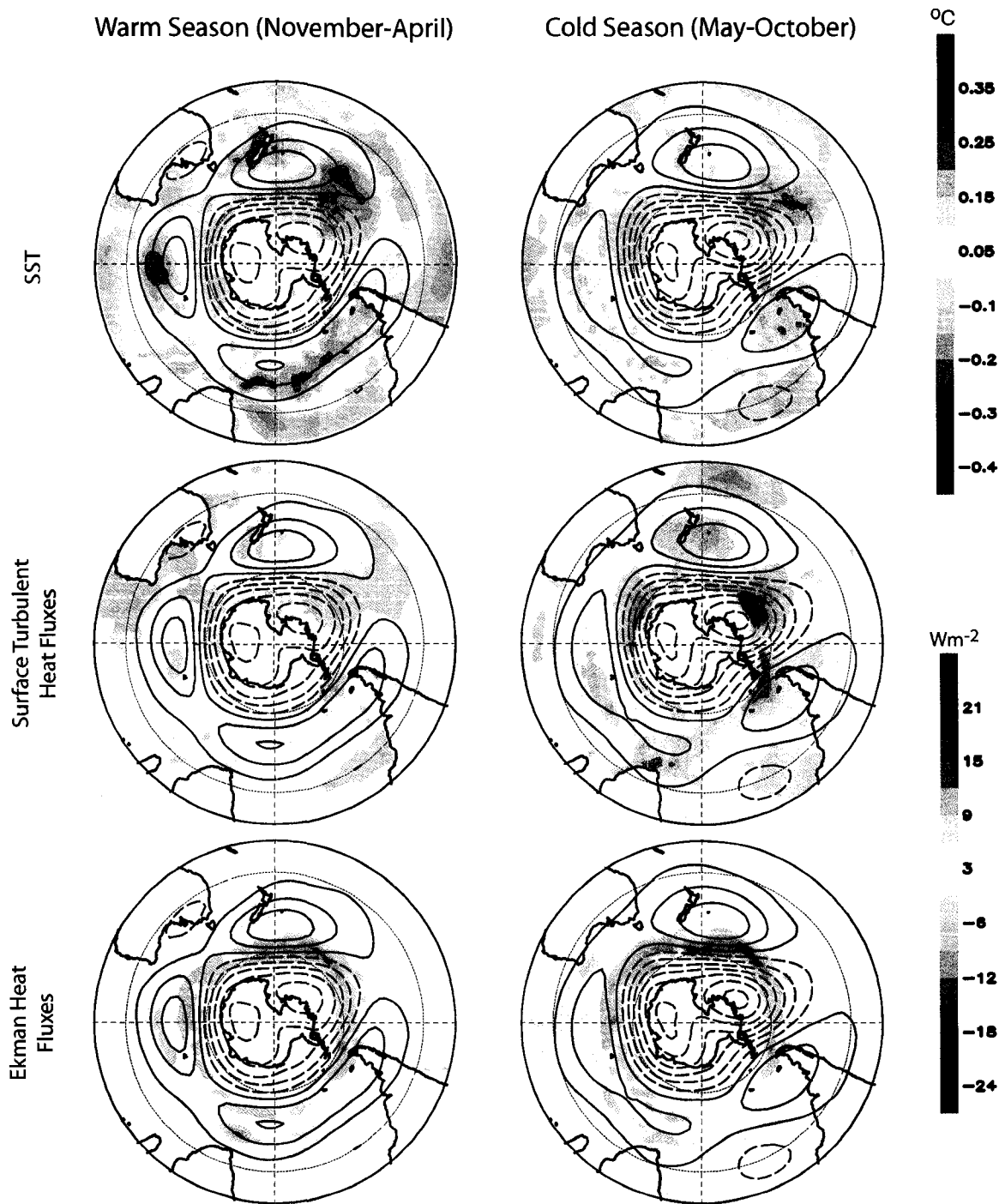


Figure 3.8. Regressions of monthly-mean (all panels; contours)  $Z_{500}$ , (top; shading) SST, (middle; shading) surface turbulent heat flux and (bottom; shading) Ekman heat flux anomalies regressed onto the SAM index. Positive (negative) contours correspond to solid (dashed) lines and are drawn at (-5m, 5m, 15m...). The left column denotes warm season (November-April) and the right column denotes cold season (May-October) results. The positive heat fluxes are directed into the ocean.

## Regressions on ENSO

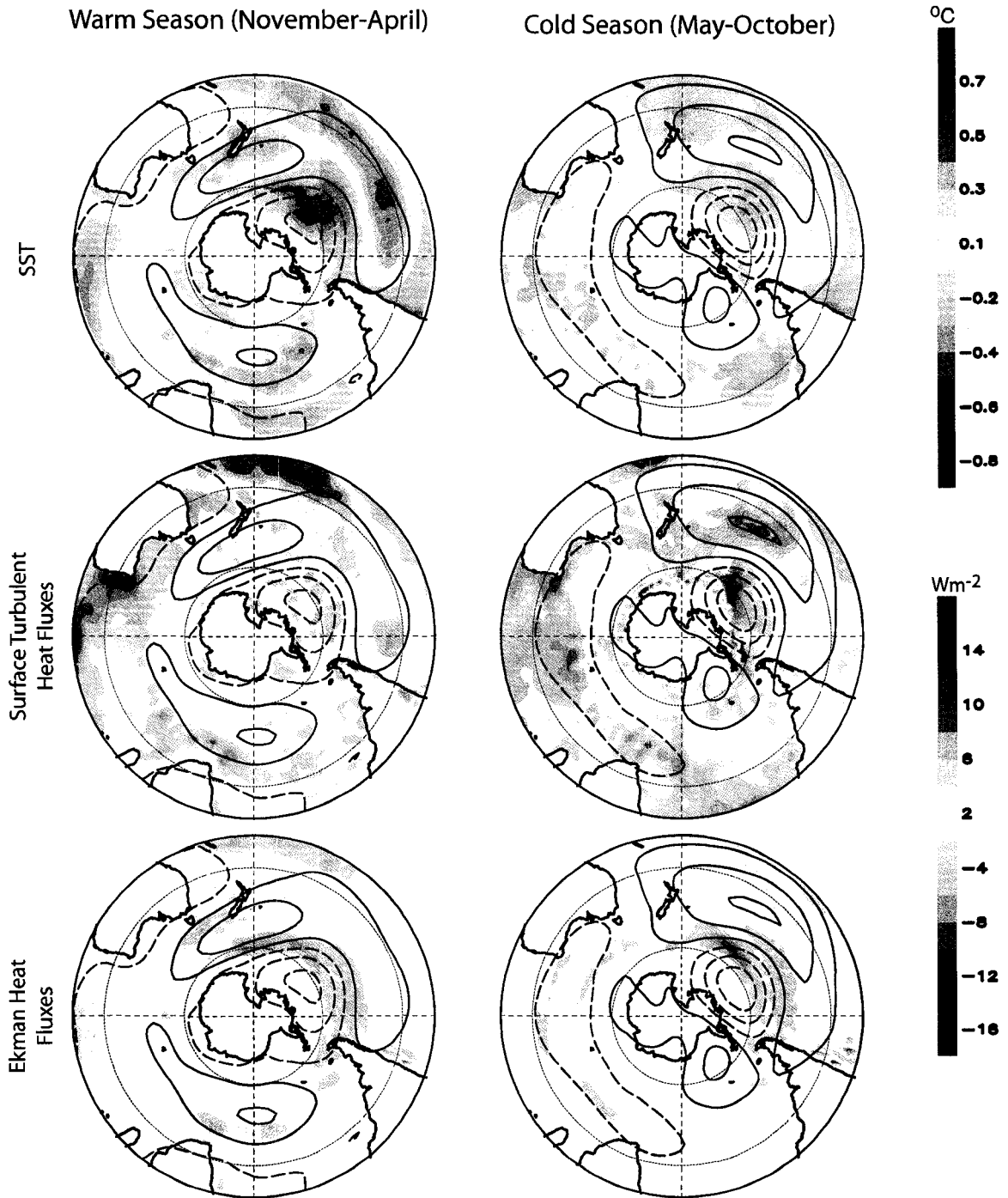


Figure 3.9. As in Figure 3.8 but the regressions are based on the standardized ENSO index. Positive values of the ENSO index denote cold conditions in the eastern tropical Pacific. Note that the color scales have changed from Figure 3.8.

### Seasonal Mean Regressions of Fluxes onto ENSO

Warm Season (November-April)

Cold Season (May-October)

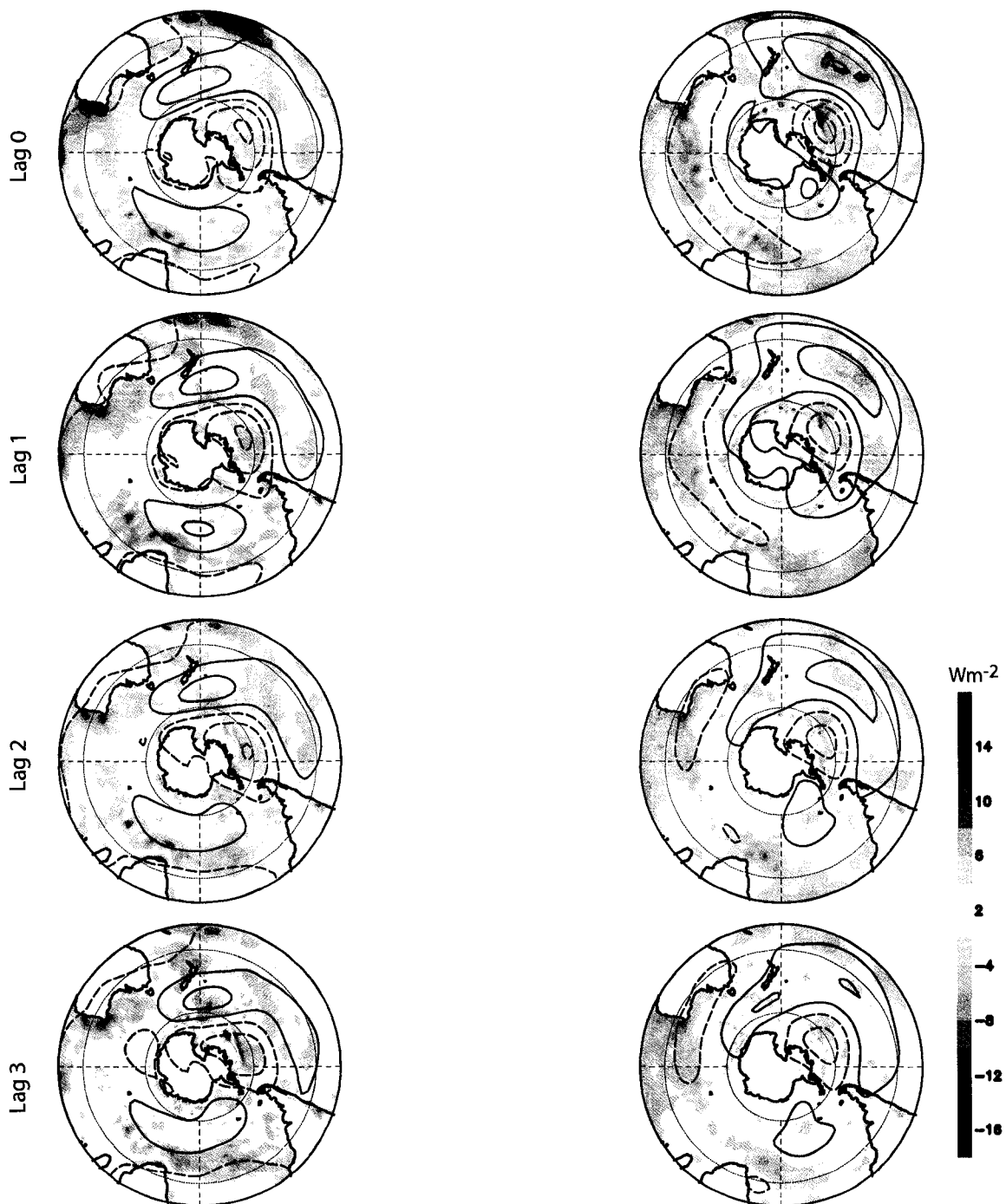


Figure 3.10. Seasonal mean turbulent heat flux anomalies regressed onto the ENSO index at lag (top) 0 month, (second from top) 1 month, (second from bottom) 2 months, and (bottom) 3 months for (left) warm and (right) cold seasons. For example, the second from top left panel corresponds to December-May mean surface heat fluxes regressed onto November-April mean ENSO. Positive values of the ENSO index denote cold conditions in the eastern tropical Pacific. Positive heat fluxes are directed into the ocean.

## Regressions of Fluxes onto ENSO

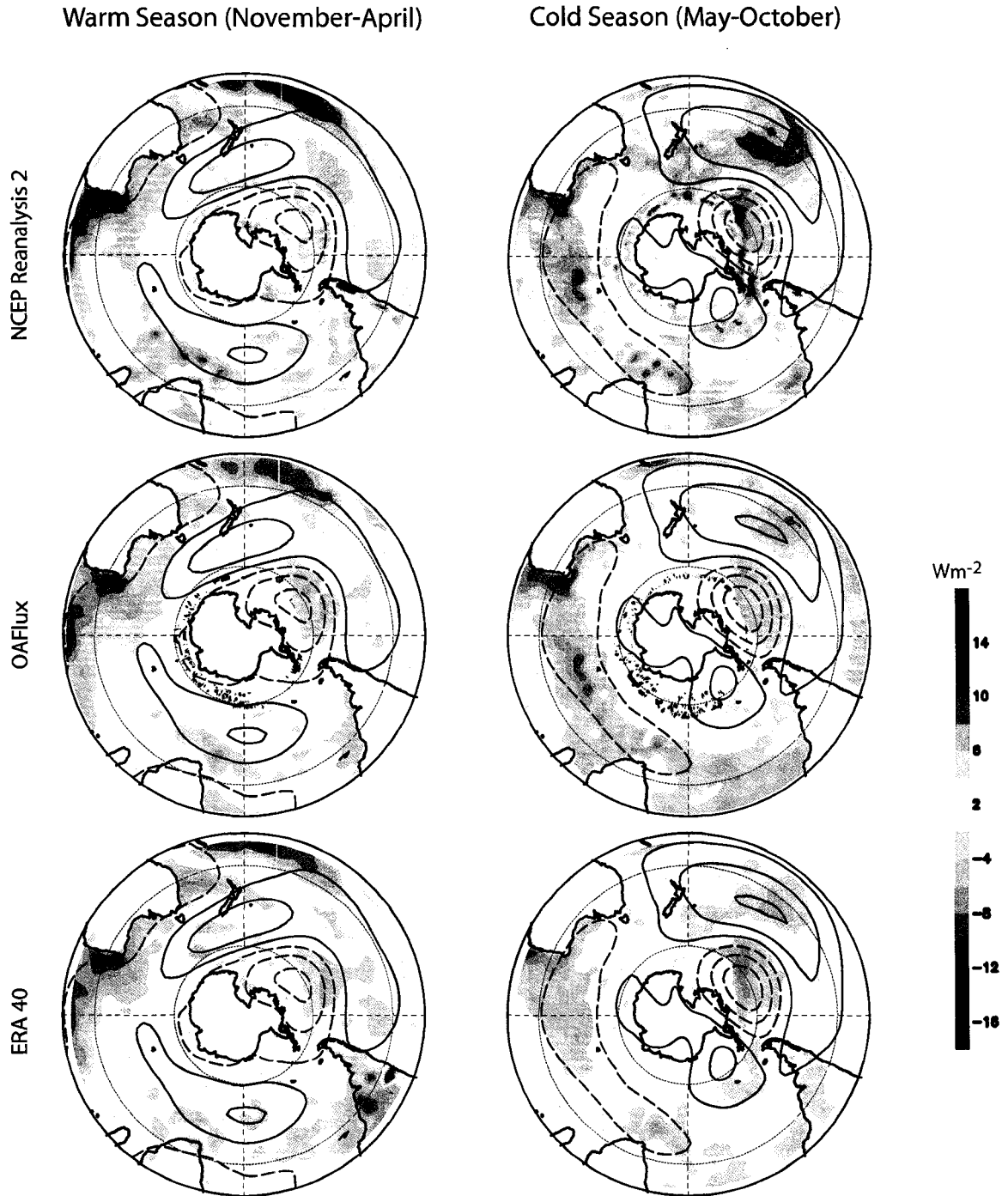


Figure 3.11. Regressions of monthly-mean surface turbulent heat fluxes onto the ENSO index for (top row) NCEP-Reanalysis 2 data (middle row) OAFIux data and (bottom row) ERA-40 data. The left column denotes warm season (November-April) and the right column denotes cold season (May-October) results. Positive values of the ENSO index denote cold conditions in the eastern tropical Pacific. The positive heat fluxes are directed into the ocean.

Warm Season (November-April)

Cold Season (May-October)

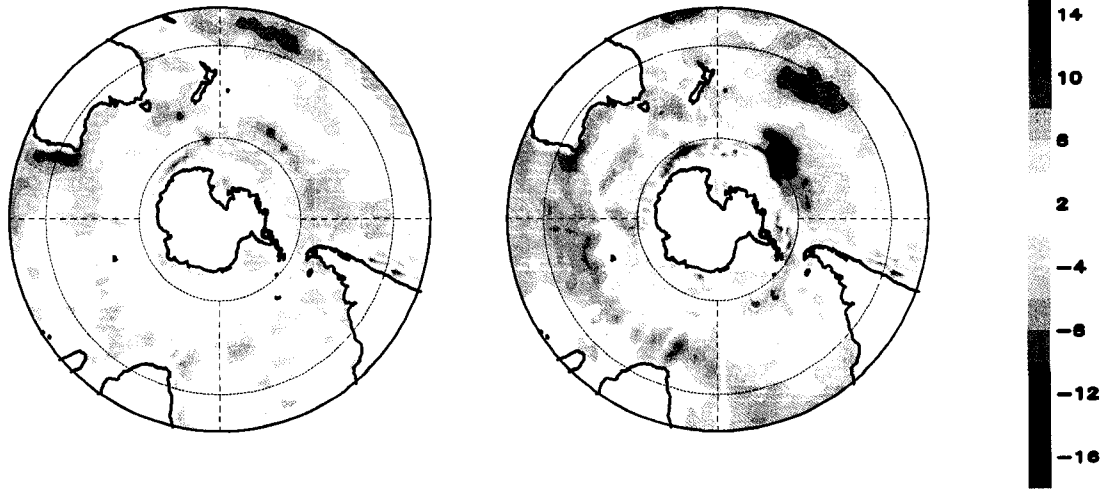


Figure 3.12. Regressions of monthly-mean combined heat flux (surface turbulent + Ekman heat fluxes) anomalies regressed onto ENSO. The left column denotes warm season (November-April) and the right column denotes cold season (May-October) results. Positive values of the ENSO index denote cold conditions in the eastern tropical Pacific. The positive heat fluxes are directed into the ocean.

Warm Season (November-April)

Cold Season (May-October)

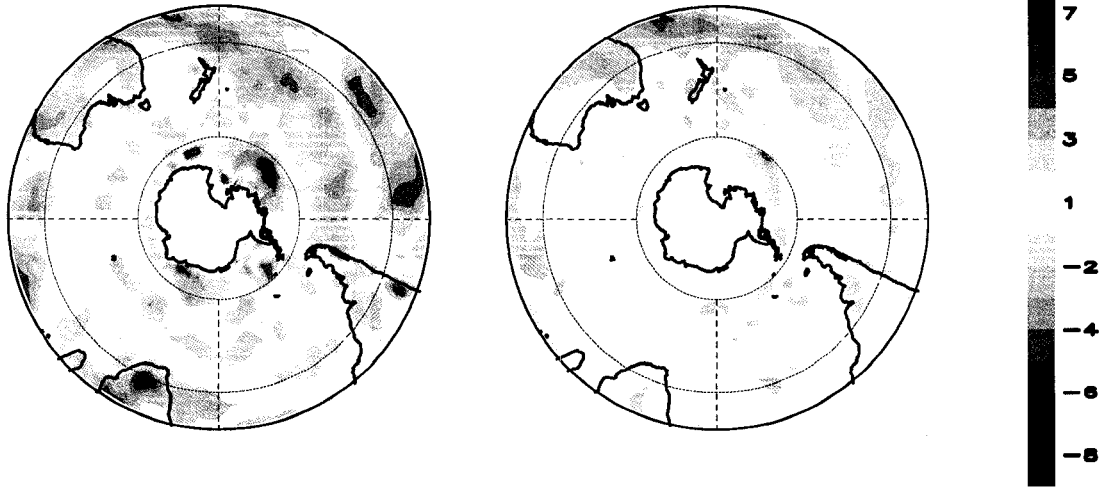


Figure 3.13. Regressions of monthly-mean shortwave radiation anomalies regressed onto ENSO. The left column denotes warm season (November-April) and the right column denotes cold season (May-October) results. Positive values of the ENSO index denote cold conditions in the eastern tropical Pacific. The positive heat fluxes are directed into the ocean.

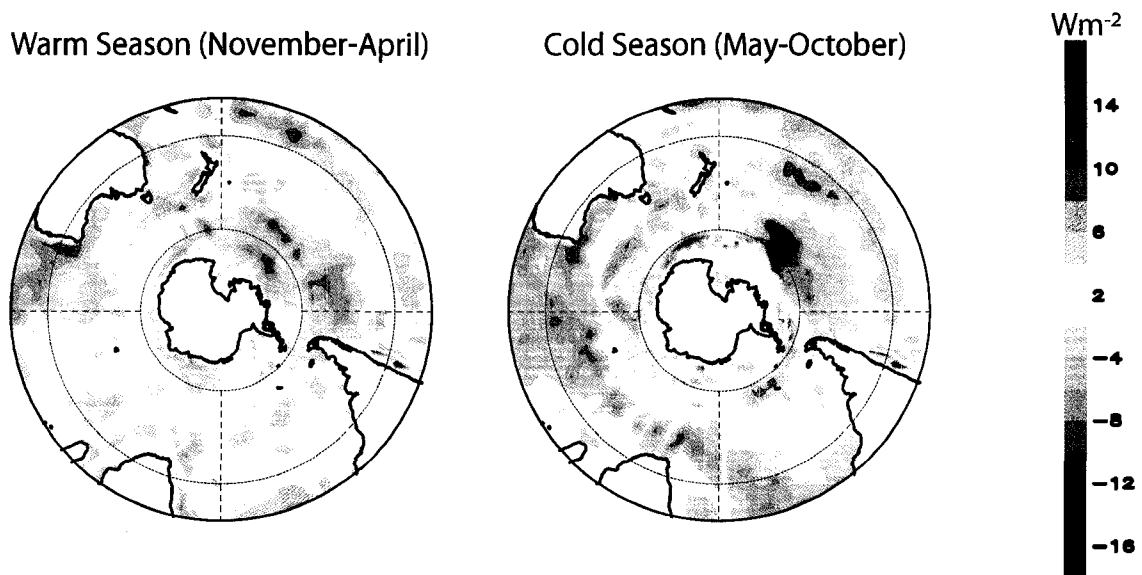


Figure 3.14. Regressions of monthly-mean heat flux (surface turbulent heat + Ekman heat + shortwave radiation) anomalies regressed onto ENSO. The left column denotes warm season (November-April) and the right column denotes cold season (May-October) results. Positive values of the ENSO index denote cold conditions in the eastern tropical Pacific. The positive heat fluxes are directed into the ocean.

Table 3.1. Correlation coefficients between the leading PC time series of the monthly-mean SH SST anomalies and the expansion coefficient time series for the SAM and ENSO-related SST regression maps from the top and middle panels of Figure 3.3. See text for details.

	Leading PC <sub>SST</sub> Time Series (Cold Season)	Leading PC <sub>SST</sub> Time Series (Warm Season)
Expansion Coefficient Time Series of SAM-related SSTs	0.55	0.91
Expansion Coefficient Time Series of ENSO-related SSTs	0.93	0.99

## **CHAPTER FOUR**

### **TEMPORAL EVOLUTION AND PERSISTENCE OF SOUTHERN HEMISPHERE SEA SURFACE TEMPERATURE ANOMALIES ASSOCIATED WITH THE SOUTHERN ANNULAR MODE**

#### **4.1 Overview**

The previous chapter revealed the patterns of extratropical Southern Hemisphere (SH) sea surface temperature (SST) variability associated with the Southern Annular Mode (SAM) and El Niño Southern Oscillation (ENSO) based on contemporaneous regressions using monthly-mean data. In this chapter, we use weekly-mean data to analyze the temporal evolution of the relationship between the SAM and the extratropical SH SST field, and examine in detail the persistence of the SAM-related SST anomalies. Because ENSO variability is strongest on seasonal time scales, the following analyses of weekly data focus on the lagged relationships between extratropical SH SST anomalies and the SAM.

#### **4.2 Relationships between the SAM and SH SST Anomalies on Weekly Timescales**

To examine the temporal evolution of the relationships between the SAM and the extratropical SH SST field, we use lagged correlation/regression analysis between weekly-mean values of SST anomalies and the SAM index. Results are based on the 26-week cold (warm) season extending from the first week of May (November) to the last week in October (April). The regressions/correlations are centered about the middle 10 weeks of each season and are lagged from -8 (SST leads) to +8 (SST lags) weeks.

Figure 4.1 shows maps formed by regressing weekly-mean SST anomalies onto standardized values of the SAM index at lags ranging from -8 (top row) to +8 (bottom row) weeks for the warm (left) and cold (right) seasons. During both seasons, the structures of SST anomalies are comparable to the contemporaneous monthly-mean regression maps shown in the top panels of Fig. 3.3. The weekly regression maps exhibit similar structure at all lags, but have largest amplitude following lag 0. As is the case for the monthly regressions, the amplitudes of the SST anomalies are somewhat higher during the warm season (note the color scales for the warm and cold season regression maps in Fig. 4.1 are different).

Figure 4.2 shows the lag correlations between the SAM index and the expansion coefficient time series of the lag 0 SST maps in Fig. 4.1. The expansion coefficient time series (hereafter  $SAM_{SST}$ ) were formed by projecting the anomalous weekly-mean SST field onto the lag 0 regression maps from Fig. 4.1. In practice, qualitatively similar time series are derived by projecting the SST field onto regression maps for other lags.

During both the warm and cold seasons, the lag correlations between the SAM and its associated pattern of SST anomalies are largest and most statistically significant when variations in the SAM precede variations in the SST field by  $\sim 1$  week, at which time  $r > 0.4$ . The lag correlations exhibit a marked asymmetry about lag 0 in which the correlations are weak when SSTs lead by 8 weeks ( $r \sim 0.1$ ) but remain statistically significant when SSTs lag by 8 weeks ( $r \sim 0.35$ ). The slow decay of the lag correlations after lag 0 attests to the substantial persistence of the SH SST field. Note that when SSTs lag the SAM, the magnitude of the correlation coefficients are virtually identical in both

seasons, but when SSTs lead the SAM, the correlation coefficients are slightly stronger in the cold season.

### 4.3 Persistence of the SAM-SST Relationship

The persistence of the SAM and its impact on the SH SST field is investigated further in Figures 4.3-4.6. The top panel in Figure 4.3 shows the lag autocorrelations of the  $SAM_{SST}$  time series for the austral warm season (dashed), the austral cold season (dotted), and all seasons (solid) for lags up to 13 weeks (i.e., the length of the cold and warm seasons used in the analyses). The bottom panel in Fig. 4.3 shows the seasonally stratified lag autocorrelations for the SAM index time series. The all-season lag autocorrelation function of the  $SAM_{SST}$  time series is repeated as the solid line in Figure 4.4 for lags up to 52 weeks.

The most obvious feature in the autocorrelation plots in Fig. 4.3 is the marked persistence of the  $SAM_{SST}$  pattern relative to the SAM itself: the  $e$ -folding time scale of the SAM index is roughly two weeks (Fig. 4.3, bottom), whereas the  $e$ -folding timescale of its expression in the SST field is on the order of 26 weeks (Fig. 4.3, top; Fig. 4.4, thin solid line). The  $SAM_{SST}$  time series exhibits slightly more persistence during the cold season (Fig. 4.3, top), whereas the SAM index time series exhibits slightly more persistence during the warm season (Fig. 4.3, bottom).

As discussed in previous sections, the SAM and ENSO are significantly related during the austral warm season. Consequently, a fraction of the persistence of the SAM and  $SAM_{SST}$  time series during the austral warm season is due to the relatively low frequency variability inherent in ENSO. Figure 4.5 is analogous to Fig. 4.3, but in all

cases ENSO has been linearly regressed from the SAM and SAM<sub>SST</sub> time series before calculating the lag autocorrelations. The persistence of the cold season time series is unchanged when ENSO is removed from the data (compare the dotted lines in Figs. 4.3 and 4.5), which is consistent with the fact ENSO and the SAM are not related during that season. But the removal of ENSO has a notable impact on the persistence of the SAM<sub>SST</sub> time series during the warm season and, by extension, across all seasons (compare the dashed and solid lines in the top panels in Figs. 4.3 and 4.5). In fact, as evidenced in Fig. 4.4, the *e*-folding timescale of the SAM<sub>SST</sub> time series for all seasons is reduced from 26 weeks to 18 weeks after ENSO is linearly regressed from the data. Comparing Figs. 4.3 and 4.5, it is clear that after ENSO has been removed from the data, the persistence of the SAM<sub>SST</sub> pattern is substantially larger during the winter months than it is during the summer months. Note that ENSO accounts for a relatively small fraction of the warm season persistence of the SAM index itself (compare the dashed lines in the bottom panels of Figs. 4.3 and 4.5). Furthermore, the results are not strongly impacted by trends in the data (i.e., compare the results in Figs. 4.5 and 4.6).

The ENSO-residual SAM<sub>SST</sub> time series in Figs. 4.5 and 4.6 may be viewed as reflecting more precisely the direct effect of the SAM on the SH SST field. Why does the impact of the SAM on the SST field exhibit more persistence during winter despite the fact the atmospheric forcing (i.e., the SAM index) exhibits comparable persistence between seasons? One possible explanation lies in the seasonally varying depth of the ocean mixed layer. The relationship between the mixed layer depth and persistence in SST anomalies can be illustrated in the context of the simple stochastic climate model as described by Frankignoul and Hasselman (1977):

$$\rho c_p H \frac{dT'}{dt} = F' - \lambda T' \quad (4.1)$$

where  $\rho$  and  $c_p$  are the density and heat capacity of sea water, respectively;  $H$  is the depth of the ocean mixed layer;  $T'$  is the anomalous sea surface temperature;  $\lambda$  is a linear damping parameter and  $F'$  is the anomalous atmospheric forcing. If the anomalous atmospheric forcing is white in time, Eq. (4.1) yields the following autocorrelation function for  $T'$ :

$$r(\tau) = e^{-\lambda\tau/\rho c_p H} \quad (4.2)$$

where  $r(\tau)$  is the autocorrelation function of  $T'$  as a function of lag  $\tau$  (see Frankignoul and Hasselman 1977; Deser et al. 2003). From Eq. (4.2) it is apparent that, all other factors being held equal, the decay timescale of  $T'$  decreases exponentially as  $H$  increases.

Figure 4.7 shows solutions to Eq. (4.2) for two different values of mixed layer depths,  $H=35$  m and  $H=90$  m (thick solid and dashed lines), superposed on the warm and cold season lag autocorrelations of the ENSO-residual  $SAM_{SST}$  time series reproduced from the top panel in Fig. 4.5 (thin solid and dashed lines in Fig. 4.7). When solving for Eq. (4.2), we have set  $\rho=1000$  kg/m<sup>3</sup> and  $c_p=4218$  J kg<sup>-1</sup> K<sup>-1</sup>, and have defined the linear damping parameter as  $\lambda=20$  W m<sup>-2</sup> K<sup>-1</sup> ( $20$  W m<sup>-2</sup> K<sup>-1</sup> represents an approximate average value of the damping coefficients used in previous studies of the persistence of the middle latitude oceans, e.g., Deser et al. 2003). The mixed layer depths of  $H=35$  m and  $H=90$  m are chosen because they provide close fits to the observed autocorrelations, but the values also correspond to physically reasonable estimates of the depth of midlatitude SH mixed layer during the warm and cold seasons, respectively (e.g., the hemispheric

mean (20°-80°S) mixed layer depths in Fig. 3.2 are ~50 m during the warm season and ~95 m during the cold season).

The results in Fig. 4.7 assume fixed linear damping of  $\lambda=20 \text{ W m}^{-2} \text{ K}^{-1}$ , which was chosen based on previous studies examining persistence of extratropical SSTs in the Northern Hemisphere (e.g., Deser et al. 2003). If our estimate of  $\lambda$  for the Southern Ocean is larger than reality then Fig. 4.7 overestimates the true lag-autocorrelation function; if  $\lambda$  is smaller than reality then the results underestimate the lag-autocorrelation function.

The stochastic climate model described in Frankignoul and Hasselman (1977) is a simplification of ocean-atmosphere interaction and neglects several factors that may impact the persistence of extratropical SST anomalies, including, for example, mixed layer dynamics (e.g., Deser et al. 2003), ocean dynamics, forcing of SST anomalies by multiple phenomena (e.g., Newman 2007), and the strength of ocean-atmosphere coupling (e.g., Barsugli and Battisti 1998). However, from Fig. 4.7 it is clear that physically reasonable differences in the depth of the Southern Ocean mixed layer are sufficient to explain the observed differences in the persistence of the  $\text{SAM}_{\text{SST}}$  time series between warm and cold seasons. A seasonal mean mixed layer depth of 50 m provides a very close fit to the observed persistence of the  $\text{SAM}_{\text{SST}}$  time series based on data for all calendar months (Figure 4.8, heavy shaded line).

Thus the calculations in Figs. 4.7 and 4.8 do not provide an exact quantification of the impacts of the seasonally varying mixed layer on the persistence of SST anomalies, but rather provide evidence that the persistence of the extratropical SH SST anomalies

associated with the SAM is consistent with the damped thermal response to relatively white atmospheric variability.

#### **4.4 Concluding Remarks**

The key results of this chapter are the following:

*1) Extratropical SH SST anomalies associated with the SAM are largest roughly one week after large changes in the atmospheric flow and persist for up to several months.*

The correlations between the SAM and its associated pattern of extratropical SH SST anomalies are strongest and most statistically significant when the SST field lags the SAM by ~ 1 week and remain significant for lags up to several months. Correlations are much weaker for periods when the SAM lags the SST field, and there is no evidence of a distinct pattern of weekly extratropical SH SST anomalies that precedes variability in the SAM. The observed persistence of the pattern of SST anomalies associated with the SAM is consistent with the simulated persistence of SAM-related SST anomalies revealed in Sen Gupta and England (2006).

*2) The seasonally varying persistence of the pattern of SST anomalies associated with the SAM is consistent with the seasonally varying depth of the ocean mixed layer.*

SST anomalies associated with the SAM appear at first glance to have comparable persistence during the cold and warm seasons. However, much of the summertime persistence in SST anomalies associated with the SAM is derived from the linear relationship between the SAM and ENSO. When ENSO is linearly regressed from the data, the persistence of the SAM SST anomalies is much less during the warm season than it is during the cold season. The differences in the persistence of the ENSO-residual SST anomalies between the cold and warm seasons is consistent with the seasonal cycle in the depth of the extratropical SH ocean mixed layer.

# Lagged Regressions of Weekly SST Anomalies onto the SAM

Warm Season (November-April)

Cold Season (May-October)

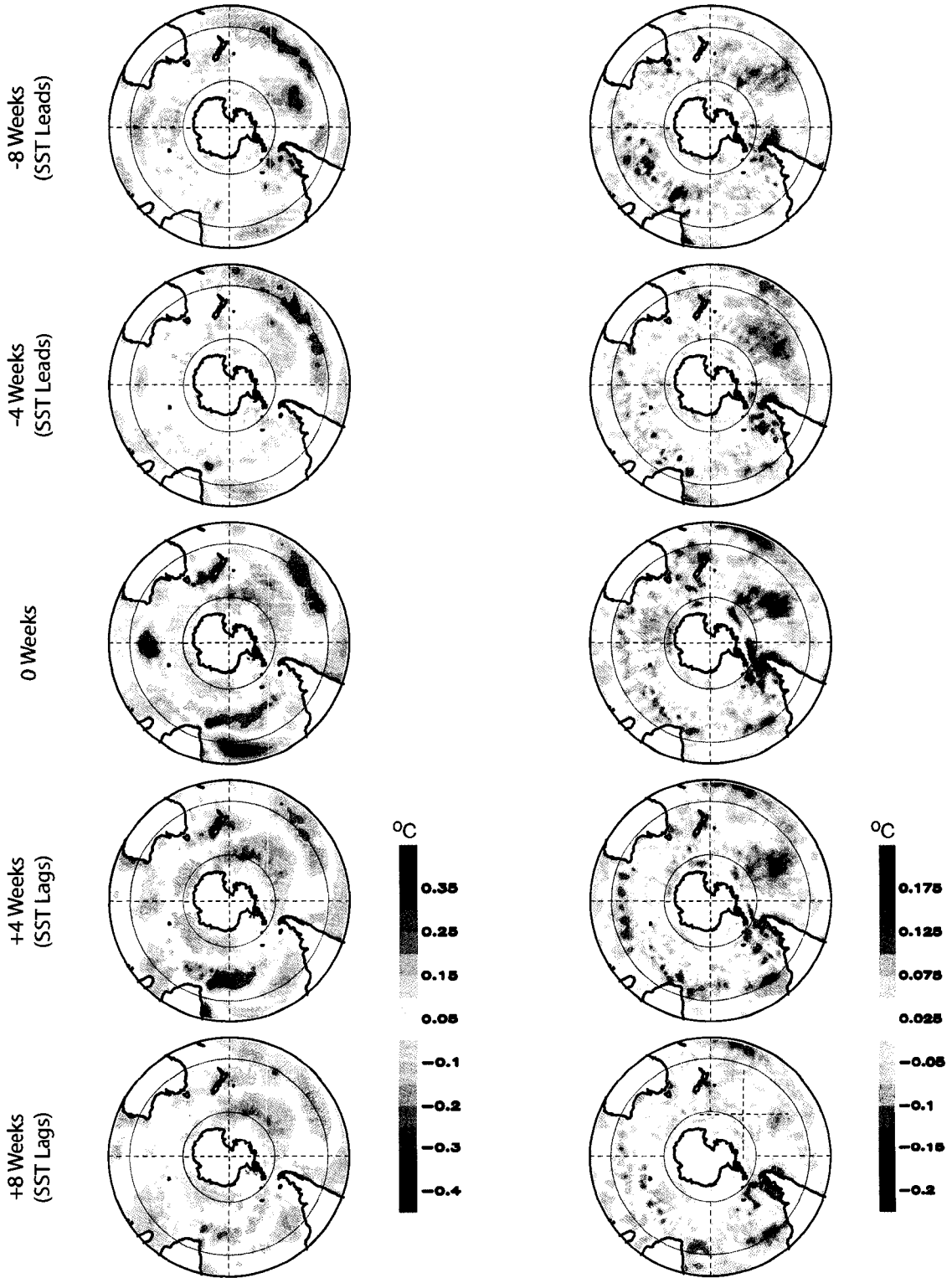


Figure 4.1. Weekly (left column) warm and (right column) cold season SST anomalies regressed onto the SAM index at (top row) lag -8 weeks (SST leads SAM), (second from top row) lag -4 weeks, (middle row) lag 0 weeks, (second from bottom row) lag +4 weeks (SST lags SAM), and (bottom row) lag +8 weeks. Note the color scale differs between warm and cold seasons.

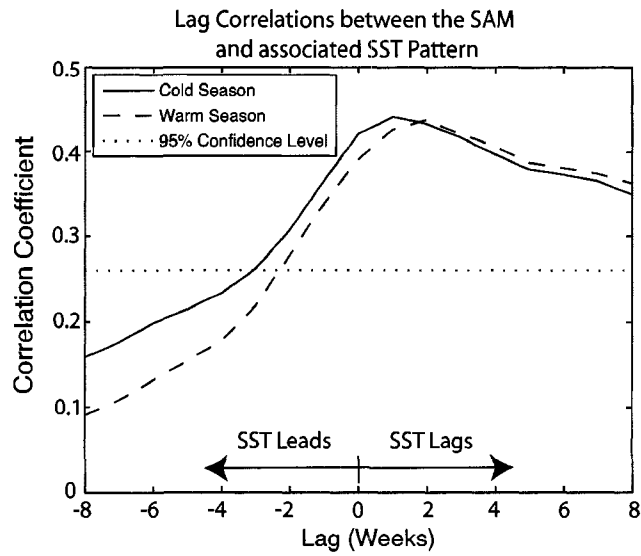


Figure 4.2. Lagged correlation coefficients between the SAM index and the expansion coefficient time series of the anomalous SST pattern associated with the SAM (i.e., the lag zero regression maps from Figure 4.1) for warm (dashed) and cold (solid) seasons. The 95% confidence level is denoted by the dotted line ( $r \sim 0.26$ ).

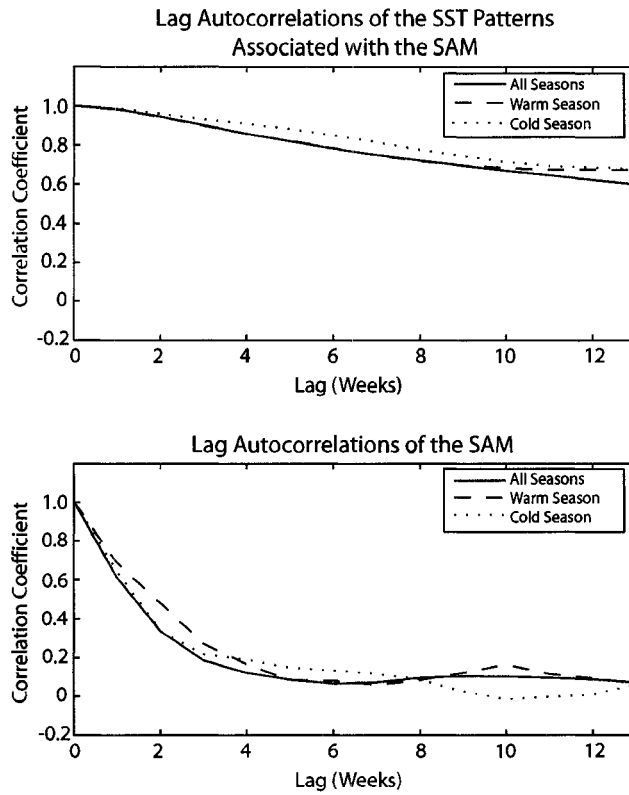


Figure 4.3. Lag autocorrelations of (top) the expansion coefficient time series of the anomalous SST pattern associated with the SAM (i.e., the lag zero regression maps from Figure 4.1) and (bottom) the SAM index for all seasons (solid), warm (dashed) and cold (dotted) seasons. See text for details.

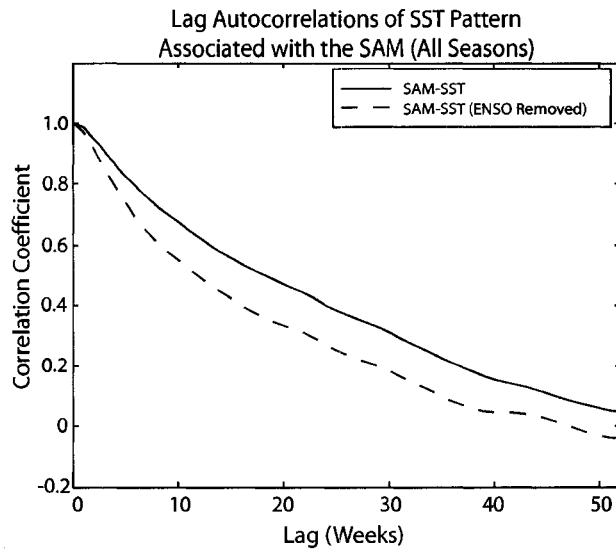


Figure 4.4. Lag autocorrelations of the expansion coefficient time series of the anomalous SST pattern associated with the SAM for all seasons (thin solid) and for all seasons with ENSO linearly regressed from the data (thin dashed) for lags up to 52 weeks.

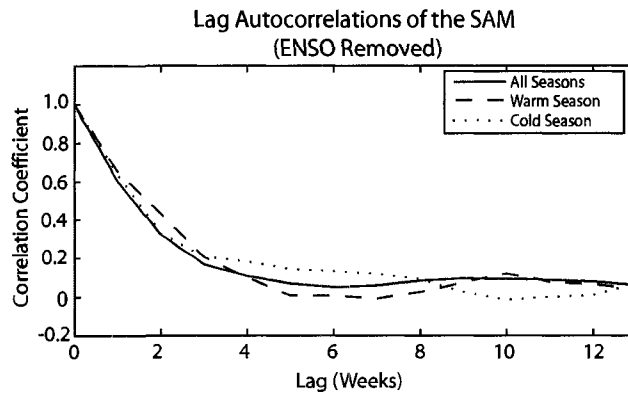
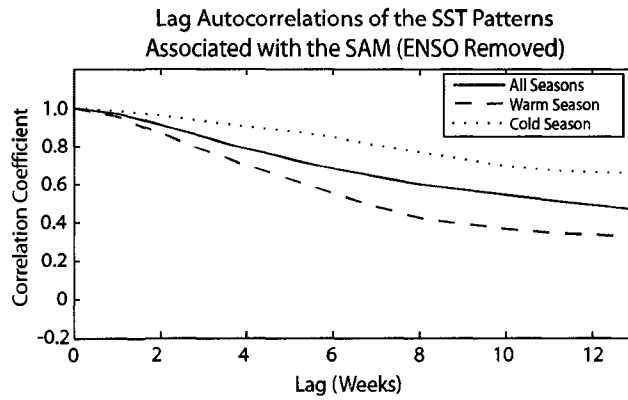


Figure 4.5. As in Figure 4.3 but ENSO has been linearly regressed from both the SAM index and the expansion coefficient time series of the SST pattern associated with the SAM.

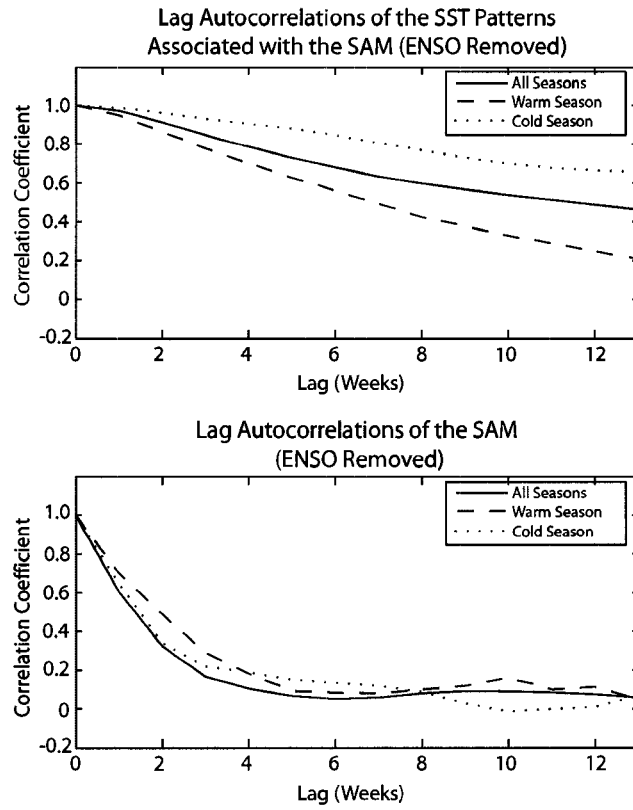


Figure 4.6. As in Figure 4.5 but data have been detrended before calculating the correlation coefficients.

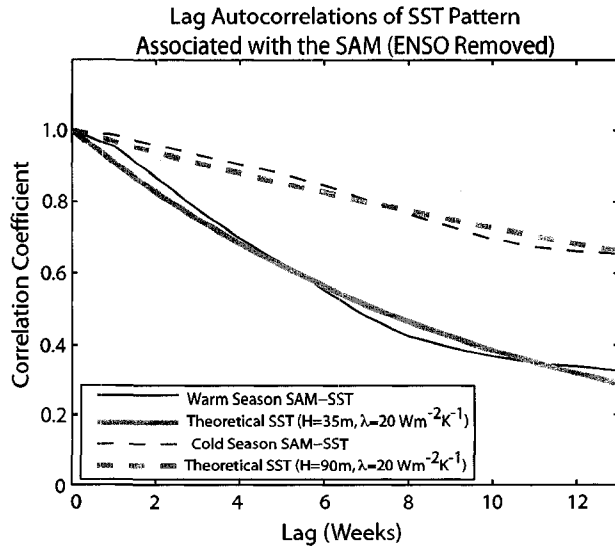


Figure 4.7. Lag autocorrelations of the expansion coefficient time series of the anomalous SST pattern associated with the SAM for warm (thin solid) and cold (thin dashed) seasons (repeated from Figure 4.5, top). The heavy shading represents the solutions to Eq. (4.2) for  $\rho=1000 \text{ kgm}^{-3}$ ,  $c_p=4218 \text{ J kg}^{-1}\text{K}^{-1}$ ,  $\lambda=20 \text{ Wm}^{-2}\text{K}^{-1}$ , and mixed layer depths of  $H=35\text{m}$  (heavy solid shading) and  $H=90\text{m}$  (heavy dashed shading).

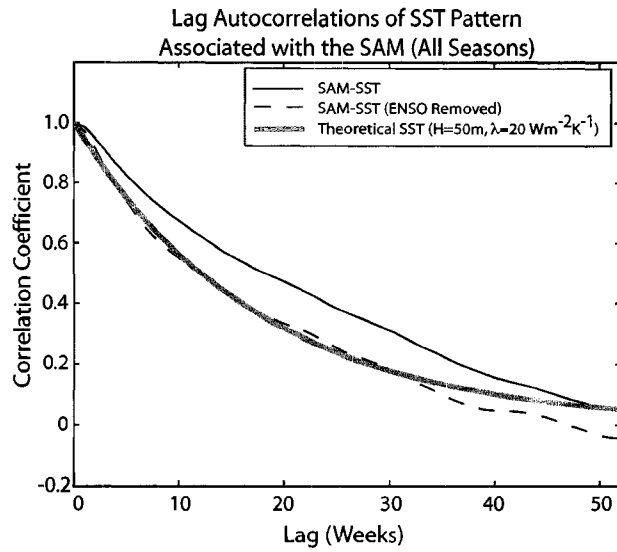


Figure 4.8. As in Figure 4.4 but the heavy shaded line represents the solution to Eq. (4.2) for  $\rho=1000 \text{ kgm}^{-3}$ ,  $c_p = 4218 \text{ J kg}^{-1}\text{K}^{-1}$ ,  $\lambda=20 \text{ Wm}^{-2}\text{K}^{-1}$ , and a mixed layer depth of  $H=50\text{m}$ .

## **CHAPTER FIVE**

### **OBSERVATIONAL EVIDENCE OF REEMERGENCE IN THE EXTRATROPICAL SOUTHERN HEMISPHERE**

#### **5.1 Overview**

The previous chapter demonstrated that seasonal variations in the depth of the mixed layer strongly impact the persistence of extratropical Southern Hemisphere (SH) sea surface temperature (SST) anomalies. As discussed in Chapter 1, the seasonal cycle of the mixed layer depth also influences the persistence of extratropical SST anomalies through “reemergence” in which SST anomalies formed in the late winter are sequestered beneath the relatively shallow summer mixed layer and are then re-entrained into the deepening mixed layer during the following fall/winter. While several studies have extensively examined reemergence in the Northern Hemisphere (NH; see Chapter 1), this is one of the first studies to use observations of subsurface temperatures to document reemergence in the extratropical SH ocean basins.

#### **5.2 Methodology**

Figure 5.1 shows the number of available vertical temperature profiles in the ENSEMBLES (EN3) database (see Chapter 2 for description of EN3 data) for the period 1990-2006 within the extratropical South Pacific sector. In actuality, the EN3 archive extends back to January 1950 but there are virtually no profile data in the SH prior to 1990. After 1990, temperature profiles are concentrated in the following three regions: 1)

off the southeast coast of Australia; 2) to the north of New Zealand; and 3) to the south of Tasmania (Fig. 5.1). Of these regions, only the area north of New Zealand is marked by sufficiently weak currents to allow reemergence to occur. This is because regions of strong ocean currents inhibit reemergence; i.e., temperature anomalies detrained from the mixed layer will be advected away from the source region before they have a chance to reemerge. Therefore, the region east of Australia, which lies in a western boundary current exhibiting strong eddy activity (Nilsson and Cresswell 1981), and the region south of Tasmania, which lies in the Antarctic Circumpolar Current, are less likely to exhibit reemergence.

We thus focus our analysis on the region spanned by  $30^{\circ}$ - $34^{\circ}$ S and  $170^{\circ}$ - $180^{\circ}$ E (dark box outlined in Fig. 5.1). The analysis region lies within the area of high data coverage to the north of New Zealand but away from the influence of coastal processes that might inhibit the reemergence process. To convert monthly-mean temperature profile data within the analysis region into monthly-mean area-averaged anomaly temperature time series at discrete depth levels, the following steps are performed:

1. Because the levels at which temperatures were recorded vary between profiles, the temperatures from each profile were interpolated to nine discrete depth levels: 0, 10, 20, 30, 50, 75, 100, 125, and 150 m.
2. Area-averaged temperatures were computed at all nine depth levels for two subsets of the analysis region:  $30^{\circ}$ - $32^{\circ}$ S,  $170^{\circ}$ - $180^{\circ}$ E and  $32^{\circ}$ - $34^{\circ}$ S,  $170^{\circ}$ - $180^{\circ}$ E. We calculated the area-averaged temperatures for two subsets rather than the entire box because there are substantial gaps in the data and the area-

averaged temperatures will be biased towards the regions with the least missing data. Subdividing the box into two subsets reduces the bias.

3. The seasonal cycle was removed from the area-averaged temperatures found in 2) by subtracting the long-term monthly mean from each month.
4. The temperature anomaly time series for the two subsets of the study region were averaged together to form monthly-mean time series at all nine depths. The resulting nine time series are indicative of monthly-mean temperature anomalies averaged over the region  $30^{\circ}$ - $34^{\circ}$ S,  $170^{\circ}$ - $180^{\circ}$ E at the depth levels given in 1).

### **5.3 The Reemergence Signal in Extratropical South Pacific Subsurface Temperature Observations**

The existence of reemergence is dependent on the amplitude of the seasonal cycle of the depth of the mixed layer: the winter mixed layer must be substantially deeper than the summer mixed layer (Timlin et al. 2002). Figure 5.2 shows the climatological mean temperatures (shading) and mixed layer depths for the region  $30^{\circ}$ - $34^{\circ}$ S,  $170^{\circ}$ - $180^{\circ}$ E. The dashed line corresponds to the mixed layer depths derived from the Ocean Mixed Layer Depth Climatology dataset described in Chapter 2. The solid line corresponds to the mixed layer depths calculated using the EN3 temperature data and the error bars denote the  $\pm 1$  standard deviation range. The mixed layer depths are defined in both datasets as the shallowest depth at which the temperature differs from the temperature at 10 m by  $0.2^{\circ}$ C.

Both data sets reveal a strong seasonal cycle in the depth of the mixed layer. Relatively strong solar heating and weak surface winds during the austral summer drive mixed layer depths no deeper than ~ 25-30 m. Comparatively weak solar heating and strong surface winds drive mixed layer depths as deep as 100 m in the austral winter. For the most part, the interannual standard deviation of the EN3-derived mixed layer depths is relatively small during the warm season months (when the mixed layer is shallow). It is interesting that the standard deviation of the mixed layer depths is much larger during late winter/spring (August-September) than it is during fall/early winter (April-May) despite comparable mixed layer depths observed during these times. One possible explanation for this feature is that the atmospheric circulation, which is partly responsible for driving variations in the depth of the mixed layer, is more vigorous during the late winter season than it is during the fall months.

Figure 5.3 shows the climatological mean mixed layer depths from the EN3 data (solid dark line) superposed on the pattern of concurrent correlations calculated for each month between temperature anomalies at the surface and temperature anomalies at nine depths from 0-150 m. For the most part, the seasonal cycle of the mixed layer depth is mirrored in the pattern of the correlations. In mid-summer, the correlations between temperature anomalies at the surface and at depth exceed 0.8 above ~30 m but decrease to less than 0.4 below 50-75 m. During winter, the correlations exceeding 0.8 are observed at depths down to 100-125 m, demonstrating that the layer of homogeneous ocean temperature anomalies extends considerably deeper at that time.

The most notable difference between the pattern of the correlations in Fig. 5.3 and the climatological mean mixed layer depths from the EN3 data is found in the spring

months (September-November) when the climatological mean mixed layer depth is only ~30-50 m but surface temperature anomalies are strongly correlated with temperature anomalies down to 125-150 m. A similar result was noted in Alexander and Deser (1995), who hypothesized that the depth of the correlations is determined by the scale of the vertical mixing during periods of enhanced springtime storm activity, whereas the depth of the mean mixed layer depth reflects an average over stormy and calm periods. Furthermore, as shown in Fig. 5.2, the vertical gradient in climatological mean temperatures is weak during the late winter/early spring and thus the mixed layer depth is difficult to estimate during this time. An alternative explanation is that since the temperature anomalies at all levels exhibit substantial persistence, then the depth of the correlations during spring are determined by the depth of the vertical mixing during the previous winter.

To evaluate the reemergence signal in the subsurface temperature data, we examine the winter-to-winter evolution of thermal anomalies in the upper ocean. Studies that have investigated reemergence in the NH ocean basins have done so by examining the lag correlations of thermal anomalies from one winter through the following winter (e.g., Alexander and Deser 1995; Alexander et al. 1999). Here we adopt a similar methodology.

Figure 5.4 shows the lag correlations between temperature anomalies at 0 m in (top) August, (middle) September, (bottom) October and temperature anomalies at 0-150 m for 0-13 month lags within the region 30°-34°S, 170°-180°E. The thick black line corresponds to the depths at which correlations with surface temperature anomalies exceed 0.8 (i.e., the 0.8 contour from Fig. 5.3), and shows the approximate layer of

homogeneous upper ocean temperature anomalies. Correlations greater than 0.4 are statistically significant at the 95% confidence level (shading in Fig. 5.4).

As also noted in Fig. 5.3, temperature anomalies in the late winter are highly coupled throughout the top 125-150 m of the ocean. At the surface, the correlations decrease as a function of lag such that by December-January the surface temperature anomalies are no longer significantly correlated with anomalies from the previous September. The decay of the surface temperature anomalies from late winter through summer is consistent with damping by anomalous heat fluxes at the ocean surface. In contrast, the temperature anomalies below the mixed layer in the summer are insulated from atmospheric influences and thus remain significantly correlated throughout the summer season with the subsurface and surface temperature anomalies formed during the previous winter.

The deepening mixed layer throughout the fall allows the thermal anomalies previously sequestered within the seasonal thermocline to be re-entrained into the mixed layer. Thus in June and July, temperature anomalies throughout the mixed layer are impacted by the entrainment process and become significantly correlated with surface temperature anomalies formed during the previous winter. By July, the mixed layer encompasses the entire top 100 meters of the ocean and the surface temperature anomalies that were formed in the previous late winter (and stored beneath the summertime mixed layer) are finally damped to the overlying atmosphere.

The results in Fig. 5.4 suggest that the reemergence signal in the extratropical western South Pacific is robust to small changes in the month in which the SST anomalies are initiated. SST anomalies formed in either August, September, or October

are strongest and most significantly correlated to SST anomalies in the following June-July. The structure of the reemergence signal for temperature anomalies formed in August slightly differs from the other two cases in the following ways: 1) the region of weakly correlated summer surface temperature anomalies is noticeably shallower than the layer of the homogeneous temperature anomalies (i.e., as given by the bold line, which correspond to the 0.8 contemporaneous correlation contour from Fig. 5.3) and 2) the temperature anomalies in the following late-winter/spring do not decay as quickly as observed in the other two cases. Overall, the results in Fig. 5.4 demonstrate that roughly 16-25% of the year-to-year variance of June SST anomalies can be explained by the reemergence of SST anomalies from the previous winter.

The structure of the reemergence signal is also clearly evident if the temperature anomalies below the summer mixed layer are used as a basis for the correlations. Figure 5.5 shows that March temperature anomalies at 75 m are significantly correlated with temperature anomalies at all depths during the previous September-November as well as the following June-July. The results in Fig. 5.5 reveal that the temperature anomalies beneath the summertime mixed layer originate in part from within the mixed layer during the previous winter and are decoupled from contemporaneous temperature anomalies at the surface. Qualitatively similar results to Fig. 5.5 are obtained for correlations based on temperature anomalies at a range of months and depths during the summer season (not shown). Furthermore, the results in Figs. 5.4-5.5 are also broadly consistent with the results of subsurface data in the North Atlantic and North Pacific Oceans (e.g., Alexander and Deser 1995; Alexander et al. 1999; Timlin et al. 2002).

#### **5.4 The Surface Signature of Reemergence across the Extratropical South Pacific**

In this section, monthly-mean Optimum Interpolation (OI) SST anomalies are used to independently investigate the reemergence mechanism across the extratropical southern Pacific Ocean. The OI SST data have considerably larger spatial and temporal coverage than the EN3 temperature data, and thus they allow the reemergence mechanism to be explored over a broader region of the extratropical South Pacific basin than explored in the subsurface observations used in the previous section.

Figures 5.6 and 5.7 show maps formed by correlating SST anomalies in September with SST anomalies in November, January, March, May, July, and September at all grid points in the extratropical South Pacific Ocean. The correlations presented in Fig. 5.6 are calculated for the period 1990-2006, the same period of record used to analyze the subsurface EN3 temperature anomalies in the previous section. Fig. 5.7 shows the correlation maps calculated for the period 1982-2007, the full OI SST record. In Fig. 5.6, the correlations that exceed 0.4 are statistically significant at the 95% confidence level. In Fig. 5.7, the correlations are derived from a larger sample size and thus values exceeding 0.35 are statistically significant at the 95% confidence level.

The patterns in Figs. 5.6 and 5.7 both exhibit a statistically significant reemergence signal in the western part of the extratropical South Pacific basin. In this region, September SST anomalies are weakly correlated with SST anomalies in the spring/summer (January-March) but are strongly correlated with SST anomalies in the following fall/winter (May-September). The amplitude of the correlations tend to be slightly stronger for the period 1990-2006 than for the full record, but the structures are qualitatively similar for both periods.

To more closely examine the robustness of the reemergence signal in the region 30°-34°S, 170°-180°E using the OI SST data, we show in Figure 5.8 the lag correlations between area-averaged SST anomalies based on three different months in which SST anomalies are formed (August, September, and October). Note that the  $x$ -axis in Fig. 5.8 is a function of lag relative to the basis month for the correlations. For example, lag 4 corresponds to correlations between August and December SST anomalies (solid line), September and January SST anomalies (dashed line), and October and February SST anomalies (dotted line).

The results in Fig. 5.8 demonstrate that the reemergence signal in the region 30°-34°S, 170°-180°E is robust to small changes in the month in which the anomalies are initiated, consistent with the results found using the subsurface observations (Fig. 5.4). SST anomalies that are formed in August, September, or October are only weakly correlated with February SST anomalies but are significantly correlated with June SST anomalies. In all three cases, correlations between wintertime SST anomalies and June SST anomalies are  $\sim 0.4$ , a value that is broadly consistent with the subsurface results in Figs. 5.4-5.5.

Figs. 5.6-5.7 not only support the results in the previous section but also highlight the relative lack of reemergence over much of the eastern part of the extratropical South Pacific. It is unclear why reemergence is less discernible over the eastern part of the basin since the ocean mixed layer exhibits a large seasonal cycle there (not shown). It is possible that the SST variability associated with ENSO, which is strongest on interannual time scales, obscures the reemergence signal. However, qualitatively similar results are

obtained when ENSO is linearly regressed from the SST time series at each grid point (not shown).

It is also possible that the lack of reemergence reflects poor data quality: the AVHRR satellite used in part to derive the OI SSTs cannot “see” through the persistent cloud decks in this region (O’Neill et al. 2003), and in situ SST observations are also sparse in this area (see Figure 2.2). Attempts were made to repeat the analysis in Figs. 5.6 and 5.7 using the raw in situ ICOADS data but the data coverage is too sparse in the eastern Pacific and few correlation coefficients could be calculated in the region. The analysis was also repeated using the microwave satellite measurements from AMSR-E, which unlike OI SST, have dense spatial coverage and are not impacted by clouds. The reemergence signal was not discernible in any region of the extratropical South Pacific – including the western South Pacific - using the six years of AMSR-E data, which suggests the AMSR-E record is still too short for studies of interannual SST variability. Finally, there are insufficient subsurface temperature observations in the eastern extratropical South Pacific to repeat the analyses in Figs. 5.4 and 5.5 in that region.

## **5.5 Concluding Remarks**

Previous studies examining the winter-to-winter reemergence of extratropical SST anomalies have focused primarily in the North Atlantic and North Pacific basins (Alexander and Deser 1995; Bhatt et al. 1998; Alexander et al. 1999; Alexander et al. 2001; Timlin et al. 2002). Reemergence has also been noted in observations of sea surface temperatures over the extratropical South Pacific (Hadfield 2000; Hanawa and Sugimoto 2004), Indian and South Atlantic Oceans (Hanawa and Sugimoto 2004). To our

knowledge, this is the first study to explicitly document the existence of reemergence in observations of SH subsurface temperatures. Our analysis of subsurface temperature data is limited by the scarcity of observations in the extratropical SH ocean basins, and is thus restricted to the region 30°-34°S, 170°-180°E, which lies in the western part of the extratropical south Pacific Ocean to the north of New Zealand.

The key findings in this chapter are the following:

*1) Analyses of subsurface temperature observations suggest that wintertime SST anomalies in the western extratropical South Pacific (30°-34°S, 170°-180°E) tend to persist beneath the summer mixed layer and are re-entrained in the subsequent fall/winter.*

The subsurface results show that SST anomalies formed in the western extratropical South Pacific in the late winter/ early spring are significantly related to SST anomalies observed in the following fall/winter but are unrelated to SST anomalies in the intervening summer. The analyses also reveal that temperature anomalies beneath the mixed layer in the summer are strongly correlated with temperature anomalies within the mixed layer during the previous and following winters but are weakly correlated with temperature anomalies within the summer mixed layer. The reemergence of SH wintertime SST anomalies explains ~16-25% of the year-to-year variance in the June SST field over the western South Pacific. The results based on the SH subsurface temperature data are generally consistent with the behavior of reemergence observed in

the NH ocean basins (Alexander and Deser 1995; Alexander et al. 1999; Timlin et al. 2002).

*2) Sea surface temperature data independently confirm the winter-to-winter recurrence of SST anomalies in the extratropical western South Pacific but highlight the absence of reemergence in the extratropical eastern South Pacific.*

It is not understood why reemergence is less noticeable in the eastern part of the extratropical South Pacific basin. One possibility is that the absence of reemergence in the eastern Pacific is physically real. Hanawa and Sugimoto (2004) also did not find evidence of reemergence in this region but they noted their selection criteria and results are “conservative”. Another possibility is that the lack of reemergence reflects poor data quality in the eastern South Pacific. Unfortunately, there are insufficient in situ observations in the region to examine the winter-to-winter evolution of temperature anomalies in subsurface data.

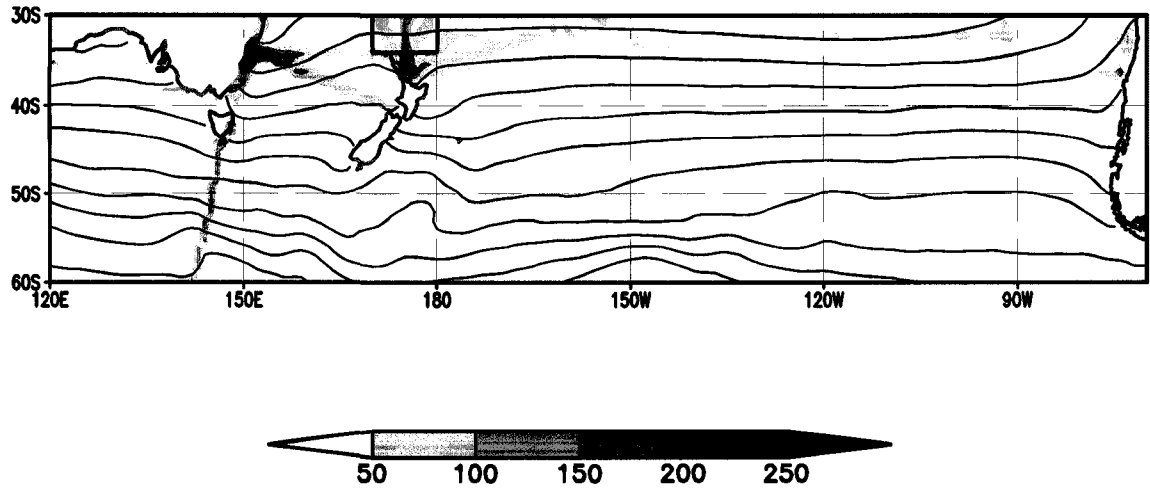


Figure 5.1. Shading denotes the number of profiles recorded within a  $1^\circ \times 1^\circ$  latitude/longitude box for the period 1990-2006. The solid contours denote the climatological annual mean sea surface temperatures. Contours are drawn at  $2^\circ$  intervals. The SST data are obtained from the NOAA OI SST data set described in Chapter 2.

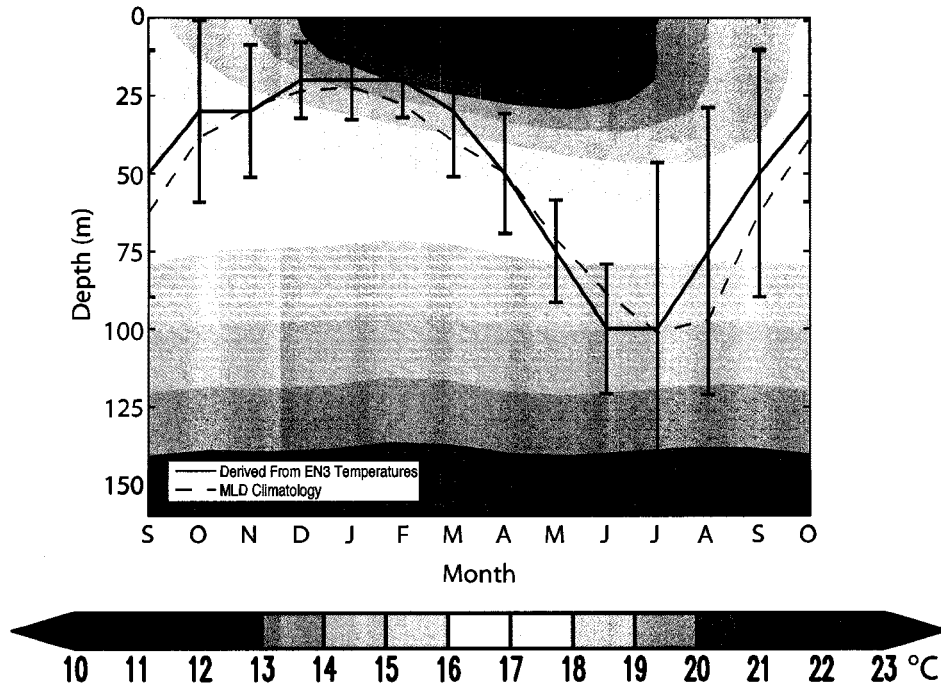


Figure 5.2. Climatological mean temperatures (shading) and mixed layer depths for the region 30°-34°S, 170°-180°E from EN3 temperature data (solid line) and the Ocean Mixed Layer Depth Climatology (dashed line). Error bars denote the  $\pm 1$  standard deviation range of the EN3 mixed layer depths. Mixed layer depths are defined as the shallowest depth at which the temperature differs from the temperature at 10 m by 0.2°C.

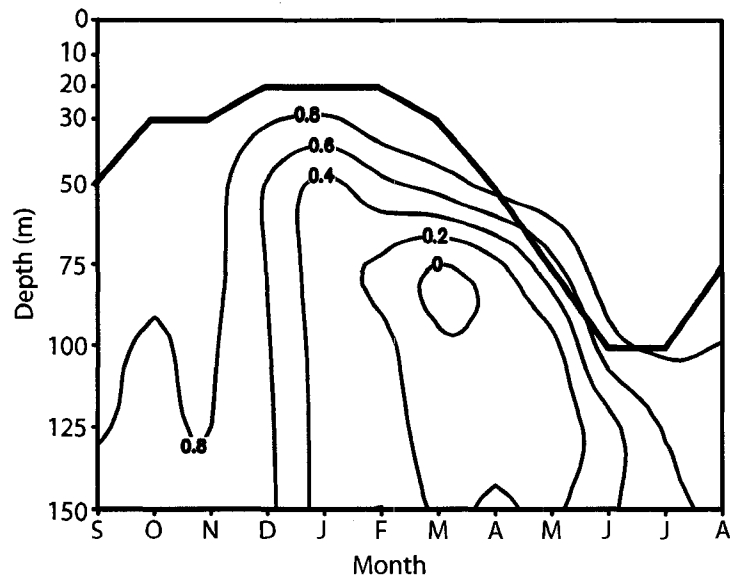


Figure 5.3. Concurrent correlations between monthly-mean temperature anomalies at 0 m and temperature anomalies from 0 m down to 150 m for each month. For example, the correlation coefficient between temperature anomalies at 0 m and temperature anomalies at 50 m in January is 0.4. The thick black line corresponds to the climatological mean mixed layer depths derived from EN3 temperature data from Figure 5.2.

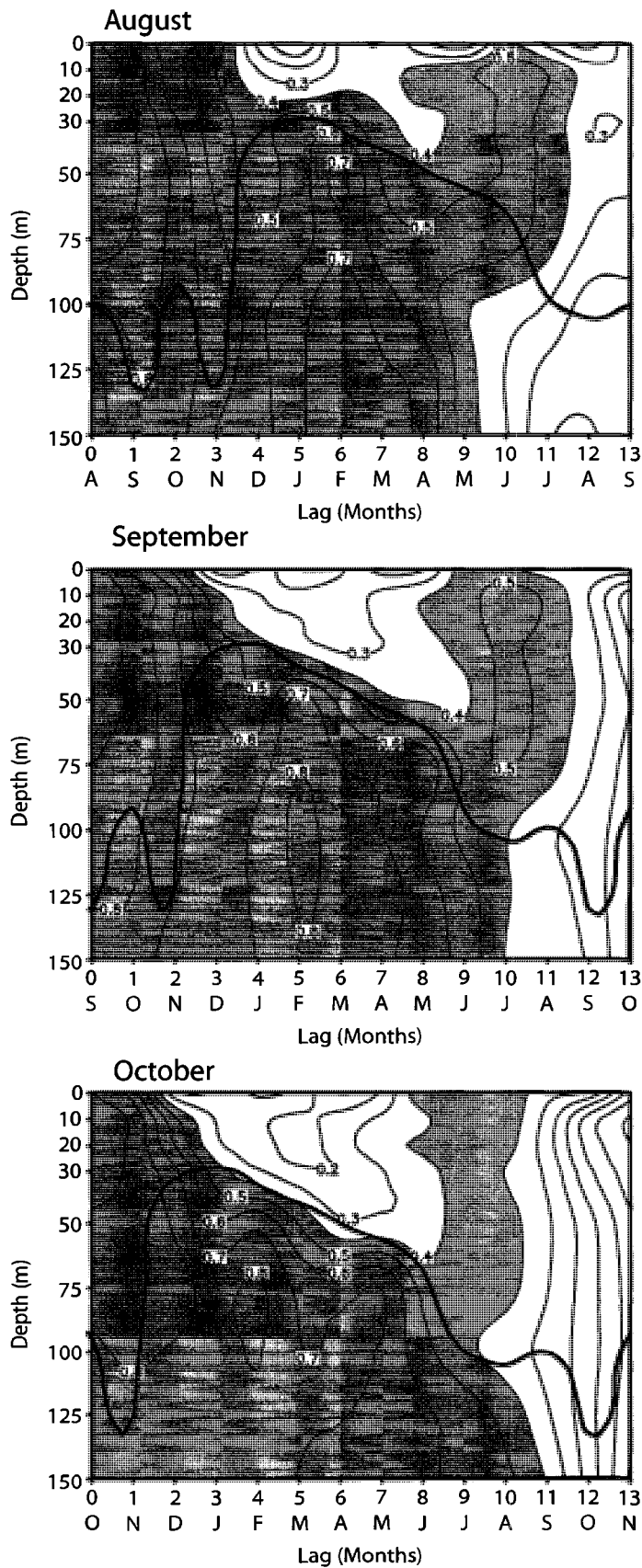


Figure 5.4. Lag correlations between monthly-mean surface temperature anomalies in (top) August, (middle) September, (bottom) October) and temperature anomalies at nine depths from 0 to 150 m for 0-13 month lags. For example, the correlation coefficient between September surface temperature anomalies and January temperature anomalies at 100 m is 0.7. Correlations that exceed 0.4 are shaded. The thick black line corresponds to the 0.8 contour from Figure 5.3.

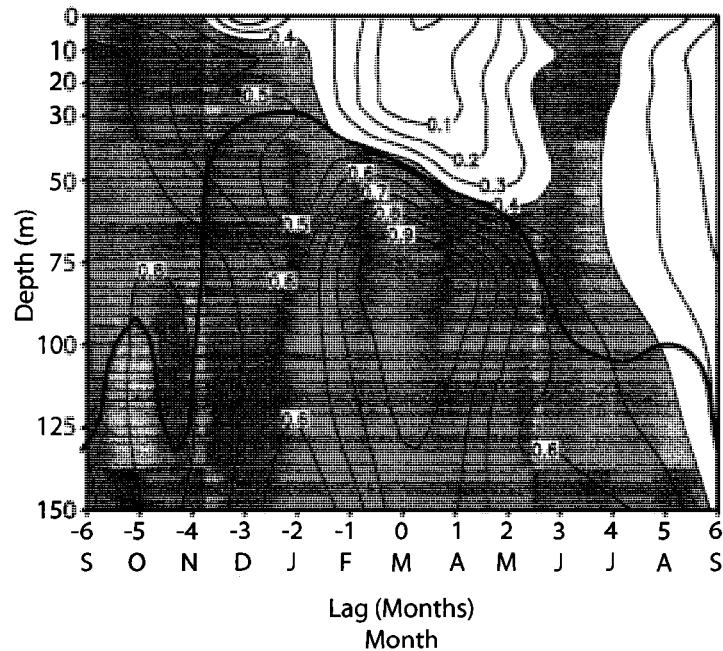


Figure 5.5. Lead-lag correlations between monthly-mean temperature anomalies in March at 75 m (i.e., beneath the base of the summer mixed layer; marked by an X) and temperature anomalies at nine depths from 0 to 150 m for the previous and following six months. For example, the correlation between March temperature anomalies at 75 m and temperature anomalies at 100 m in the previous October is 0.8. Correlations that exceed 0.4 are shaded. The thick black line corresponds to the 0.8 contour from Figure 5.3.

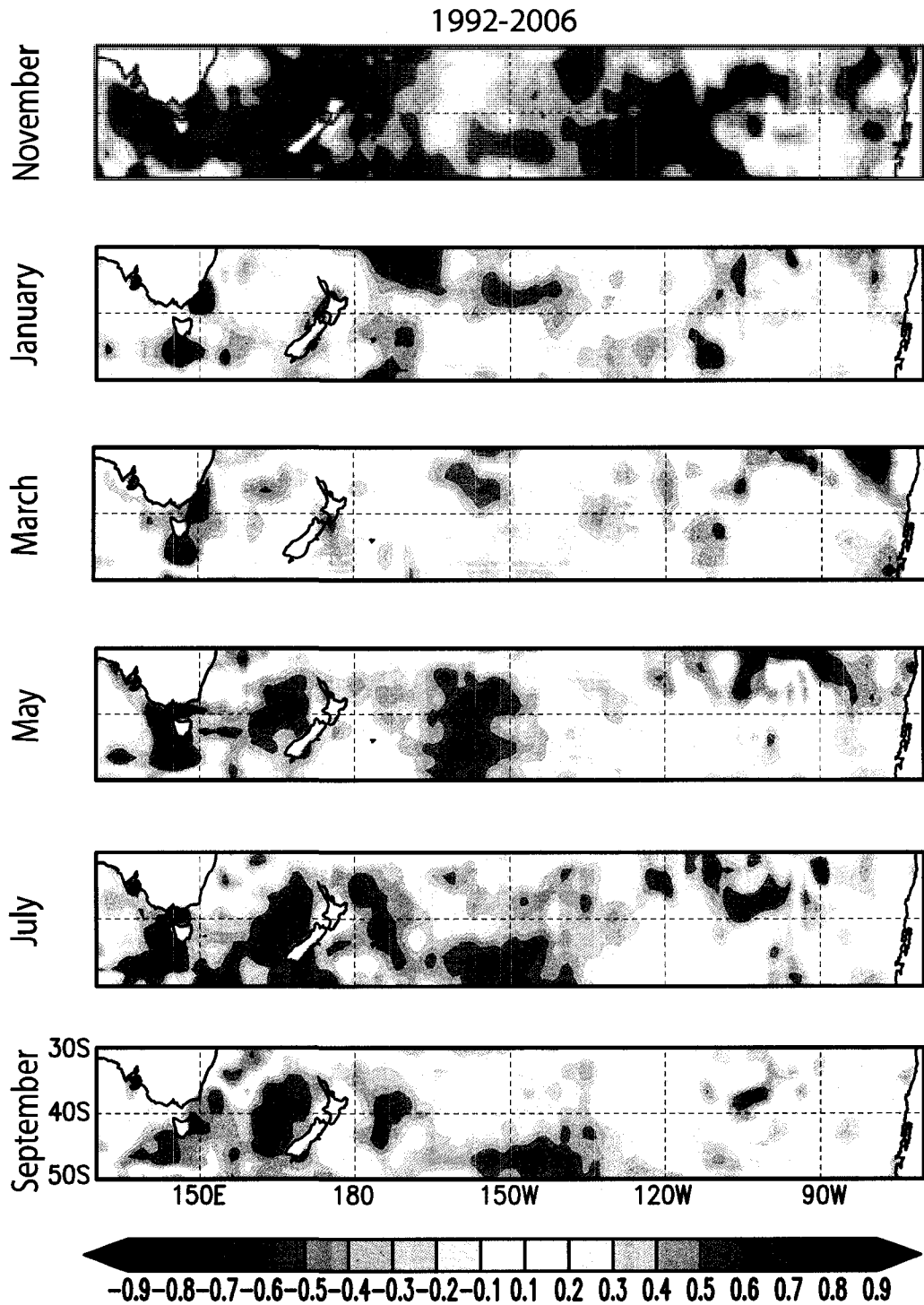


Figure 5.6. Correlations between September SST anomalies and (top) November SST anomalies (2nd from top) January SST anomalies, (3rd from top) March SST anomalies, (3rd from bottom) May SST anomalies, (2nd from bottom) July SST anomalies, and (bottom) September SST anomalies at all grid points for 1990-2006.

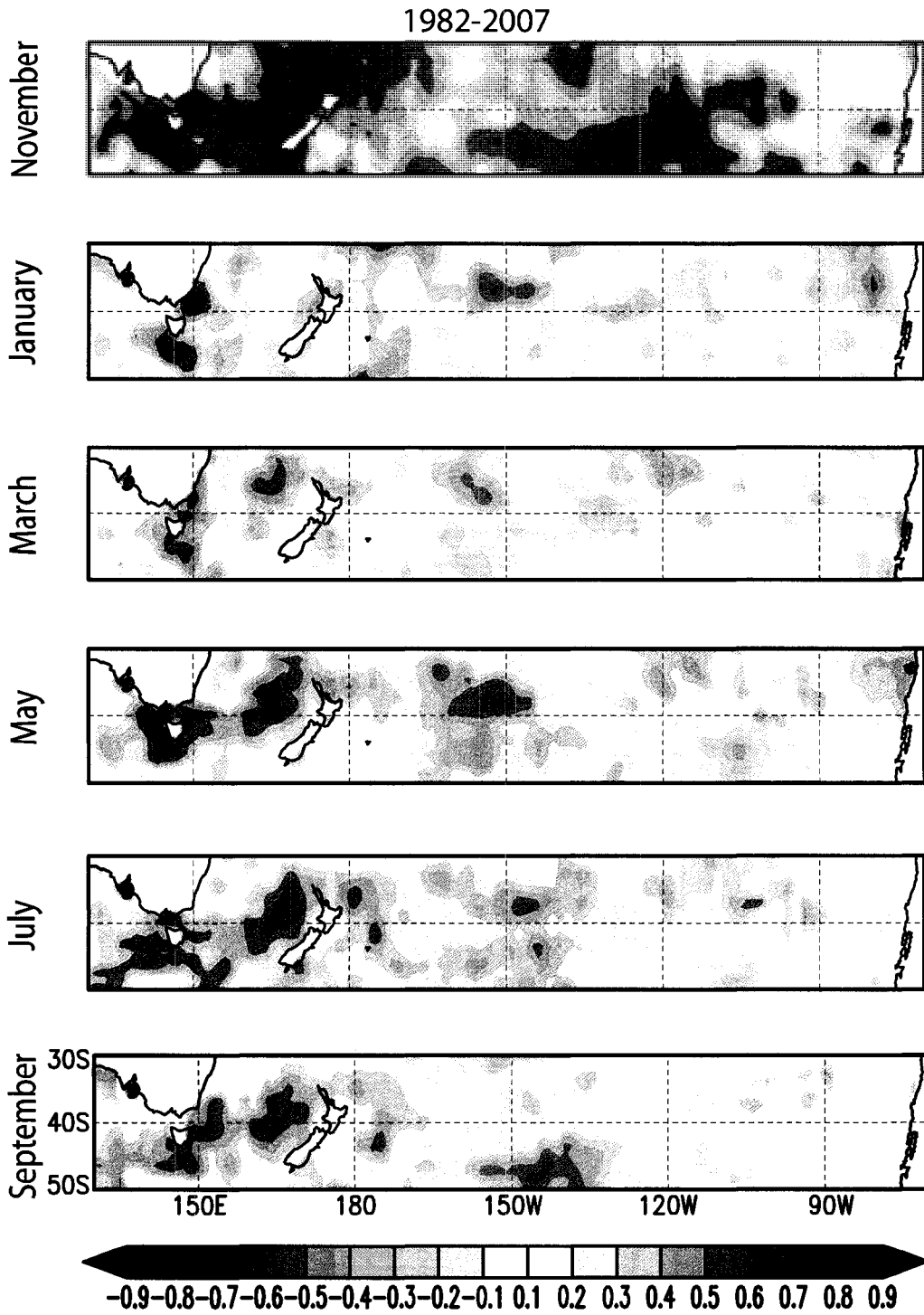


Figure 5.7. As in Figure 5.6 but for the period 1982-2006.

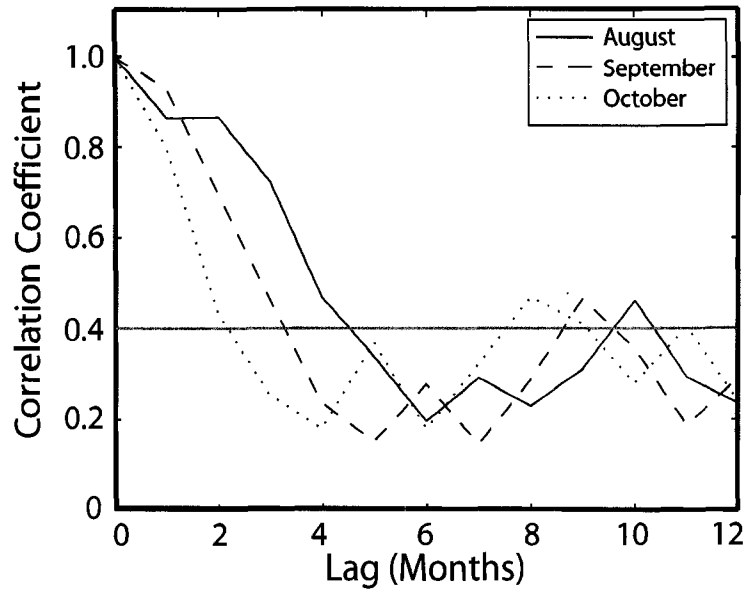


Figure 5.8. Lag correlations of monthly-mean OI SST anomalies averaged over the region 30°-34°S, 170°-180°E based on a starting month of August (solid line), September (dashed line), and October (dotted line). For example at lag 6, the solid line corresponds to a correlation between August and February SST anomalies of ~0.2. The gray line corresponds to the 95% confidence level ( $r \sim 0.4$ ).

## **CHAPTER SIX**

### **CONCLUSIONS**

This chapter provides a summary and discussion of the key results of the thesis and offers several avenues for future research.

#### **6.1 Summary and Discussion**

Until the late 1970s/ early 1980s, sea surface temperatures (SSTs) were primarily measured in situ onboard ships crossing between major population centers, which are largely concentrated in the Northern Hemisphere (NH). As a result, the North Atlantic and North Pacific basins were the only regions with sufficient SST data to examine extratropical SST variability on interannual timescales and longer. Many studies have shown that, consistent with the null hypothesis of extratropical SST variability (Frankignoul and Hasselman 1977), the primary mechanism that drives fluctuations in NH SSTs on intraseasonal and interannual time scales is variability in the surface turbulent heat fluxes associated with internal atmospheric forcing (e.g., Frankignoul and Reynolds 1983; Frankignoul 1985). Hence, the large-scale patterns of NH SST anomalies owe their existence to the dominant structures of atmospheric variability (Bjerknes 1964, Cayan 1992a,b, Visbeck et al. 2003).

Analyses of the NH ocean temperature field have also revealed the importance of the depth of the mixed layer on the persistence of extratropical SST anomalies. In particular, several studies have demonstrated that the subduction and re-entrainment of

SST anomalies associated with the seasonal cycle of the mixed layer depth, a process referred to as reemergence, gives rise to winter-to-winter persistence of SST anomalies in the NH ocean basins (Alexander and Deser 1995; Alexander et al. 1999; Timlin et al. 2002; Deser et al. 2003).

With the advent of satellite-derived surface temperature measurements in the late 1970s/ early 1980s, SST coverage around the globe has substantially improved. Hence, there are now several decades of SST measurements available in the Southern Hemisphere (SH), a period long enough to evaluate the importance of the mechanisms described above in the extratropical SH ocean basins. Thus, the goal of the current study is to provide the first comprehensive examination of the mechanisms that drive SST variability in the extratropical SH.

The first part of the study provides an extensive analysis of the relationships between variability in extratropical SH SST field and two important patterns of large-scale SH atmospheric variability: the Southern Annular Mode (SAM), and the El Niño Southern Oscillation (ENSO). These relationships were evaluated in both the warm (November-April) and cold (May-October) seasons. During the warm season, the SAM and ENSO are significantly correlated with each other, and therefore the SST patterns associated with both phenomena are similar: both are characterized by predominantly cold SST anomalies poleward of 50°S and warm SST anomalies equatorward of 50°S, but for a large region of cold anomalies that extends from the west of the Antarctic Peninsula to middle latitudes. A similar pattern of SST anomalies also emerges as the leading EOF of monthly (Chapter 3, this thesis) and annual-mean (Kidson and Renwick 2002) SST anomalies.

During the cold season, the SAM and ENSO are not significantly correlated with each other, and thus their associated SST patterns exhibit larger differences. The cold season expression of the SAM in the SST field resembles its warm season counterpart (Chapter 3), and also bears strong resemblance to the pattern of SST anomalies associated with the SAM in year-round data (Lovenduski and Gruber 2005; Sen Gupta and England 2006). In contrast, the cold season expression of ENSO in the SST field exhibits a more wave-like structure than its warm season counterpart, with largest amplitude in the Pacific sector. The leading EOF of monthly-mean cold season SST anomalies resembles the signature of ENSO in the SH SST field.

A comparison of the structures of the SST, surface turbulent and Ekman heat flux anomalies associated with the SAM reveals that the surface turbulent heat fluxes play an important role in driving the SAM-related SST anomalies throughout much of the SH, and that anomalous heat advection by Ekman currents also contributes at higher latitudes. That the large-scale patterns of SST anomalies associated with the SAM are primarily driven by surface turbulent heat fluxes is consistent with results found in previous studies for the Northern Annular Mode (NAM; e.g., Visbeck et al. 2003).

As is the case for the SAM, the ENSO-related SST anomalies project strongly onto the ENSO-related Ekman heat flux anomalies. But in contrast to the SAM, they do not project onto the ENSO-related turbulent heat fluxes. It is possible that the SH SST response to ENSO may be driven by processes such as ocean dynamics and radiative fluxes. However, numerous studies have demonstrated the consistency between ENSO-related surface turbulent heat fluxes and SST anomalies in the North Pacific (i.e., the atmospheric bridge; Alexander et al. 1990; 1992; 2002; Cayan 1992a; Lau and Nath

1996; 2001; Park et al. 2006). Shortwave radiation anomalies associated with ENSO explain some of the SST variability in the subtropical Pacific sector, but there are still many discrepancies between the pattern of combined (surface turbulent + Ekman + shortwave radiation) heat flux anomalies and the pattern of SST anomalies associated with ENSO. Hence it is equally plausible that the inconsistency between the ENSO-related SST and turbulent heat flux anomalies is due to the relatively short period of analysis used in this study and/or errors in the SH flux data.

In Chapter 4, weekly-mean data are used to examine the temporal evolution of the SAM-SST relationship. The results reveal that no unique pattern of extratropical SH SST anomalies leads variability in the SAM. Furthermore, correlations between the SAM and its associated SST anomalies are weak for periods when SSTs lead the SAM. The strongest and most statistically significant correlations are observed when the SST field lags the SAM by  $\sim 1$  week, and the correlations remain significant at least 8 weeks after peak amplitude in the SAM. The lead-lag relationships between the SAM and its expression in the SST field are consistent with the SH atmosphere forcing the SST field and not vice versa.

The SAM-related SST anomalies exhibit less persistence during the warm season than during the cold season. The different timescales are most evident when ENSO is linearly subtracted from the warm season data to account for the fact that ENSO and the SAM are significantly correlated during that season. The simple stochastic climate model constructed by Frankignoul and Hasselman (1977) reveals that the observed seasonal variations in the persistence of the SAM-related SST anomalies are consistent with seasonal variations in the depth of the mixed layer.

In Chapter 5, subsurface temperature observations are used to examine the winter-to-winter “reemergence” of SST anomalies in the extratropical South Pacific (30°-34°S, 170°-180°E). Reemergence is the mechanism through which SST anomalies formed in the late winter are stored beneath the relatively shallow summer mixed layer and then re-entrained into the deepening mixed layer during the following fall/winter. The results demonstrate that, consistent with reemergence, SST anomalies formed in the late winter/early spring are significantly correlated with SST anomalies during the following fall/winter but are only strongly correlated with temperature anomalies beneath the mixed layer during the intervening summer. The time-depth structure of the reemergence signal is robust to small changes in the month in which the SST anomalies are created, and reemergence explains ~20% of the year-to-year variance in the June SST field over the western extratropical South Pacific. The results based on the SH subsurface temperature data are broadly consistent with evidence of reemergence in the NH ocean basins (e.g., Alexander and Deser 1995; Alexander et al. 1999; Timlin et al. 2002).

The spatial scale of reemergence is independently evaluated across the extratropical South Pacific basin using sea surface temperature data. The results reveal the reemergence signal is statistically significant across the western South Pacific basin but is less apparent in the eastern part of the basin. It is unclear whether the absence of a reemergence signal in the eastern extratropical South Pacific is real or due to poor data sampling in that region. As more subsurface temperature data become available through programs like ARGO, we hope to continue examining reemergence in the SH oceans, particularly in the eastern South Pacific basin.

The results in Chapter 5 demonstrate that the reemergence of SST anomalies in the extratropical South Pacific yields predictability in anomalous SSTs out to ~8-10 months, which is longer than the known predictability associated with most other physical phenomena. If the reemerging SST anomalies impact the extratropical atmospheric circulation, then reemergence may prove to be important for seasonal forecasting. The atmospheric response to reemerging SST anomalies has not been examined in great detail as of yet but Cassou et al. (2007) have shown that reemerging SST anomalies in the North Atlantic tend to modestly enhance the winter-to-winter persistence of the atmospheric circulation pattern that created them (e.g., the North Atlantic Oscillation).

## **6.2 Future Research**

The results presented in Chapters 4 and 5 demonstrate that extratropical SH SST anomalies exhibit considerable persistence on timescales ranging from months to years. However, the extent to which these SH SSTs feedback onto the atmosphere is unclear. In the remainder of this section I will discuss my ideas for future research. The following ideas focus on the persistence of extratropical SSTs and the potential impact of the persisting SSTs on the atmospheric circulation.

### *6.2.1 Persistence of extratropical SST anomalies as a function of hemisphere*

In Chapter 4, lag autocorrelation analysis reveals that the cold season SAM-related SST anomalies tend to persist much longer than their warm season counterparts. Further lag autocorrelation analysis would be useful to determine whether the persistence

of North Atlantic SST anomalies associated with the NAM also exhibits similar seasonal variations. The lag autocorrelation analysis should also be applied to the full SH and NH SST fields (i.e., not just the anomalous SSTs related to the SAM and the NAM) to provide a more general understanding of the differences in the persistence of the extratropical SST anomalies between the NH and SH ocean basins.

### *6.2.2 Atmospheric response to persistent SH SST anomalies*

The results in Chapter 4 demonstrate that the cold season SH SST anomalies associated with the SAM exhibit considerable persistence from month-to-month, but do these SST anomalies feedback onto the atmospheric circulation? Many studies have documented an atmospheric response to anomalous SST forcing in the NH, but in most cases, the amplitude of the response is modest compared to that of internal atmospheric variability (see review by Kushnir et al. 2002). The atmospheric response to extratropical SSTs has received considerably less attention in the SH but previous results provide some evidence of a response of the SAM to changes in the SST field. For example, Sen Gupta and England (2007) note a coupling between the SAM-related SST anomalies and the atmospheric circulation that acts to increase the persistence of the SAM. Previous results also suggest that the relatively weak long-term warming of the Southern Ocean relative to middle and polar latitudes may potentially drive a positive trend in the SAM (Kushner et al. 2001).

A recent study by Marshall and Connolley (2006; hereafter MC06) demonstrates that changes in the meridional gradient in wintertime SSTs drive changes in the sign and the strength of the SAM. By forcing an atmospheric General Circulation Model (AGCM) with a zonally symmetric heat source located in the SH middle latitudes ( $\sim 60^{\circ}\text{S}$ ), they

showed that an increase in the meridional SST gradient enhances baroclinicity. The resulting anomalous eddy activity fluxes more momentum into the upper troposphere and increases the westerly winds, which projects onto the positive phase of the SAM. The opposite is true in the presence of a weakened meridional SST gradient. It has also been demonstrated that the eddy feedback mechanism described in MC06 is also important for driving an atmospheric response to anomalous extratropical SST forcing in the NH (e.g., Peng and Whittaker 1999; Peng and Robinson 2001; Peng et al. 2003; Magnusdottir et al. 2004; Deser et al. 2007).

Future work could expand upon the results of MC06 to examine the temporal evolution of the atmospheric response to meridional SST gradients induced by observed patterns of winter SST variability. Specifically, we want to ask the following questions: can the observed cold-season SST anomalies associated with the SAM (i.e., not the idealized zonally symmetric heat source used in MC06) induce a meridional SST gradient that impacts the SAM through the eddy feedback mechanism suggested in MC06? Furthermore, if the anomalous SSTs that induce the meridional SST gradient persist for several months, will the atmospheric response also persist for several months?

The ability of the atmospheric circulation to respond to variations in extratropical SSTs through the eddy feedback mechanism is dependent on several factors including the strength of the meridional SST gradient as well as the strength and position of the climatological storm track (e.g., Peng and Whitaker 1999; Hall et al. 2001). Thus changes in the strength or position of the SST anomalies that drive the meridional SST gradient or changes in the SH storm track can result in different atmospheric responses. The goal of this future research is to examine how the winter-to-summer evolution of the SAM-

related SST anomalies and the atmospheric circulation (e.g., the SH storm track) impact the atmospheric response to these SAM-related SSTs.

I propose to examine the SH atmospheric response to extratropical SST anomalies within the context of several AGCM experiments that are forced with time-varying patterns of SST anomalies. The experimental design proposed here is similar to the design presented in Cassou et al. (2004). The first experiment will consist of a multi-member ensemble integration, each 12 months long. The model would be forced with the observed pattern of SST anomalies associated with the SAM for the 6 winter months (May-October) and the other 6 months (November-April) will remain fixed to the climatology. The monthly SST anomalies would be derived from the regressions of SSTs onto the expansion coefficient time series of the winter SAM-related SST pattern (i.e., top right pattern in Fig. 3.3).

The temporal evolution of the horizontal and vertical structures of the atmospheric response will be examined from winter through summer. The atmospheric response will be decomposed into the component that projects onto the leading pattern of internal atmospheric variability (i.e., the SAM) and the residual component. This decomposition, as shown in Deser et al. (2004), is a useful method for distinguishing physically meaningful patterns that are associated with different underlying dynamical mechanisms.

I also propose to run at least two more AGCM experiments to evaluate the sensitivity of the extratropical SH atmospheric response to SSTs exhibiting various degrees of persistence. The second experiment would be designed similarly to the experiment described above. The only difference is that the anomalous SST forcings would exhibit larger persistence in the second experiment than in the first experiment

(i.e., the SST anomalies in the second experiment would decay more slowly than in the first experiment). In the third experiment, the prescribed SST anomalies would exhibit less persistence. The atmospheric response from the three experiments would be compared to determine whether increasing or decreasing the persistence in the SST field noticeably alters the structure and amplitude of the large-scale atmospheric circulation.

## REFERENCES

- Alexander, M. A., 1990: Simulation of the response of the North Pacific Ocean to the anomalous atmospheric circulation associated with El Niño. *Climate Dyn.*, **5**, 53-65.
- Alexander, M. A., 1992a: Midlatitude atmosphere-ocean interaction during El Niño. Part I: the North Pacific Ocean. *J. Climate*, **5**, 944-958.
- Alexander, M.A., and C. Deser, 1995: A mechanism for the recurrence of wintertime midlatitude SST anomalies. *J. Phys. Oceanog.*, **25**, 122-137.
- Alexander, M.A., C. Deser, and M.S. Timlin, 1999: The reemergence of SST anomalies in the North Pacific Ocean. *J. Climate*, **12**, 2419-2433.
- Alexander, M. A., M.S. Timlin, and J. D. Scott, 2001: Winter-to-winter recurrence of sea surface temperature, salinity and mixed layer depth anomalies. *Prog. Oceanogr.*, **49**, 41-61.
- Alexander, M.A., I. Bladé, M. Newman, J.R. Lanzante, N.C. Lau, and J.D. Scott, 2002: The Atmospheric Bridge: The influence of ENSO teleconnections on air-sea interaction over the global oceans. *J. Climate*, **15**, 2205-2231.
- Alexander, M. A., and J. D. Scott, 2008: The role of Ekman ocean transport in the Northern Hemisphere response to ENSO. *J. Climate*, in press.
- Battisti, D., U. Bhatt, and M. Alexander, 1995: A modeling study of the interannual variability in the wintertime North Atlantic Ocean. *J. Clim.*, **8**, 3067-3083.
- Bhatt, U.S., M.A. Alexander, D.S. Battisti, D.D. Houghton, and L.M. Keller, 1998: Atmosphere-ocean interaction in the North Atlantic: near-surface climate variability., *J. Climate*, **11**, 1615-1632.
- Boyer, T. P., J. I Antonov, H. E. Garcia, D. R. Johnson, R. A. Locarnini, A. V. Mishonov, M. T. Pitcher, O. K. Baranova, and I. V. Smolyar, 2006: *World Ocean Database 2005*. S. Levitus, Ed., NOAA Atlas NESDIS 60, U.S. Government Printing Office, Wash., D. C., 190 pp., DVDs.
- Barsguli, J. J., and D. S. Battisti, 1998: The basic effects of atmosphere-ocean thermal coupling on midlatitude variability. *J. Atmos. Sci.*, **55**, 477-493.

- Bretherton, C. S., M. Widmann, V. P. Dymnikov, J. M. Wallace, and I. Blade, 1999: The effective number of spatial degrees of freedom of a time-varying field. *J. Clim.*, **12**, 1990-2009.
- de Boyer Montégut, C., G. Madec, A. S. Fischer, A. Lazar, and D. Idicone, 2004: Mixed layer depth over the global ocean: An examination of profile data and a profile-based climatology. *J. Geophys. Res.*, **109**, C12003, doi:10.1029/2004JC002378.
- Bjerknes, J., 1964: Atlantic air-sea interaction, *Adv. Geophys.*, **10**, 1-82.
- Cassou, C., et al., 2004: Summer sea surface temperature conditions in the North Atlantic and their impact upon the atmospheric circulation in early winter. *J. Climate*, **17**, 3349–3363.
- Cassou C., C. Deser, and M. A. Alexander, 2007: Investigating the impact of reemerging sea surface temperature anomalies on the winter atmospheric circulation over the North Atlantic. *J. Climate*, **20**, 3510–3526.
- Cayan, D. R., 1992a: Latent and sensible heat-flux anomalies over the northern oceans: the connection to monthly atmospheric circulation. *J. Climate*, **5**, 354-369.
- Cayan, D. R., 1992b: Latent and sensible heat-flux anomalies over the northern oceans: driving the sea surface temperature. *J. Phys. Oceanogr.*, **22**, 859-881.
- Czaja, A. and C. Frankignoul, 1999: Influence of the North Atlantic SST on atmospheric circulation. *Geophys. Res. Lett.*, **26**, 2969-1972.
- Deser, C., M. A. Alexander, and M. S. Timlin, 2003: Understanding the persistence of sea surface temperature anomalies in midlatitudes. *J. Climate*, **16**, 57-72.
- Deser C., G. Magnusdottir, R. Saravanan, and A. S. Phillips, 2004: The effects of North Atlantic SST and sea-ice anomalies on the winter circulation in CCM3. Part II: Direct and indirect components of the response. *J. Climate*, **17**, 877–889.
- Deser, C., R.A. Tomas, and S. Peng, 2007: The Transient Atmospheric Circulation Response to North Atlantic SST and Sea Ice Anomalies. *J. Climate*, **20**, 4751–4767.
- Frankignoul, C., 1985: Sea surface temperature anomalies, planetary waves, and air-sea feedback in the middle latitudes. *Rev. Geophys.*, **23**, 357-390.
- Frankignoul, C., and K. Hasselman, 1977: Stochastic climate models. Part II: Application to sea-surface temperature variability and thermocline variability. *Tellus*, **29**, 289-305.

- Frankignoul, C., and R.W. Reynolds, 1983: Testing a Dynamical Model for Mid-Latitude Sea Surface Temperature Anomalies., *J. Climate*, **13**, 1131–1145.
- Fyfe, J. C., and O. A. Saenko, 2006: Simulated changes in the extratropical Southern Hemisphere winds and currents. *Geophys. Res. Lett.*, **33**, L06701.
- Gandin, L. S., 1963: *Objective Analysis of Meteorological Fields*. Gidrometeorizdat, 238 pp. (Translated from Russian by Israeli Program for Scientific Translations in 1965.)
- Gille, S. T., 2002. Warming of the Southern Ocean since the 1950s, *Science*, **295**, 1275-1277.
- Gupta, A. S. and M. H. England, 2006: Coupled ocean-atmosphere-ice response to variations in the Southern Annular Mode. *J. Climate*, **19**, 4457-4486.
- Gupta, A.S., and M.H. England, 2007: Coupled ocean–atmosphere feedback in the Southern Annular Mode. *J. Climate*, **20**, 3677–3692.
- Haarsma, R. J., E. J. D. Campos, W. Hazeleger, C. Severijns, A. R. Piola, and F. Molteni, 2005: Dominant modes of variability in the South Atlantic: study with a hierarchy of ocean–atmosphere models. *J. Climate*, **18**, 1719–1735.
- Hadfield, M. G., 2000: Atmospheric effects on upper-ocean temperature in the southeast Tasman Sea. *J. Climate*, **30**, 3239-3248.
- Hall, A., and M. Visbeck, 2002: Synchronous variability in the Southern Hemisphere atmosphere, sea ice, and ocean resulting from the annular mode. *J. Climate*, **15**, 3043-3057.
- Hall N. M. J., J. Derome, and H. Lin, 2001: The extratropical signal generated by a midlatitude SST anomaly. Part I: Sensitivity at equilibrium. *J. Climate*, **14**, 2035–2053.
- Hanawa, K. and S. Sugimoto, 2004: ‘Reemergence’ of winter sea surface temperature anomalies in the world’s oceans. *Geophys. Res. Lett.*, **31**, L10303.
- Haney, R.L., 1985: Midlatitude sea surface temperature anomalies: A numerical hindcast. *J. Phys. Oceanogr.*, **15**, 787–799.
- Hartmann, D. L., 1994: *Global Physical Climatology*. Academic Press, 411 pp.
- Hogg, A. M., and J.R. Blundell, 2006: Interdecadal variability of the Southern Ocean. *J. Phys. Oceanogr.*, **36**, 1626–1645.
- Hogg, N. G., 1992: On the transport of the Gulf Stream between Cape Hatteras and the Grand Banks. *Deep-Sea Res.*, **39**, 1231-1246.

- Hogg, N. G., and W. E. Johns, 1995: Western boundary currents. *U.S. National Report to International Union of Geodesy and Geophysics 1991-1994*, Supplement to *Rev. of Geophys.*, **33**, 1311-1334.
- Holland, M. M., C. M. Blitz, E. C. Hunke, 2005: Mechanisms forcing an Antarctic Dipole in simulated sea ice and surface ocean conditions. *J. Climate.*, **18**, 2052-2066.
- Hoskins, B. J., and D. J. Karoly, 1981: The steady linear response of a spherical atmosphere to thermal and orographic forcing. *J. Atmos. Sci.*, **38**, 1179-1197.
- Ingleby, B., and M. Huddleston, 2007: Quality control of ocean temperature and salinity profiles - historical and real-time data. *Journal of Marine Systems*, **65**, 158-175  
10.1016/j.jmarsys.2005.11.019.
- Johns, W.E., T.J. Shay, J.M. Bane, D.R. Watts, 1995: Gulf Stream structure, transport, and recirculation near 68° W. *J. Geophys. Res.*, **100**, 817-838.
- Kalnay, E., M. Kanamitsu, R. Kistler, W. Collins, D. Deaven, L. Gandin, M. Iredell, S. Saha, G. White, J. Woollen, Y. Zhu, A. Leetmaa, B. Reynolds, M. Chelliah, W. Ebisuzaki, W. Higgins, J. Janowiak, K. Mo, C. Ropelewski, J. Wang, R. Jenne, and D. Joseph, 1996: The NCEP/NCAR 40-Year Reanalysis Project. *Bull. Amer. Soc.*, **77**, 437-471.
- Karoly, D. J., 1989: Southern Hemisphere circulation features associated with El Niño-Southern Oscillation Events. *J. Climate*, **2**, 1239-1251.
- Karoly, D. J., 1990: The role of transient eddies in low-frequency zonal variations of the Southern Hemisphere circulation. *Tellus*, **42A**, 41-50.
- Karsten, R. H., and J. Marshall, 2002: Constructing the residual circulation of the ACC from observations. *J. Phys. Oceanogr.*, **32**, 3315-3327.
- Kidson, J. W., 1988: Interannual variations in the Southern Hemisphere circulation. *J. Climate*, **1**, 1177-1198.
- Kidson, J. W., and J. A. Renwick, 2002: The Southern Hemisphere evolution of ENSO during 1981-1999. *J. Climate*, **15**, 847-863.
- Kidwell, K. B., 1991: NOAA polar orbiter data users guide. National Oceanic and Atmospheric Administration, 280 pp. [Available from NOAA, Washington, DC 20233.].

- Kidwell, K. B., 1995: NOAA polar orbiter data users guide (NOAA TIROS 6-14). NOAA NESDIS Rep., 386 pp. [Available from NESDIS, Federal Office Building 3, Washington DC 20233.].
- Kiladis, G. N., and K. C. Mo, 1998: Interannual and intraseasonal variability in the Southern Hemisphere. *Meteorology of the Southern Hemisphere*. D. J. Karoly and D. G. Vincent. Eds., Amer. Met. Soc., 307-336.
- Kistler, R., E. Kalnay, W. Collins, S. Saha, G. White, J. Woollen, M. Chelliah, W. Ebisuzaki, M. Kanamitsu, V. Kousky, J. van den Doo, R. Jenne, and M. Fiorino, 2001: The NCEP-NCAR 50-year reanalysis: Monthly means CD-ROM and documentation. *Bull. Amer. Meteor. Soc.*, **82**, 247-268.
- Klein, S.A., B.J. Soden, and N.C. Lau, 1999: Remote Sea Surface Temperature Variations during ENSO: Evidence for a Tropical Atmospheric Bridge. *J. Climate*, **12**, 917-932.
- Kushnir, Y., W.A. Robinson, I. Bladé, N.M.J. Hall, S. Peng, and R. Sutton, 2002: Atmospheric GCM response to extratropical SST anomalies: synthesis and evaluation., *J. Climate*, **15**, 2233-2256.
- Kushner, P.J., I.M. Held, and T.L. Delworth, 2001: Southern Hemisphere atmospheric circulation response to global warming., *J. Climate*, **14**, 2238-2249.
- Lau, N.-C. and M. J. Nath, 1996: The role of the 'atmospheric bridge' in linking tropical Pacific ENSO events to extratropical SST anomalies. *J. Climate*, **9**, 2036-2057.
- Lau, N. C., and M. J. Nath, 2001: Impact of ENSO on SST variability in the North Pacific and North Atlantic: seasonal dependence and role of extratropical air-sea coupling. *J. Climate*, **14**, 2846-2866.
- Lefebvre, W., H. Goosse, R. Timmermann, and T. Fichefet, 2004: Influence of the Southern Annular Mode on the sea ice-ocean system. *J. Geophys. Res.*, **109**(C09006), doi:10.1029/2004JC002403.
- Li, Z. X., 2000: Influence of tropical Pacific El Niño on the SST of the Southern Ocean through atmospheric bridge. *Geophys. Res. Lett.*, **27**, 3505-3508.
- L'Heureux, M. L., and D. W. J. Thompson, 2006: Observed relationships between El Niño Southern Oscillation and the extratropical zonal-mean circulation. *J. Climate*, **19**, 276-287.
- Lorenz, D. J., and D. L. Hartmann, 2001: Eddy-zonal feedback in the Southern Hemisphere. *J. Atmos. Sci.*, **58**, 3312-3327.

- Lovenduski, N. S., and N. Gruber, 2005: Impact of the Southern Annular Mode on Southern Ocean circulation and biology. *Geophys. Res. Lett.*, **32**, doi:10.1029/2005GL022727.
- Lovenduski, N.S., N. Gruber, S.C. Doney and I.D. Lima, 2007: Enhanced CO<sub>2</sub> outgassing in the Southern Ocean from a positive phase of the Southern Annular Mode. *Global Biogeochem. Cycles*, **21**, GB2026, doi:10.1029/2006GB002900.
- Luksch, U. and H. v. Storch, 1992: Modeling the low-frequency sea surface temperature variability in the North Pacific. *J. Climate*, **5**, 893-906.
- Magnusdottir G., C. Deser, and R. Saravanan, 2004: The effects of North Atlantic SST and sea-ice anomalies on the winter circulation in CCM3. Part I: Main features and storm-track characteristics of the response. *J. Climate*, **17**, 857–876.
- Marshall G. J., and W. M. Connolley, 2006: Effect of changing Southern Hemisphere winter sea surface temperatures on Southern Annular Mode strength. *Geophys. Res. Lett.*, **33**, L17717, doi:10.1029/2006GL026627.
- Marshall, J., H. Johnson, and J. Goodman, 2001: A study of the interaction of the North Atlantic Oscillation with ocean circulation. *J. Climate*, **14**, 1399-1421.
- Meredith, M. P., L. Woodworth, C. W. Hughes, and V. Stepanov, 2004: Changes in the ocean transport through Drake Passage during the 1980s and 1990s, forced by changes in the Southern Annular Mode. *Geophys. Res. Lett.*, **31**, L21305, doi:10.1029/2004GL021169.
- Meredith, M. P., and A. M. Hogg, 2006: Circumpolar response of Southern Ocean eddy activity to a change in the Southern Annular Mode. *Geophys. Res. Lett.*, **33**, doi:10.1029/2006GL026499.
- Monterey, G. I., and S. Levitus, 1997: *Climatological cycle of mixed layer depth in the world ocean*. U.S. Gov. Printing Office, NOAA NESDIS, 5pp.
- Namias, J., and R. M. Born, 1970: Temporal coherence in North Pacific sea-surface temperature patterns. *J. Geophys. Res.*, **75**, 5952-5955.
- Namias, J., and R. M. Born, 1974: Further studies of temporal coherence in North Pacific sea surface temperatures. *J. Geophys. Res.*, **79**, 797-798.
- Newman, M., 2007: Interannual to decadal predictability of tropical and North Pacific sea surface temperatures. *J. Climate*, **20**, 2333-2356.
- Nilsson, C. S., and G. R. Cresswell, 1981: The formation and evolution of East Australian Current warm-core eddies. *Progress in Oceanography*, **9**, 133–183.

- North, G. R., R. L. Bell, R. F. Cahalan, and F. J. Moeng, 1982: Sampling errors in the estimation of empirical orthogonal functions. *Mon. Wea. Rev.*, **110**, 699-706.
- O'Neill, L. W., D. B. Chelton, and S. K. Esbensen, 2003: Observations of SST-induced perturbations of the wind stress field over the Southern Ocean on seasonal timescales. *J. Climate*, **16**, 2340-2354.
- Orsi, A. J., T. W. Whitworth III, and W. D. Nowlin Jr., 1995: On the meridional extent and fronts of the Antarctic Circumpolar Current. *Deep-Sea Research.*, **42**, 641-673.
- Park, S., C. Deser, and M.A. Alexander, 2005: Estimation of the Surface Heat Flux Response to Sea Surface Temperature Anomalies over the Global Oceans. *J. Climate*, **18**, 4582-4599.
- Park, S., M. A. Alexander, and C. Deser, 2006: The impact of cloud radiative feedback, remote ENSO forcing, and entrainment on the persistence of North Pacific sea surface temperature anomalies. *J. Climate*, **19**, 6243-6261.
- Peng S., and J. S. Whitaker, 1999: Mechanisms determining the atmospheric response to midlatitude SST anomalies. *J. Climate*, **12**, 1393-1408.
- Peng S., and W. A. Robinson, 2001: Relationships between atmospheric internal variability and the responses to an extratropical SST anomaly. *J. Climate*, **14**, 2943-2959.
- Peng S., W. A. Robinson, and S. Li, 2003: Mechanisms for the NAO responses to the North Atlantic SST tripole. *J. Climate*, **16**, 1987-2004.
- Peterson, R.G., 1988. On the transport of the Antarctic Circumpolar Current through Drake Passage and its relation to the wind, *J. Geophys. Res.*, **93**, 13,993-14,004.
- Pond, S., and G. L. Pickard, 1983: *Introductory Dynamical Oceanography*. 3<sup>rd</sup> ed. Butterworth-Heinemann, 329pp.
- Renwick, J. A., 2002: Southern Hemisphere circulation and relations with sea ice and sea surface temperature. *J. Climate*, **15**, 3058-3068.
- Reynolds, R.W., 1988: A real-time global sea surface temperature analysis. *J. Climate*, **1**, 75-87.
- Reynolds, R.W., and D.C. Marsico, 1993: An improved real-time global sea surface temperature analysis. *J. Climate*, **6**, 114-119.

- Reynolds, R. W., and T. M. Smith, 1994: Improved global sea surface temperature analysis using optimum interpolation. *J. Climate.*, **7**, 929-948.
- Reynolds, R. W., N. Rayner, T. M. Smith, D. C. Stokes, and W. Wang, 2002: An improved in situ and satellite SST analysis for climate. *J. Climate.*, **15**, 1609-1625.
- Rintoul, S. R., et al. 2001: The Antarctic Circumpolar Current System. In G. Siedler, J. Church, and J. Gould, editors, *Ocean Circulation and Climate*, pp. 271-302. Academic Press, San Diego, CA, USA.
- Sabine, C. L., 2004: The Oceanic Sink for Anthropogenic CO<sub>2</sub>. *Science*, **305** (5682), 367-371.
- Saravanan, R., and J.C. McWilliams, 1998: Advective ocean-atmosphere interaction: An analytical stochastic model with implications for decadal variability. *J. Clim.*, **11**, 165-188.
- Sardesmukh, P. D., and B. J. Hoskins, 1988: The generation of global rotational flow by steady idealized tropical divergence. *J. Atmos. Sci.*, **45**, 1228-1521.
- Seager, R., Y. Kushnir, M. Visbeck, N. Naik, J. Miller, G. Krahnmann, and H. Cullen, 2000: Causes of Atlantic Ocean climate variability between 1958 and 1998. *J. Climate*, **13**, 2845-2862.
- de Soezke, R. A., and M. D., Levine, 1981: The advective flux of heat by mean geostrophic motions in the Southern Ocean. *Deep-Sea Res.*, **28**, 1057-1085.
- Sterl, A. and W. Hazeleger, 2003: Coupled variability and air-sea interaction in the South Atlantic Ocean. *Climate Dyn.*, **21**, 559-571.
- Thompson, D. W. J., and J. M. Wallace, 2000: Annular modes in the extratropical circulation: Part I: month-to-month variability. *J. Climate*, **13**, 1000-1015.
- Thompson, D. W. J., and S. Solomon, 2002: Interpretation of recent Southern Hemisphere climate change. *Science*, **296**, 895-899.
- Timlin, M.S., M.A. Alexander, and C. Deser, 2002: On the reemergence of North Atlantic SST anomalies., *J. Climate*, **15**, 2707-2712.
- Verdy, A., J. Marshall, and A. Czaja, 2006: Sea surface temperature variability along the path of the Antarctic Circumpolar Current. *J. Phys. Oceanography*, **36**, 1317-1331.
- Visbeck, M., E. P. Chassignet, R. G. Curry, T. L. Delworth, R. R. Dickson, and G. Krahnmann, 2003: The Ocean's Response to North Atlantic Oscillation Variability. The North Atlantic Oscillation: Climatic Significance and Environmental Impact, J. W. Hurrell, Y. Kushnir, G. Ottersen, M. Visbeck, American Geophysical Union, 113-

- Watanabe, M. and M. Kimoto, 2000: On the persistence of decadal SST anomalies in the North Atlantic. *J. Climate*, **13**, 3017-3028.
- Watterson, I. G, 2000: Southern midlatitude zonal wind vacillation and its interaction with the ocean in GCM simulations. *J. Climate*, **13**, 562-578.
- Whitworth, T., 1983: Monitoring the transport of the Antarctic Circumpolar Current at Drake Passage. *J. Phys. Oceanogr.*, **13**, 2045-2057.
- Whitworth, T., and R. Peterson, 1985: Volume transport of the Antarctic Circumpolar Current from bottom pressure measurements. *J. Phys. Oceanography*, **15**, 810-816.
- Woodruff, S. D., R. J. Slutz, R. L. Jenne, and P. M. Steurer, 1987: A comprehensive ocean-atmosphere data set. *Bull. Amer. Meteor. Soc.*, **68**, 521-527.